CONF-880363--3

"The submitted manuscript has been authored by a contractor of the U.S. Government under contract DE-AC05-84OR21400. Accordingly, the U.S. Government retains a nonexclusive, royalty-free license to publish or reproduce the published form of this contribution, or allow others to do so, for U.S. Government purposes."

LINEAR IDEAL MHD STABILITY CALCULATIONS FOR ITER

John Hogan

CONF-880363--3

DE88 011012

1. INTRODUCTION

A survey of MHD stability limits has been made to address issues arising from the MHD - poloidal field design task of the US ITER project. This is a summary report on the results obtained to date.

As described at the November. 1987 ITER meeting, the objective of the ITER study is to 'develop and maintain baseline design(s) at a system codes level'. It is not intended to produce a 'new, fully engineered U.S. machine'. Thus, a primary goal of the work is to provide scaling information for the systems codes regarding the possible MHD constraints on the ITER operating space.

The study described here evaluates the dependence of ballooning, Mercier and low-n ideal linear MHD stability on key system parameters to estimate overall MHD constraints for ITER.

The calculations have been carried out with a version of the PEST 2.4 stability code [1] and the PEST ballooning package, supplied to ORNL by Dr. J. Manickam of PPPL.

The ITER operating space limitations must be expressed as functions of the available geometric parameters free to be chosen by the designer : aspect ratio. elongation, triangularity, and indentation. In addition, the plasma parameters related to the rotational transform (central and edge q, local shear) and pressure profiles (peak and average values) must be varied. Given values for these variables, the instability mode number and effective external wall position must be specified as well. Adopting, for simplicity, zero indentation, there are 10 significant parameters. A relatively coarse survey, with 3 values for each, would require ~ 60,000 cases, and a more refined study, with 5 points per variable would need ~ 10^7. Even these figures refer to an overly simplified representation of the MHD stability problem since, for example, we use 5 parameters to represent the q profile in the present study.

* Research sponsored by the Office of Fusion Energy, U.S. Department of Energy, under contract DE-AC05-84OR21400 with Martin Marietta Energy Systems, Inc.

DISTRIBUTION OF THIS DOCUMENT IS UNLIMITED

These considerations suggest very strongly that data acquisition be well organised, and that a sharply restricted number of issues be examined.

The equilibrium and stability results have been collated in a database system, in order to examine the systematics of scaling. The database combines the commercial 1032 system [2] for data archiving and manipulation with the PPPL LOCUS software [3] for plotting and fitting. Equilibrium and stability calculations are performed on the US NMFECC Cray machines, while database storage and activity is restricted at present to the ORNL Fusion Energy Division VAX cluster. Use of this ORNL stability database by the ITER study group at Garching has been proposed.

The ITER issues addressed in this report are :

1. Is there an optimum elongation for fixed triangularity at the present US ITER engineering limit ($\delta = 0.4$)?
2. Is there an optimum triangularity for nominal fixed elongation $\kappa \sim 2$ - 2.5?
3. How severe are restrictions on the operating space arising from non-optimal q values ('ravines' [4,5])?
4. What is the magnitude of the effect of the external wall on the accessible operating space ?
5. What is the effect of larger aspect ratio on beta limits?
6. Are there restrictions on the operating space due to use of typical current drive profiles?
7. What modifications arise from the use of self-consistent transport profiles?
8. What is the nature of the modes which define the limiting boundaries of the operating space.
9. What is the functional dependence of the Troyon parameter $C_T(\kappa, \delta, A, q, p)$, and is there an optimal choice of variables for systems code analysis ?

The report is arranged as follows: section 2 elaborates on the specific questions covered in the report, section 3 describes the equilibrium data used for the stability study, section 4 gives more detail on the parameters used in the stability calulation. Section 5 presents

the stability results and section 6 is devoted to discussion of the results and of directions for further study.

DISCLAIMER

This report was prepared as an account of work sponsored by an agency of the United States Government. Neither the United States Government nor any agency thereof, nor any of their employees, makes any warranty, express or implied, or assumes any legal liability or responsibility for the accuracy, completeness, or usefulness of any information, apparatus, product, or process disclosed, or represents that its use would not infringe privately owned rights. Reference herein to any specific commercial product, process, or service by trade name, trademark, manufacturer, or otherwise does not necessarily constitute or imply its endorsement, recommendation, or favoring by the United States Government or any agency thereof. The views and opinions of authors expressed herein do not necessarily state or reflect those of the United States Government or any agency thereof.

2. ISSUES

The MHD stability issues posed for study by the MHD- Poloidal field design task force are elaborated in this section.

2.1 Optimum elongation

The strong dependence of ITER cost on elongation has been stressed by Perkins [6]. From the overall economics aspect, (Figure in [6]), there appears to be a window for elongation , $2.0 \leq \kappa \leq 2.4$, within which κ should lie. (The assumptions used to obtain this result were that the triangularity was increased along with the elongation. As κ varied from $1 \rightarrow 3$, δ rose from $0 \rightarrow 1$.)

Thus, given triangularity constrained for ITER-3 to a putative engineering limit ($\delta = 0.4$), is there an optimum elongation for stability, or does β_{crit} increase without limit? Systems code analyses tend to seek the maximum possible κ if not so constrained.

2.2 Optimum triangularity

ITER work at the ORNL Fusion Energy Design Center motivated study of the question whether, given a nominal value for κ, there is an optimal triangularity. This could cause a revision of the engineering limit imposed in the first study. The systems code impact here is similar to that motivating the first issue.

2.3 Structure of the operating space

MHD stability studies are complicated by the fact that the stable operating space has a complex structure. Unstable operating points in the midst of an otherwise stable zone ('Ravines') have been observed by several groups [4,5] as q_ψ is varied. In addition, there is sensitivity to details of the profiles: intermediate-n 'infernal' modes can be expected with low shear profiles, and disappear with the addition of moderate shear. Hence, a detailed study varying the q profiles is required to assess the robustness of the dependences $\beta_{crit}(\kappa)$ and $\beta_{crit}(\delta)$.

2.4 External wall effects

For the studies described above, it is assumed that the wall is at ∞, both to be conservative and because the 'effective wall' location cannot be specified until a detailed poloidal coil design is chosen. However, stability of the external kink mode is very sensitive to the existence and presumed location of an external wall, so some estimate of the wall effect must be made.

2.5 Aspect ratio scaling

The ITER preliminary design evolved from the original TIBER-II design [7], and a more ambitious radial build was proposed, resulting in a lower aspect ratio for the device. As MHD stability generally improves at lower aspect ratio [8], a study similar to that described in section 2.1 has been carried out at the TIBER-II aspect ratio, A=3.6, with the same constraints on the shape, in order to document aspect ratio effects for possible future evolution of the design.

2.6 Current drive effects on stability

The important role of driven currents in ITER implies that we study the sensitivity of MHD stability to the current profile shape. Some flexibility is afforded by the freedom to use any of a number of current drive schemes (lower hybrid and neutral beams, for example) in producing optimal profiles. However, some schemes are more effective in producing edge localised profiles (with smaller ℓ_i values), and the effect of varying current density profiles on the operating space has been addressed.

2.7 Transport profiles

Optimal profiles for stability have been used in the preceding studies, to estimate the operating space constraints. These profiles are not necessarily similar to those which are optimal for neutron production, or those which are extrapolated from exisitng high-β experiments. Peaking the pressure profile will enhance the fusion output, and so an assessement of the impact of this peaking on the stability characteristics has been performed.

2.8 Mode analysis

While calculation of fitting formulae from the broadest possible database is the primary goal of the study, it is important to have as detailed as possible an understanding of the physical modes which actually limit performance. This level of analysis is more difficult to provide on a bulk basis, since it requires, e.g., the grid convergence studies concomitant with use of Pest 1. A sub-set of the database has been examined to establish the nature of the modes which determine the operating boundary.

2.9 Systems code interface

The major purpose of this MHD study is to provide a detailed description of the structured operating space in a form useful for systems code analysis. This application requires the extraction of limiting curves from the database, and the formulation of fits to these curves to describe the dependence $C_T(\kappa, \delta, A, q, p)$.

In translating the results of the MHD survey into a form useful for systems code analysis, appropriate variables must be chosen. In particular, Peng and Strickler [9] have proposed the use of $\bar{q}$ as a reliable indicator of the rotational transform for highly elongated and/or diverted configurations.

$$\bar{q} \equiv \oint \frac{dl}{R^2 B_{pol}}$$

An assessment has been made of the relative properties of $\bar{q}$ and q^* as indicators of ideal stability, where

$$q^* \equiv \frac{5a^2}{2R^2 I}\left(1 + \kappa^2(1 + 2\delta^2)\right)$$

The systems code requires a scaling description of the dependence of the stability boundary on the important parameters. we have this found least-squares fits to the β^{max} values obtained by the survey for systems code use.

3. EQUILIBRIUM PARAMETERS

The equilibrium is computed with the DeLucia, Jardin, Todd [10] flux-coordinates equilibrium code. The PEST mapper codes are used to produce input files for the stability codes and the EQDSK and mapper files are stored at the US NMFECC for later use. (Appendix 1 describes details of the database system.)

3.1 Equilibrium parameter ranges

For all the results presented the system parameters lie in the following ranges:

- Aspect ratio, A = 2.9 or 3.6
- Elongation, κ , varies between 1.5 and 3.2
- Triangularity, δ , varies between 0. and 1.0 .
- Fixed boundary safety factor q_ψ varies between 2.3 and 4.5
- Central safety factor q(0) is varied between 1.05 and 1.4
- $< \beta >$ is scanned continuously between 0 and 30 %.

3.2 Profiles

We have adopted model analytic tokamak profiles for the cases studied, requiring $q(0) \geq 1$, and $2.5 \leq q_{edge} \leq 4.5$. These profiles are adapted from optimal cases at other aspect ratios previously studied. A=1.67 [10], A=2.5 [11].

This choice of profiles is indicated by the fact that more detailed forms are unlikely to be better known for some time. Current drive will strongly influence q profiles and α heating will modify both pressure profiles and the stability criteria themselves.

A recurrent topic in ideal MHD analysis is the choice of a value for q(0). We seek to establish the limits of the ITER operating space, and thus wish to examine large scale modes likely to be accurately described by the MHD approximation, and unlikely to be non-linearly stabilised. In this regard, ideal MHD modes for profiles with $q(0) < 1$ have recently been proposed as a possible mechanism for triggering the internal sawtooth oscillation.[12] As sawtooth modes *per se* do not limit the operating space of tokamaks, although they have an important effect on confinement, we will impose the constraint $q(0) > 1$.

The approach described here complements that of other groups:

- Special 'Ohmic' current density profiles have been examined for CIT [13]
- A few configurations (A=3.6, $\kappa = 2, \delta = .25, 0.4$) have been studied for NET,[14], for which the current density profile is optimised according to the Lausanne procedure for the zero-β external kink.
- The role of edge current density, with

$$< j_\phi >= C \cdot (1 - \psi^\alpha)^\beta$$

has been examined for a limited number of configurations (A=4, κ=1.6, δ=.3, with possible up-down asymmetry), by the Keldysh group [5].

The p and q profiles we have used are of the general form:

$$p = p(0) \cdot \left((1. - \psi^{\alpha_0})^\beta + p_1 \psi^3 (1 - \psi)^{1.2}\right)$$

$$q = q(0) + q_1 \psi^{\alpha_1} + q_2 \cdot \psi^{\alpha_2}$$

p(0) has been varied to scan $< \beta >$.

q_{edge} has been varied between 2.3 and 4.5, and calculations have been done for q(0) between 1.05 and 1.4.

The choice q_2=0 for the q profile produces a broad central low shear region, which is susceptible to Mercier and 'infernal' modes. To avoid these modes, profiles with with q_2 = 0.5 and α_2 = 2 have been used for the majority of cases..

To obtain high shear in the region with large pressure gradients, the we chose α_1 = 6.

Figure 1a shows the range of q profiles used for the study, and Figure 1b depicts the (normalised) pressure profiles.

Figure 2 shows a typical current density profile which results from using these p and q profiles. Note that there is a nonzero edge current density, resulting from the fact that the q-profile is chosen rather than j_ϕ. Typically, the the ratio of edge to peak j_ϕ ranges from 10-30 % in the cases studied. The β_{crit} estimates are thus expected to be conservative, since external modes due to this non-zero edge current density could, in principle, be optimised further. Note, however, that feedback stabilisation of highly elongated configurations will

continuously generate edge currents in the actual device, so these current density pedestals are not unrealistic.

3.3 Configurations

The equilibrium calculations all assume a fixed external boundary. The shape parameters are defined by the equations for the outermost flux surface:

$$X = X_0 + \epsilon \cdot cos(\theta + \delta sin\theta)$$

$$Z = \kappa \cdot \epsilon \cdot sin\theta$$

The elongation (κ) and triangularity (δ) values quoted are those used in these equations, and the aspect ratio A $\equiv 1/\epsilon$.

3.4 Scope of the equilibrium database

An overall view of the equilibrium characteristics of the ITER cases in the database is shown in Figure [3], for which the β_{pol} vs ℓ_i 'operating space' is depicted. The use of a variety of profiles in the calculations approximately simulates the conditions under which experimental β-limit data is assembled from a series of experiments employing varying techniques for fuelling and current programming. Figure [4] depicts the extent of the coverage in $< \beta > -\kappa$ space. equilibrium calculations well in excess of the expected β limit are required to establish the kink limits for modes with n > 1, to aid in the unstable mode diagnosis by examining cases with the conducting shell on the plasma, and to serve as input data for future kinetic analysis which includes the effects of α particle populations.

4. STABILITY CALCULATIONS

4.1 Codes used, mode and wall parameters

The PEST code system has been used to evaluate stability. For the great majority of cases we have used Pest 2.4, which eliminates the sound continuum by solving an artificial minimisation problem for marginal stability. Pest 1 is used in a relatively small number of cases to compute the mode eigenfunctions to establish the characteristics of the limiting boundaries in the operating space.

The stability study examines both low-n and localised modes. For the cases in this report the stability of the n=1 and 2 kinks has been tested, along with the ideal ballooning and Mercier criteria.

For the majority of cases discussed we have assumed that the conducting wall is located at an infinite distance from the last flux surface. However, as part of the wall effects issue discussed in Section 2.4, we have also examined cases with a perfectly conducting shell on the plasma boundary and at b /a = 1.5 (b is the shell radius, a is the plasma radius, and the shell is assumed to be conformal with the plasma shape).

4.2 Overall stability results

Before discussing the stability results in detail, the overall aspects of the stability operating boundary deserve comment.

Experimental results are often compared with the Troyon-Gruber parameter, proposed to bound the maximum attainable β due to ideal modes:

$$C_T \equiv < \beta > / \frac{0.010\mu_0 I}{aB}$$

In general, when this parameter is compared with measurements, there is a trend apparent, as illustrated in Figure [5], from [15]. The Doublet III operating space for $1.4 < \kappa < 1.6$, and $2.3 < q_{edge} < 2.6$ is bounded for low ℓ_i by a disruptive limit unrelated to $< \beta >$, while for higher ℓ_i a pressure limit is seen. The conclusion drawn by the Doublet III group is that broad current density profiles are required for high β, since the highest values of the C_T parameter occur for the lowest values of ℓ_i consistent with the hard disruption limit.

Comparing the results in a similar fashion from the ITER database as a whole, we find a similar pattern. Figure [6a] shows the space surveyed for $\kappa = 2.$, and $3.1 < q_{edge} < 4.1$. Figure [6b] shows that there is a low-n limit in C_T - ℓ_i space, while Figure [6 c] shows a ballooning limit. The overall trend is similar to that of the reported Doublet III operating space.

The validity of the C_T parameter as a guide to stability is illustrated in Figures [7a,b]. In Figure [7a], all the ITER cases in the ORNL database are shown in the C_T vs I plot. (Current is normalised). In Figure [7b] only the n=1 stable cases are shown for the same space. We see that C_T = constant gives a reasonably good description, but that there is some degradation at high current. Further discussion of this point is deferred until the next section.

5. RESULTS

5.1 Optimal elongation

To establish the dependence of stability on elongation for these profiles, we examine separately the cases δ=0.4 and $\delta = 0.2$.

In addition, we take aspect ratio A=2.9 and $q_\psi = 3.1$. Results for q(0) = 1.05, 1.2 and 1.4 are included. (More detailed analysis of the dependence on q is presented in section 5.3).

5.1.1 Case with $\delta = 0.4$

The results of the study of optimal elongation for $\delta = 0.4$ are shown in Figure [8a-e].

Figure [8a] shows the dependence of the ballooning limit on κ. A monotonic increase in β_{crit} is found as κ increases. This dependence $\beta_{crit}(\kappa)$ is sensitive to details of the pressure profile. The solid curve in Figure [8a] shows the limiting case for which the pressure profile parameter p_1 in equation (2.1) equals 2. The dotted line in Figure [8a] shows the limiting curve for the case when p_1=0. For the narrower pressure profile, there is an increase in β for $\kappa < 2.5$, followed by a decline for larger values.

Figure [8b] shows the κ dependence of the n=1 limit. The ballooning limit is dominant for $\kappa < 2$, and there is a strong decline in β_{crit} for $\kappa > 2.5$ as was seen for ballooning stability with p1=0. The n=1 mode is not stongly affected by the pressure gradient, and cases with p_1=2 and p_1=0 produce similar scaling. This result coincides with that found by the Lausanne group [13], who have shown that n=1 stability is most strongly influenced by β_{pol}, and not by the local pressure gradient.

Figure [8c] shows the maximum stable values in the database as a function of κ, for both ballooning and n=1 stability, for $\delta = 0.4$.

For the profiles chosen, the n>1 limit in general lies above the n=1 limit. Figure [8d] shows the dependence of n=2 stability on κ. β_{crit} is slightly increasing for $\kappa > 2.5$.

Figure [8e] shows the dependence of the Troyon-Gruber parameter on κ for low and high-n modes. C_T slightly increases for $\kappa < 2.5$, and declines for larger values.

5.1.2 Case with $\delta = 0.2$

Similarly, results have been obtained for the case $\delta = 0.2$. These are shown in Figure [9a-b]. Figure [9a] shows the dependence $< \beta(\kappa) >^{max}$ for ballooning modes and n=1 modes for the $\delta = 0.2$ case, along with the comparable results discussed previously for $\delta = 0.4$. Figure [9b] shows the same comparison for C_T as a function of κ.

We see that increasing the triangularity from 0.2 to 0.4 increases $< \beta >^{max}$ by 30 % , while the optimal κ is ~ 2.5 . However, the dependence of optimal C_T varies with δ. For $\delta = 0.4$, the highest stable value of C_T is reached for $\kappa = 2. \rightarrow 2.8$, while κ^{opt} is 2.2 for $\delta = 0.2$

5.1.3 Trend

The picture which emerges from these results is that there is a peak in stability for $\kappa \sim 2. - 2.5$, followed by a decline for higher elongations.

It should be noted that axisymmetric modes will also be important for such configurations, and that ITER studies of n=0 modes are underway.

5.2 Optimal triangularity

To study the dependence of β_{crit} and C_T on δ we consider scaling with fixed elongation for two cases : $\kappa = 2.0$ and 2.5 . The other parameters are as chosen in section 5.1 .

5.2.1 Case with $\kappa = 2.0$

Figure [10a] shows the dependence of β^{max} on δ for n=1 and ballooning for $\kappa = 2.0$. As expected the ballooning stability is most sensitive to triangularity, while the n=1 boundary is improved with the increase in total current. For larger triangularity , the n=1 limits grow slowly with δ.

Figure [10b] shows the n=1 and ballooning dependence $C_T^{max}(\delta)$ at $\kappa = 2.0$. As expected from the steady rise of β_{crit} with δ. the Troyon parameter is relatively constant. This is a favorable result, in that there is no deterioration of MHD stability with increase in δ, although the current is increasing. Thus. since confinement and density limits rise with I, an overall improvement in performance can be expected.

5.2.1 Case with $\kappa = 2.5$

Figure [11a] shows the dependence of β^{max} on δ for n=1 and ballooning for $\kappa = 2.5$. β_{crit} rises with δ for $\delta \leq 0.5$, then saturates and declines.

Figure [11b] shows the n=1 and ballooning dependence $C_T^{max}(\delta)$ at $\kappa = 2.5$ The Troyon constant has a peak at $\delta = 0.5$. This result implies that there is a deterioration in the benefits of triangularity at higher elongation.

5.2.3 Trend

Since there is overall growth in β^{max} and relative constancy of C_T^{max} with increase in δ, further improvement can be expected in the ITER-3 design β limit if the triangularity were to be increased from 0.4 .

5.3 Dependence on q : 'Ravines'

The trends observed for the maximum values of β and C_T in the database will depend on the assumed values of the safety factor. Thus, calculations have been made to assess the sensitivity to q(0) and q_{edge}. The parameters varied in this study are:

A = 2.9
δ = 0.2 , 0.4
κ = 1.6 → 3.2
q(0) = 1.05 , 1.2 , 1.4
q_{edge} = 3.1 , 3.6 , 4.1

5.3.1 Variation with q_{edge}

The variation of ballooning and n=1 limits is discussed separately for $\delta = 0.2$ and 0.4 .

5.3.1.1 q_{edge} variation for $\delta = 0.4$

We first consider the nominal ITER reference case with $\delta = 0.4$.

The sensitivity of the $< \beta >$ limit to q_{edge} is shown in Figures [12a-c] for ballooning and in Figures [13a-c] for the n=1 mode. The $< \beta > (\kappa)$ dependence is shown separately

for q(0) = 1.05, 1.2, and 1.4 in Figures [12a-c] for ballooning and in Figures [13a-c] for n=1.

For $\kappa < 2.5$, the ballooning limits decrease as q_{edge} is increased from 3.1 to 4.1, recalling the simple analytic scaling $\beta_{crit} \sim \epsilon/q^2$.

For higher κ, there is a more complex structure, and saturation and decline is observed for q(0) = 1.2

The n=1 stability limits show the effect of 'ravines' found earlier by the Keldysh and Lausanne groups. The low-n limits are the most stringent for $\kappa > 2.5$, and thus set the overall limit.

5.3.1.2 q_{edge} variation for $\delta = 0.2$

The next series of results examines the stability limit variation with q_{edge} for $\delta = 0.2$ .The $< \beta(\kappa) >$ curves for q_{edge} = 3.1, 3.6, and 4.1 are shown.

For $\delta = 0.2$, the ballooning limits show relatively little variation with q_{edge}, as seen in Figures [14a-c] for q(0) = 1.05, 1.2, and 1.4, respectively. In each case there is an optimal κ at ~ 2.5, and a slight decrease in β^{max} as q_{edge} is increased from 3.1 to 4.1 .

The n=1 limits behave similarly to the $\delta = 0.4$ case (Figures 15 a,b]). There is a moderate 'ravine' for the q_{edge} = 3.6 case, as at the higher triangularity, and, again, the n=1 mode sets the upper limit for $\kappa > 2.5$.

5.3.2 Variation with q(0)

Just as in the case with q_{edge} variation, varying q(0) with fixed q_{edge} can be expected to show structure . As in Section 5.3.1, we discuss the cases $\delta = 0.2$ and 0.4 separately.

5.3.2.1 Case with $\delta = 0.4$

Beginning with the nominal ITER reference case, $\delta = 0.4$, the ballooning limits $< \beta(\kappa) >$ are shown in Figures [16a-c] for q_{edge} = 3.1, 3.6 and 4.1, respectively, while the n=1 limits are shown in Figures [17a-c].

The ballooning limits show a generally increasing behavior as a function of κ, with slight variation as a function of q(0). There is some structure for $\kappa > 2.5$, for q(0) = 1.2, but overall there is a slight decrease in β_{crit} with increasing q(0).

The n=1 limits again show the 'ravine' structure associated with resonances. As seen in Figure [17b], there is again a pronounced dip in β_{crit} for $q_{edge} = 3.6$, both for q(0)= 1.05 and q(0) = 1.2 . For cases away from resonance, there is a maximum κ at 2.5, and constant or declining β for $\kappa > 2.5$.

5.3.2.2 Case with $\delta = 0.2$

For the case, $\delta = 0.2$, the ballooning limits $< \beta(\kappa) >$ are shown in Figures [18a-c] for q_{edge} = 3.1, 3.6 and 4.1. respectively, while the n=1 limits are shown in Figures [19a-c]

The ballooning limits are similar to those seen with $\delta = 0.4$, except that the peak κ is slightly smaller, 2.3 as compared with 2.5 for higher triangularity.

The n=1 limits at $\delta = 0.2$ also show a less pronounced 'ravine' structure for q_{edge} = 3.6. As seen in Figure [19b], there is a dip in β_{crit} for $q_{edge} = 3.6$, both for q(0)= 1.05 and q(0) = 1.2 . For cases away from resonance, there is a maximum κ at 2.3, and constant or declining β for $\kappa > 2.3$.

5.3.3 Trends

The complex structure of the operating space is made evident by the separate studies of the dependence $< \beta(\kappa) >$ with q(0) and q_{edge} varied independently. It is important to note that scaling of β_{crit} with κ can vary strongly depending on the value of q_{edge}.

5.4 Wall effects

The preceding results all assumed a conducting wall at ∞. The effect of wall stabilisation on the external kink modes is well known. However, without a detailed poloidal coil design it is not possible to make a precise estimate of the effective wall radius, except to say that the ∞ wall results are pessimistic. To estimate the size of the effect we have re-studied the $< \beta(\kappa) >$ dependence for q_{edge} = 3.1. and q(0) = 1.05, 1.2 and 1.4, for $\delta = 0.4$. The wall positions chosen for comparison were b / a = 0, 1.5, and ∞ .

Results are shown for $< \beta^{max}(\kappa) >$ and $C_T^{max}(\kappa)$ in Figures [20-22a,b]. Figures [20-22a] show the β dependence, while Figures [20-22b] show the C_T scaling.

For each value of q(0) , the b/a = 0. and 1.5 cases have nearly the same behavior, and the b/a = ∞ case is pessimistic by a factor 2-3 for $\kappa > 2.5$. Only for q(0) = 1.4 is there an appreciable diminution of β_{crit} for the case b/a = 1.5 . The C_T variation (Figures [20-22b]) is relatively flat with κ, except for the case with wall at ∞ .

5.5 Aspect ratio scaling

To document the possible consequences of adopting a higher aspect ratio in the ITER design, calculations made for the earlier TIBER-II design, with A=3.6, are discussed. The parameters for this study are :

A = 3.6

$q_{edge} = 3.1 \rightarrow 4.5$

q(0) = 1.05

$\kappa = 1.5 \rightarrow 3.$

$\delta = 0.2 \rightarrow 0.6$

As seen from Figure [23], the dependence $\beta^{max}(\kappa)$ is similar to that at A = 2.9, however, the optimal κ lies somewhat lower, at $\kappa \sim 2.3$. The absolute values of β_{crit} are also lower at the higher aspect ratio, with $\beta^{max} \sim 8\%$. Thus, adopting a higher aspect ratio would bring a $\sim 50\%$ penalty in β_{crit}.

5.6 Current drive implications

The sensitivity of β limits to the current density profile is well known. Various schemes for current drive are being considered for the ITER design, with lower hybrid, bootstrap and neutral beam drive among them. These approaches are somewhat complementary , in that beam current drive could provide current density peaking, while LH and bootstrap currents can provide edge current density. Thus, all could be used to tailor MHD-stable profiles.

Figures [24a,b] show the dependence of stable cases in β_{pol} vs ℓ_i space, for ballooning and n=1 modes, respectively. As can be seen , the stability criteria favor high β_{pol} at high

ℓ_i. This may conflict with current drive requirements. For example, calculations of the dynamics of bootstrap current formation [16] show that the proportionality between j_{BS} and β_{pol} leads to production of a hollow current density profile (low ℓ_i) at high β_{pol}. This trend is opposite to that suggested by Figures [24a,b].

5.7 Transport self-consistency

Considerations of optimisation of neutron production lead to a need for centrally peaked pressure profiles [17]. These high-reactivity profiles enhance the fusion output for a given energy confinement time τ_E.

The impact of such profiles on ideal MHD stability is significant, though. The Table shows the results of a scan with the pressure profile parameter α of Section 3.2 taken to be 2.2 to coincide with confinement performance calculations. For this study $\kappa = 2.$, $\delta = 0.4$. $q(0) = 1.05$, $q_{edge} = 3.1$. For profiles which limit the β operating space, $< \beta >^{ballooning} \sim$ 7.5 %, and $< \beta >^{n=1} \sim$ 10.5 %. we see that the ballooning limit is reduced by a factor 3.5, and the low n limit by ~ 3 . It important to note that optimisation of this result is possible. Nevertheless, the reduction in C_T is substantial.

Table : Stability with peaked profiles

Beta	C_T	Baloon stable	Mode	Inf. Wall stable	b/a=1.5 stable
0.00	0.00		1		
			2		
0.68	0.24		1		
			2		
1.37	0.49		1		
			2		
2.07	0.73	No	1		
			2		
2.76	0.97	No	1		
			2		
3.46	1.22	No	1	No	No
			2		
4.16	1.46	No	1	No	No
			2		
4.87	1.70	No	1	No	No
			2	No	No

Note: Cases are stable unless noted

5.8 Mode identification

To decide whether the operating space boundaries represent substantial physical limits, rather than artifacts of the particular profiles chosen for study, it is necessary to compute the radial eigenfunctions for the cases lying on the stable-unstable boundary. From the large number of such operating space boundaries presented in the preceding sections, we choose to examine the bounding curve in $< \beta > -\kappa$ space discussed in 4.2.1. This study varied κ with δ fixed at 0.40, and with q(0)=1.05, q_{edge}=3.1

Figure [8a] reproduces the stable-unstable boundary, and three cases lying on the boundary are selected for further analysis. The parameters for these cases are:

$<\beta>$ (%)	κ	Equilibrium ID
12.5	2.4	ITR32
8.9	2.8	ITR54
3.5	3.0	ITR45

Figure [25a-c] shows the flux surface averaged toroidal current density as a function of effective radius for these three cases , and Figure [26a-c] shows the computed PEST 1 eigenfunctions for each.

The unstable mode structure for each of the cases is heavily dominated by external modes, with a large internal m=2 component. Thus, it is likely that there will be a strong effect from an external stabilising shell. It also appears that finite Larmor radius effects would not radically alter the stability picture for such a large-scale mode.

Analysis of these cases re-confirms the effect discussed earlier in Section 5.4. . Each case is found to be stable both with the wall located on the plasma surface and for b / a = 1.5 . Thus, the operating space boundary will be strongly influenced by wall effects.

5.9 Systems code interface

In order to describe the MHD limits in a form suitable for interface with the other constraints examined in tokamak reactor design (confinement scaling laws, poloidal field design criteria, etc.) we must express the results in the form of scaling fits . This task is greatly facilitated by the LOCUS database software developed at PPPL [5].

Before presenting the scaling fits, though, we discuss the appropriate variables to use in the fitting.

5.9.1 $\bar{q}$ compared with q^*.

The safety factor variable is sensitive to configuration for highly elongated and diverted plasmas. As has been discussed by Peng and Strickler [11], even highly elongated plasmas without an internal separatrix are influenced by the nearby separatrix in the vacuum field. Thus, artificially high values of safety factor may be computed in using such approximate formulae as that commonly used :

$$q^* = \frac{5}{2}\frac{a^2}{R^2 I}\left(1 + \kappa^2(1 + \delta^2)\right)$$

Figure [27a] shows the dependence of C_T on q* for ITER-3 cases with $1.6 \leq \kappa \leq 3.2$ and $\delta = 0.4$. The stable and unstable cases for n=1 modes , with the wall at ∞, are distinguished.

When described in terms of q*, the cases (all of which have $q_{MHD} \geq 3$), have q-values < 2. Furthermore, there is a relatively indistinct unstable boundary.

Figure [27b] shows the same cases. plotted as $C_T(\bar{q})$. The q values all lie above 2, and there is an obvious low-q limit due to large scale MHD modes.

Thus, $\bar{q}$ appears to represent a more natural choice for describing the scaling .

5.9.2 Scaling formulae

Figure [28a] shows the overall dependence $< \beta > (\bar{q})$ and Figure [28b] shows the $C_T(\bar{q})$ curve. There is a resonance structure visible, but the over-all scaling formulae are taken to average this detailed dependence away , yielding :

$$C_T = (-0.136019 \pm 0.116)\bar{q} - (2.86427 \pm 0.336)$$

More detailed fits to the individual cases discussed in sections 5.1 - 5.7 are given in Appendix 2.

6. CONCLUSIONS AND FURTHER WORK

The following conclusions emerge from the studies to date:

1. At the ITER-3 aspect ratio, the calculations support choosing elongation greater than 2. Optima lie in the range $2.2 \leq \kappa \leq 2.6$.
2. Triangularity is generally beneficial, and the calculations support an increase in the present upper limit ($\delta = 0.4$).
3. There are two countervailing effects not included in the bulk of the calculations :
   a. Non-optimal profiles, typical equilibria generated by transport codes
   b. Effect of an external conducting wall

   The first effect will reduce the expected β, while the second will increase it. Present indications are that the transport-related reduction is greater than the wall stabilisation.
4. The operating space is structured, and local unstable regions appear in the midst of generally stable zones. This phenomenon is correlated with resonant values of the safety factor. Scaling fits used in systems code analysis should account for this effect.
5. For the profiles chosen, current density profiles tending toward those typical of edge current drive schemes appear to reduce the β_{crit}. This tendency should be factored into the analysis of such scenarios.
6. The modes which limit the operating space are of a large-scale nature, and are thus appropriate predictions of a fluid-like theory.
7. A limited examination of aspect ratio scaling suggests that operation at a larger aspect ratio would reduce β_{crit}.

Further work is needed in a number of areas:

- we need to examine transport-relevant profiles more systematically, and to calculate the results using profiles from present β-limit experiments.
- an estimate of the magnitude of kinetic effects (especially α pressure) is needed.
- the changes introduced by nonlinear and resistive effects have to be studied

It is expected that evolution of the ITER design will occur. and we have constructed a flexible system for evaluating the consequences for MHD stability of such inevitable changes.

Acknowledgments

Discussions with B. A. Carreras and R.A. Dory have been instrumental in selecting the topics to explore. D. Pearlstein and W. Nevins of LLNL have helpfully provided the ITER perspective. M. Peng and D. Strickler of FEDC have represented the systems code viewpoint. J. Holmes of ORNL Computing and Telecommunications Division imported and installed the PEST codes used in the study, and has offered helpful advice both about numerical aspects and about MHD stability optimisation. J. Manickam of PPPL has collaborated with ORNL in the use of the PEST code suite.

REFERENCES

1. R.C. Grimm, J.M. Greene, J.L. Johnson. in Methods in Computational Physics, **16** (1976) 769; R.C. Grimm. R.L. Dewar. J. Manickam, Journal of Computational Physics, **49** (1983) 94

2. System 1032 User's Guide, Software House, Cambridge, MA. Sept. 1986

3. J. A. Murphy, LOCUS database system, ISAM version 5.0, Princeton Plasma Physics Laboratory internal memorandum, July 1987.

4. L. Degtyarev, S. Medvedev, A. Martynov, V. Drozdov, USSR contribution to INTOR Phase 2, Part3 workshop, (1987)

5. W.A. Cooper, F. Yasseen, F. Troyon, T. Tsunematsu, A. Turnbull, Spring College of Plasma Physics, 114.SMR/210-40, 1987.

6. J.L. Perkins, Internal memorandum LLNL-ITER-88-021

7. C. Henning, B. Logan, Journal of Fusion Energy, **6**(1987) 241

8. B.A. Carreras, L. Charlton, J. Hogan et al, in Plasma Physics and Controlled Nuclear Fusion, Proc. 11th Internat. Conf., Kyoto, paper IAEA-CN-47/E-I-2-4, Vienna, 1987

9. Y-K. M. Peng, D.J. Strickler, Nuclear Fusion **26** (1986) 769

10. J. Delucia, S.C. Jardin, A.M.M. Todd, Princeton Plasma Physics Laboratory Report PPPL-1564, (1979)

11. F. Troyon, R. Gruber, H. Saurenmann, S. Semenzato, and s. Succi, Plasma Physics and Controlled Fusion, **26** (1984) 209

12. J. Holmes, B. Carreras, L. Charlton et al. Oak Ridge National Laboratory Report ORNL/TM-10585, Sept. 1987.

13. M. Phillips, A.M.M. Todd. M. Hughes, Sherwood Theoretical Meeting, April 6-8, 1987, San Diego, Ca.

14. W. A. Cooper, F. Yasseen, F. Troyon, A. Roy. Workshop on plasma theory, Varenna, 1987.

15. E. Strait, Proc. US-Japan workshop on high-beta tokamaks, San Diego, Jan. 1987.

16. J. Hogan , Nuclear Fusion, 21 (1981) 365

17. N. Uckan, private communication

FIGURE CAPTIONS

Figure 1a q profiles used in ITER study as a function of poloidal flux.

Figure 1b Normalised pressure profiles used in ITER study, as a function of poloidal flux.

Figure 2 Typical j_ϕ profile, with $\sim 10\ \%$ edge current density pedestal, as a function of $\psi^{1/2}$

Figure 3 ITER $\beta_{poloidal}$ vs ℓ_i operating space surveyed for MHD stability.

Figure 4 ITER $< \beta >$ - κ space surveyed for stability.

Figure 5. Operating space for the Doublet III tokamak, as a function of the Troyon-Gruber parameter C_T and the internal inductance, ℓ_i, for $1.4 < \kappa < 1.8$, and $2.3 < q_{edge} < 2.8$.

Figure 6a Cases surveyed for ITER, in C_T - ℓ_i space, for $\kappa = 2.$, and $3.1 < q_{edge} < 4.1$.

Figure 6b Cases in Figure 6a with n=1 instability.

Figure 6c Cases in Figure 6b with ballooning instability.

Figure 7a Overall view of the dependence of C_T on current for the database.

Figure 7b Stable cases in the database.

Figure 8a Dependence of ballooning $< \beta_{crit} >$ on κ for q(0) = 1.05 and q_{edge} = 3.1 , δ=0.4, and for pressure profile parameter p_1=0. and 2.

Figure 8b Dependence of n=1 limit $< \beta_{crit} >$ on κ with δ=0.4, for q(0) = 1.05 and q_{edge} = 3.1

Figure 8c Combined n=1 and ballooning limits for δ=0.4.

Figure 8d n=2 stability limit for the conditions of Figures 8a-c.

Figure 8e C_T vs κ for the conditions of Figures 8a-d.

Figure 9a Ballooning limit for q(0)=1.05, q_{edge}=3.1, δ = 0.2.

Figure 9b n=1 stability limit for conditions of Figure 9a.

Figure 10a Dependence of $< \beta_{crit} >$ on triangularity for κ=2.

Figure 10b Dependence of C_T on triangularity for κ=2.

Figure 11a Dependence of $< \beta_{crit} >$ on triangularity for κ=25.

Figure 11b Dependence of C_T on triangularity for κ=2.5

Figure 12a Ballooning stability : $< \beta >$ vs κ for δ=0.4. q(0)=1.05. The 3 cases shown are : q_{edge} = 3.1, open circles, 3.6, black circles, and 4.1. triangles.

Figure 12b Same as Figure 12a for q(0)=1.2

Figure 12c Same as Figure 12a for q(0)=1.4

Figure 13a n=1 stability : $< \beta >$ vs κ for δ=0.4, q(0)=1.05. The 3 cases shown are : q_{edge} = 3.1, open circles, 3.6, black circles, and 4.1, triangles.

Figure 13b Same as Figure 13a for q(0)=1.2

Figure 13c Same as Figure 13a for q(0)=1.4

Figure 14a Ballooning stability : $< \beta >$ vs κ for δ=0.2. q(0)=1.05. The 3 cases shown are : q_{edge} = 3.1, open circles, 3.6, black circles, and 4.1, triangles.

Figure 14b Same as Figure 14a for q(0)=1.2

Figure 14c Same as Figure 14a for q(0)=1.4

Figure 15a n=1 stability : $< \beta >$ vs κ for δ=0.2, q(0)=1.05. The 3 cases shown are : q_{edge} = 3.1, open circles, 3.6, black circles, and 4.1, triangles.

Figure 15b Same as Figure 15a for q(0)=1.2

Figure 15c Same as Figure 15a for q(0)=1.4

Figure 16a Ballooning stability : $< \beta >$ vs κ for δ=0.4. open circles are q(0) = 1.05. dark circles q(0)=1.2. q_{edge}=3.1.

Figure 16b same as Figure 16a for q_{edge}=3.6

Figure 16c Same as Figure 16a for q_{edge}=4.1

Figure 17a n=1 stability : $< \beta >$ vs κ for δ=0.4, open circles are q(0) = 1.05, dark circles q(0)=1.2. q_{edge}=3.1.

Figure 17b Same as Figure 17a for q_{edge}=3.6

Figure 17c Same as Figure 17a for q_{edge}=4.1

Figure 18a Ballooning stability : $< \beta >$ vs κ for δ=0.2, open circles are q(0) = 1.05, dark circles q(0)=1.2. q_{edge}=3.1.

Figure 18b Same as Figure 18a for q_{edge}=3.6

Figure 18c Same as Figure 18a for q_{edge}=4.1

Figure 19a Ballooning stability : $< \beta >$ vs κ for δ=0.2, open circles are q(0) = 1.05, dark circles q(0)=1.2. q_{edge}=3.1.

Figure 19b Same as Figure 19a for q_{edge}=3.6

Figure 19c Same as Figure 19a for q_{edge}=4.1

Figure 20a Dependence $< \beta >$ on κ for δ = 0.4, q_{edge} = 3.1. The three curves are : open circles, b / a = 0., closed circles, b / a = 1.5, triangles , b / a = ∞.

Figure 20b Dependence C_T on κ for δ = 0.4, q_{edge} = 3.1. The three curves are : open circles, b / a = 0., closed circles, b / a = 1.5, triangles , b / a = ∞.

Figure 21a Dependence $< \beta >$ on κ for δ = 0.4, q_{edge} = 3.6 The three curves are : open circles, b / a = 0., closed circles, b / a = 1.5, triangles , b / a = ∞.

Figure 21b Dependence C_T on κ for δ = 0.4, q_{edge} = 3.6 The three curves are : open circles, b / a = 0., closed circles, b / a = 1.5, triangles , b / a = ∞.

Figure 22a Dependence $< \beta >$ on κ for δ = 0.4, q_{edge} = 4.1 The three curves are : open circles, b / a = 0., closed circles, b / a = 1.5, triangles , b / a = ∞.

Figure 22b Dependence C_T on κ for $\delta = 0.4$, $q_{edge} = 4.1$ The three curves are : open circles, b / a = 0., closed circles. b / a = 1.5, triangles , b / a = ∞.

Figure 23 $< \beta_i >$ vs κ for $0.3 < \delta < 0.4$ at A=3.6 . q(0) = 1.05, $q_{edge} = 3.1$.

Figure 24a Ballooning stability for $\kappa = 2.$, $\delta = 0.4$. in $\beta_{poloidal}$ vs ℓ_i space for A=2.9

Figure 24b n=1 stability for $\kappa = 2.$, $\delta = 0.4$, in $\beta_{poloidal}$ vs ℓ_i space for A=2.9

Figure 25a Toroidal surface-averaged current density as a function of minor radius for case ITR32.

Figure 25b Toroidal surface-averaged current density as a function of minor radius for case ITR54.

Figure 25c Toroidal surface-averaged current density as a function of minor radius for case ITR45.

Figure 26a PEST 1 eigenfunction arrow plot for case ITR32.

Figure 26b PEST 1 eigenfunction arrow plot for case ITR54.

Figure 26c PEST 1 eigenfunction arrow plot for case ITR45.

Figure 27a C_T vs q^* for $1.6 \leq \kappa \leq 3.2$, and $\delta = 0.4$.

Figure 27b C_T vs $\bar{q}$ for $1.6 \leq \kappa \leq 3.2$, and $\delta = 0.4$.

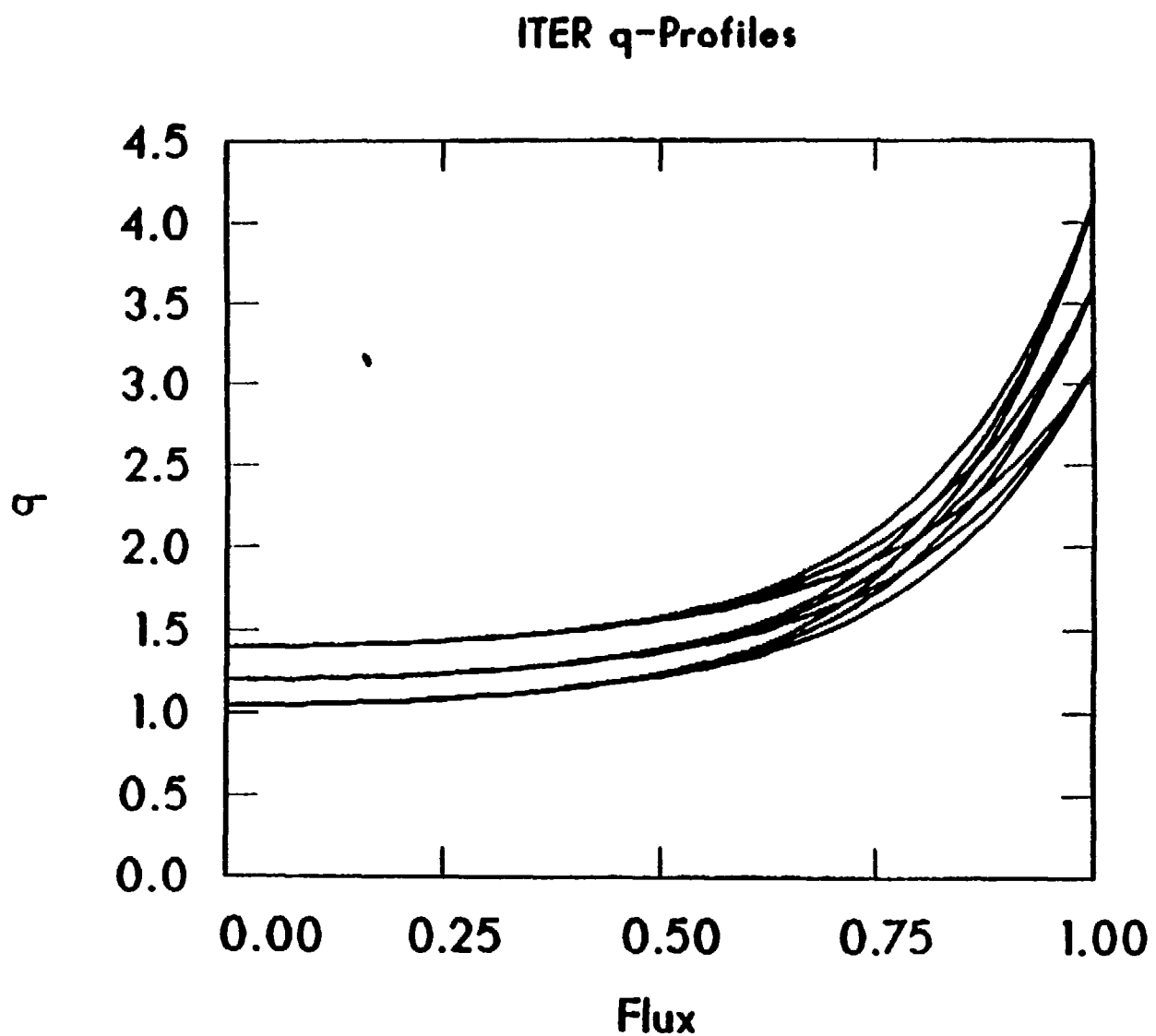
ITER q-Profiles
4.5
4.0
3.5
3.0
2.5
2.0
1.5
1.0
0.5
0.0
q
0.00
0.25
0.50
0.75
1.00
Flux

1a

ITER PRESSURE PROFILES

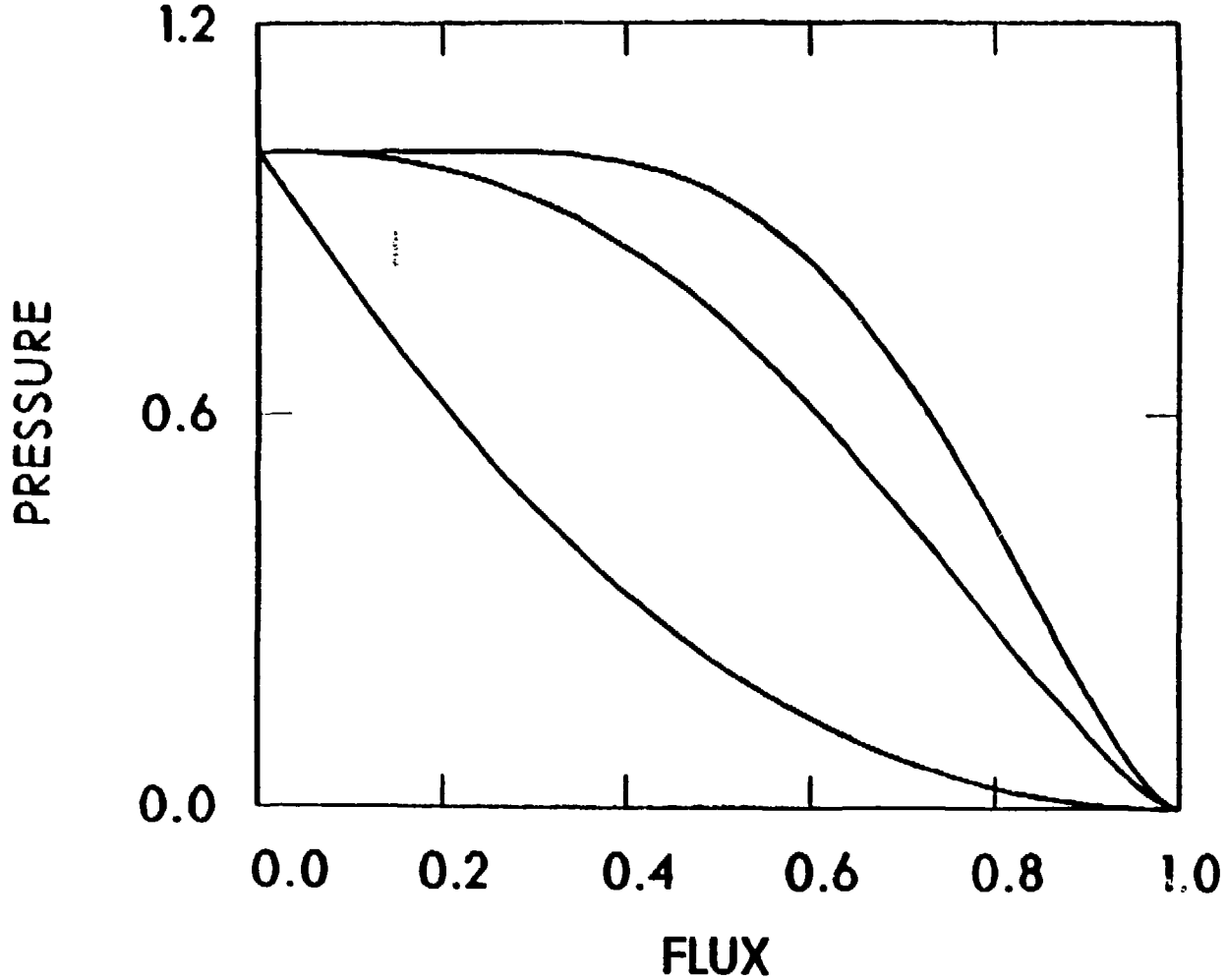

TOROIDAL CURRENT DENSITY
ITER-3 EQUIL_ID= ITR32

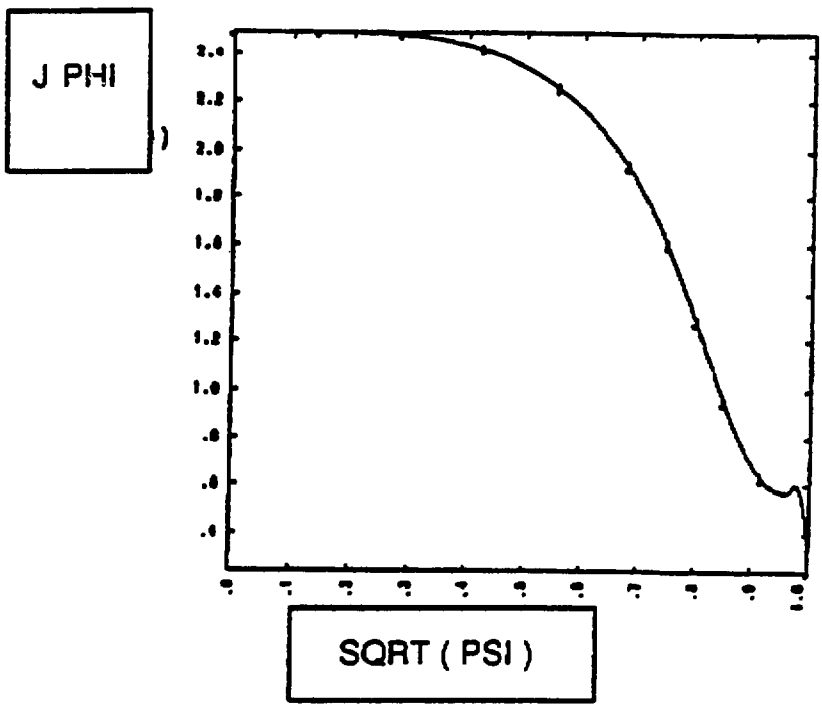

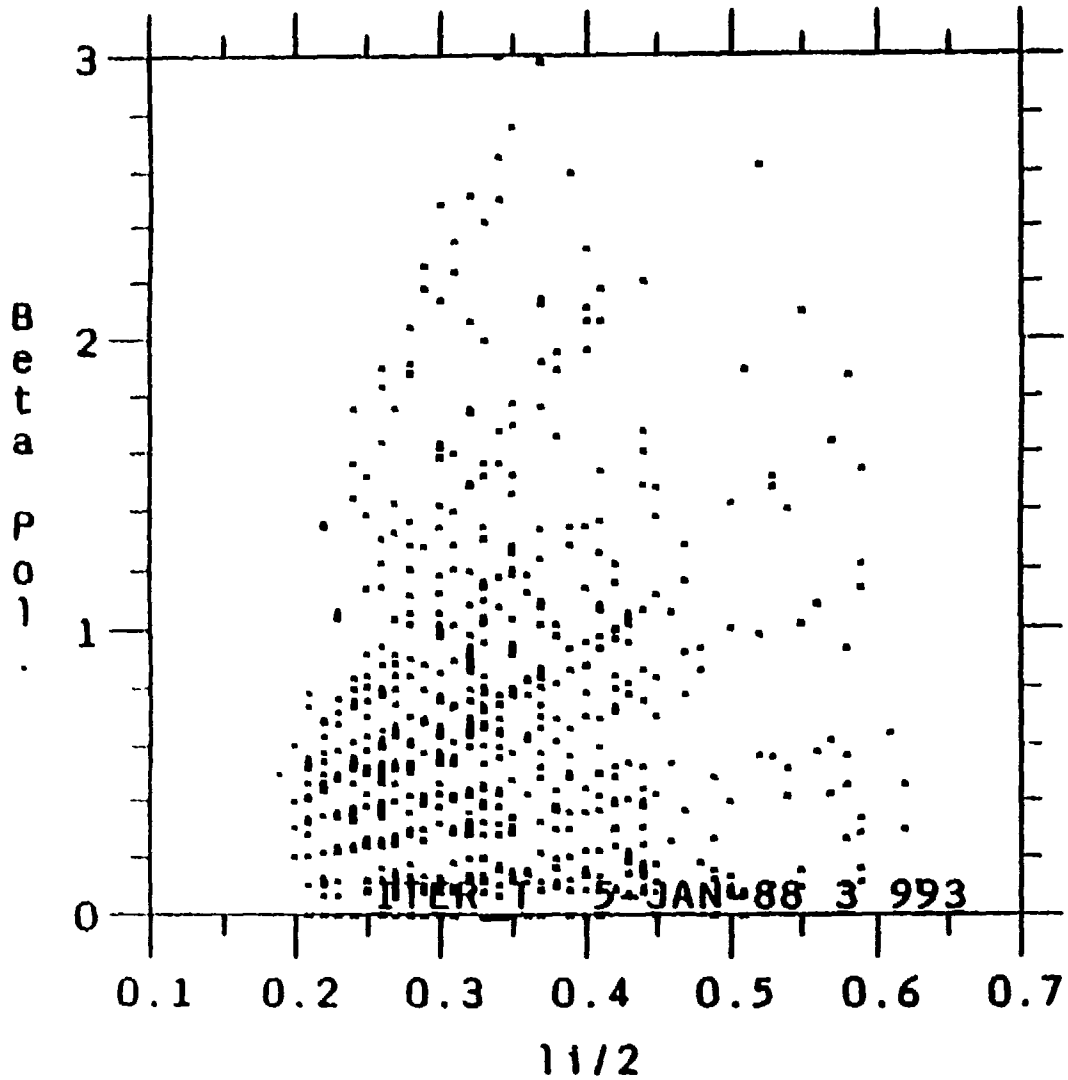

(3)

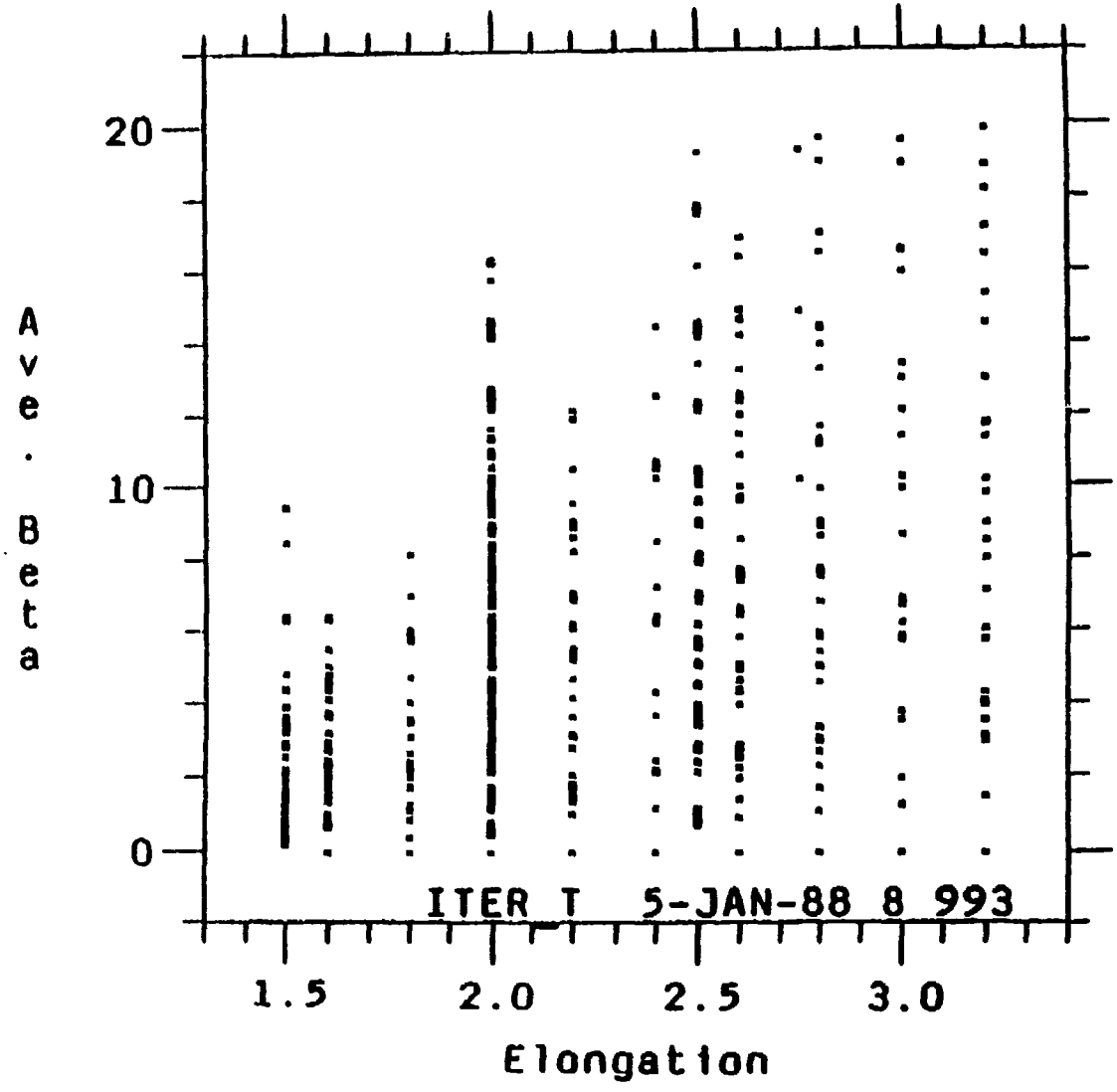

④

DIII OPERATING SPACE
2.3 < q < 2.6
1.4 < KAPPA < 1.6

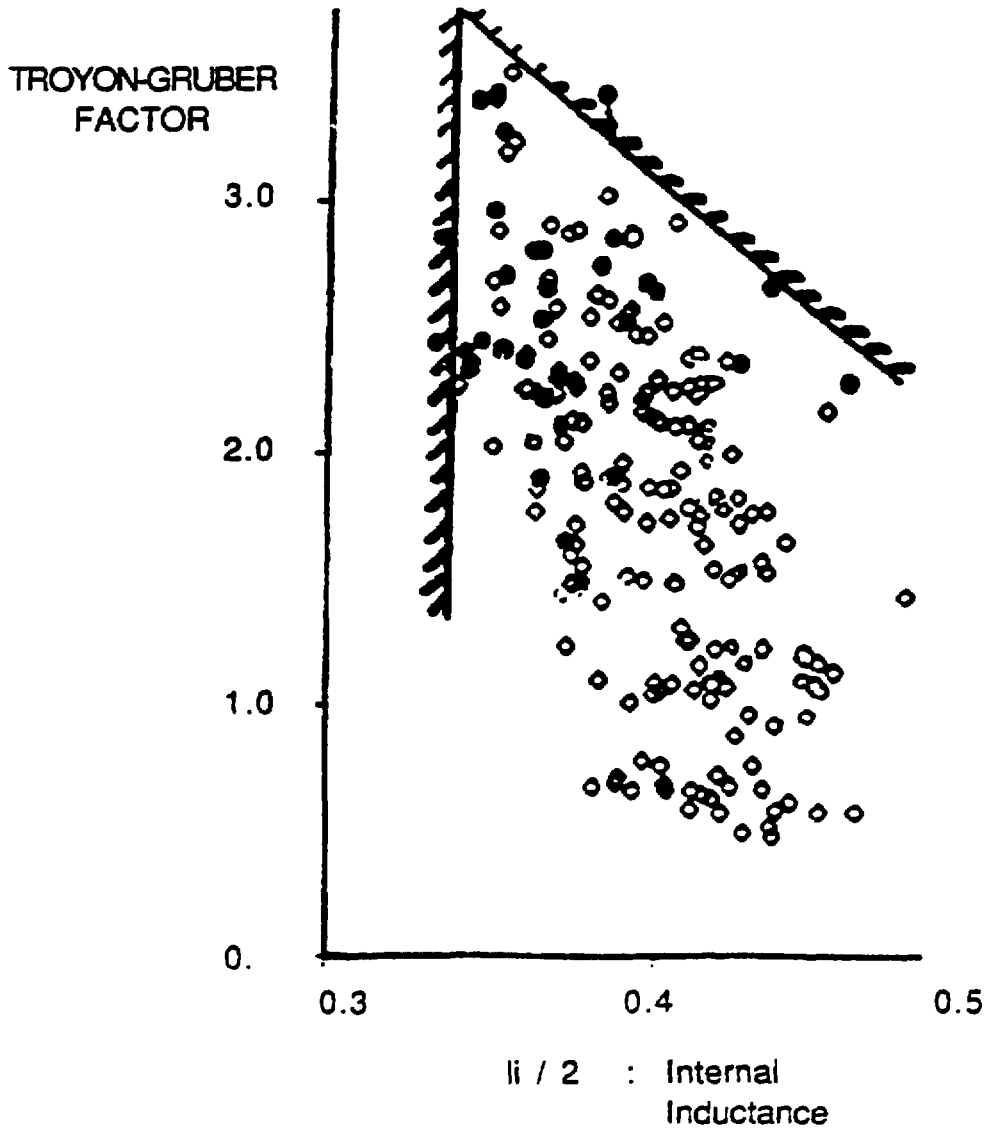

Reference : E.J. Strait
US-JAPAN HIGH-BETA WORKSHOP
San Diego, January 1987

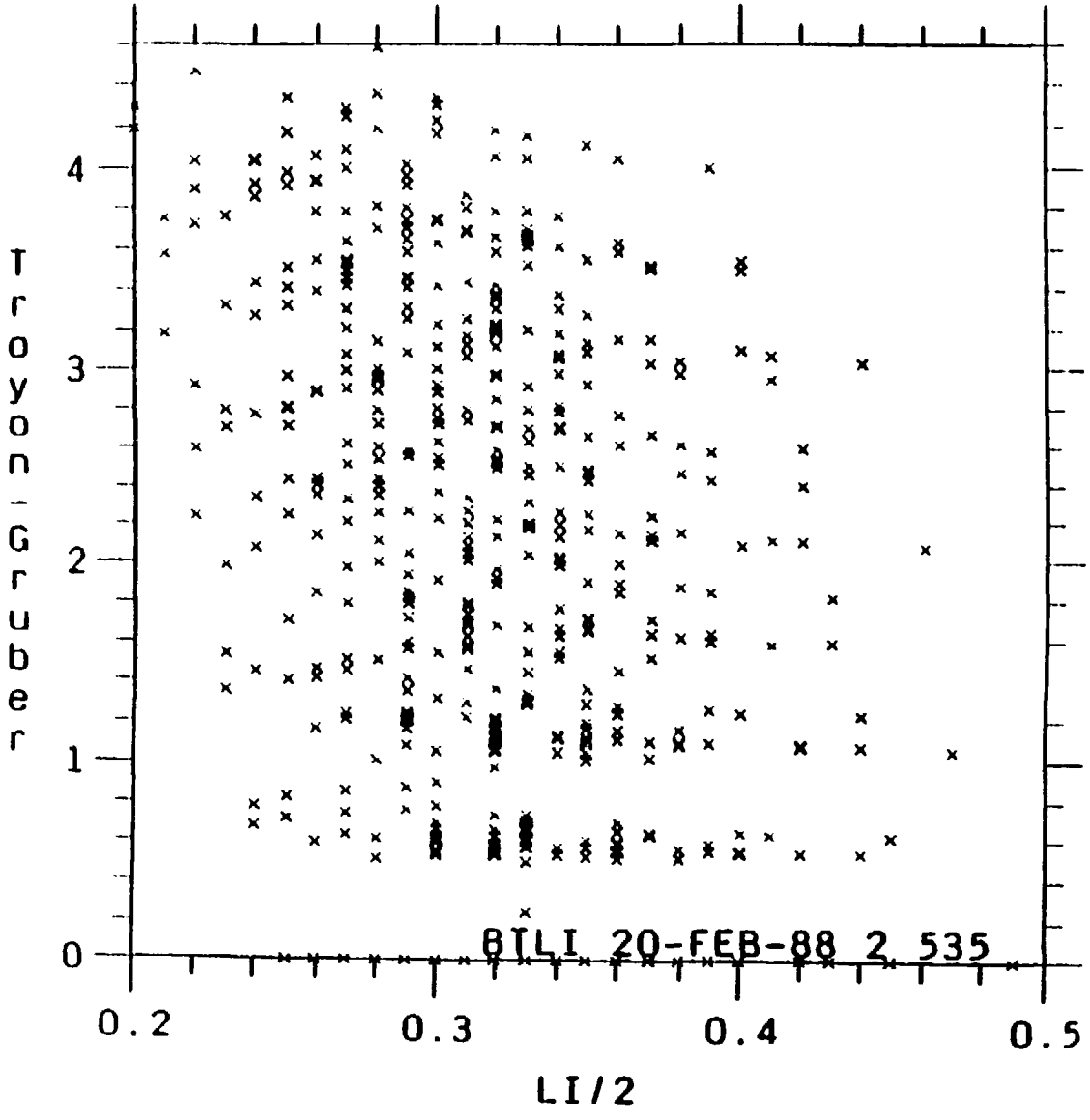

164

PESST=0

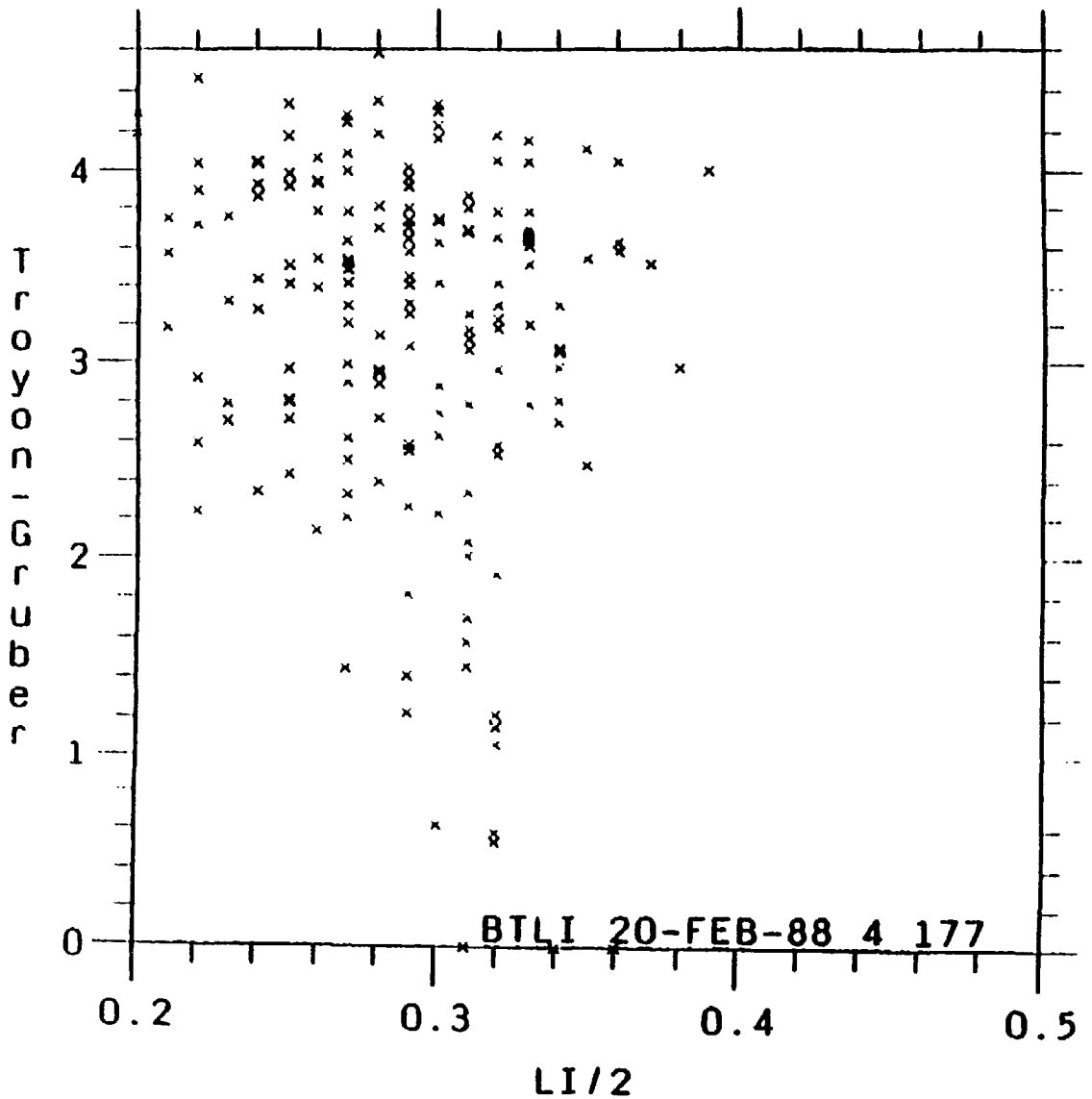

BALST=0

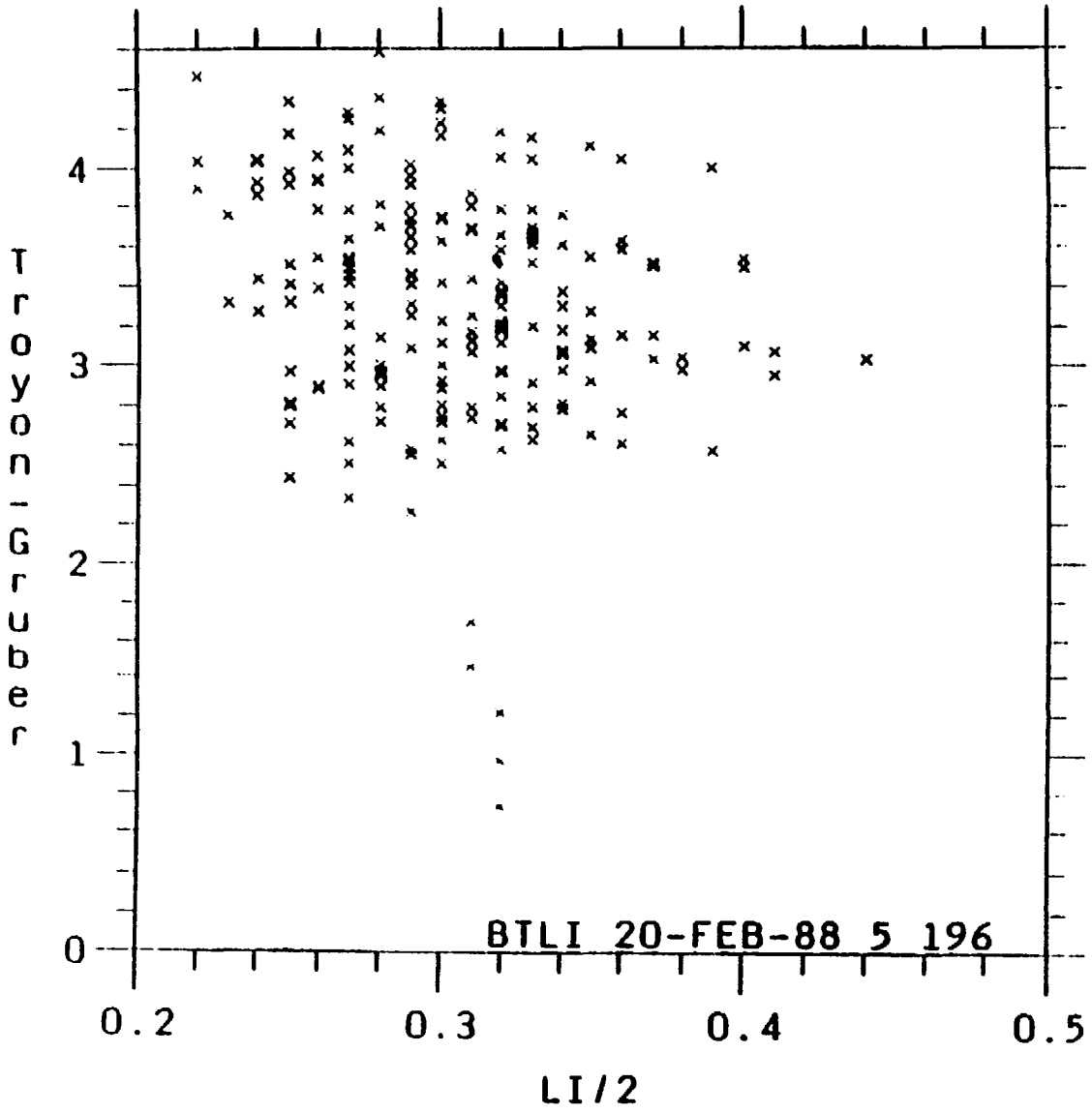

(6c)

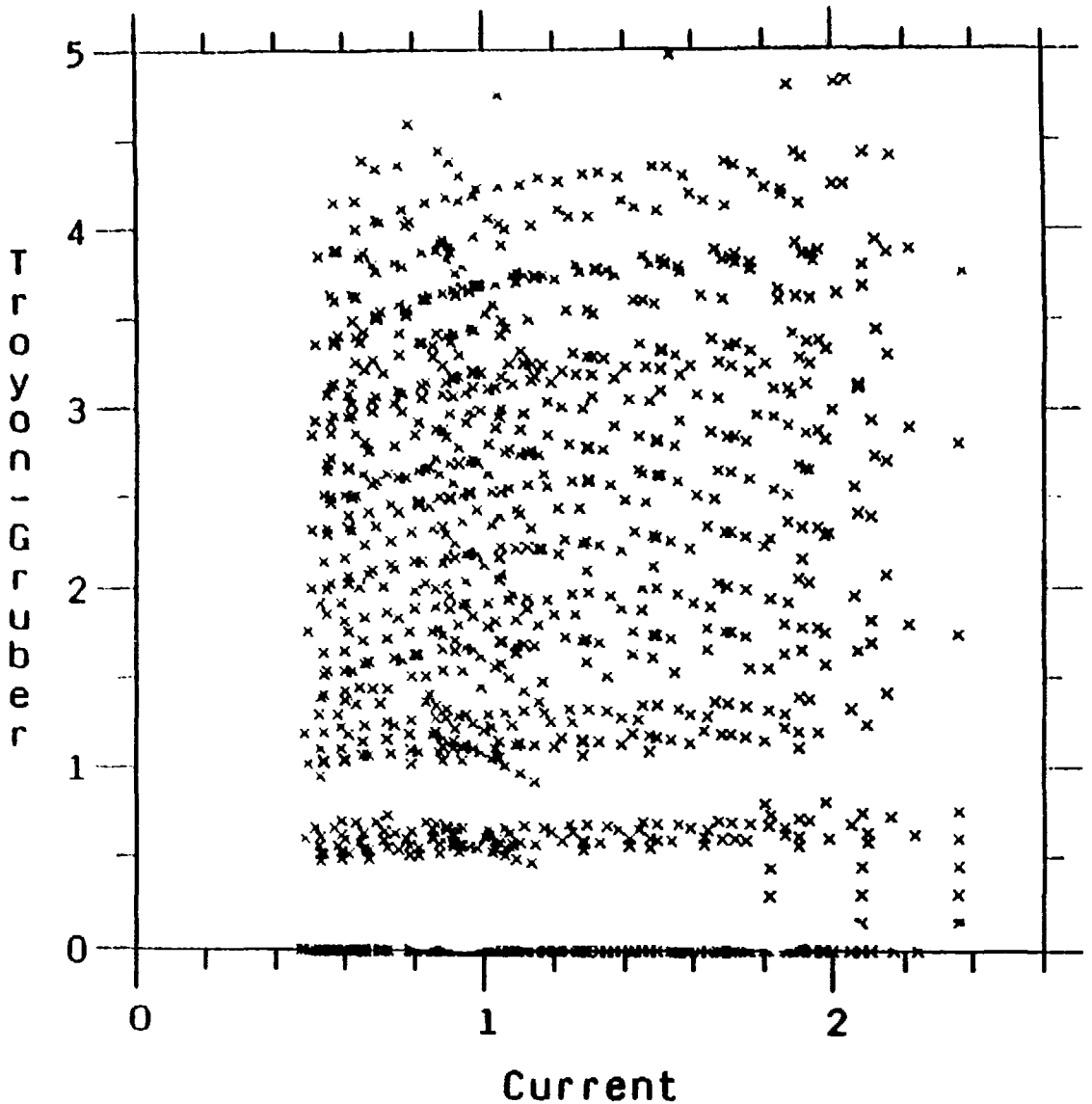

(19)

PESST=1

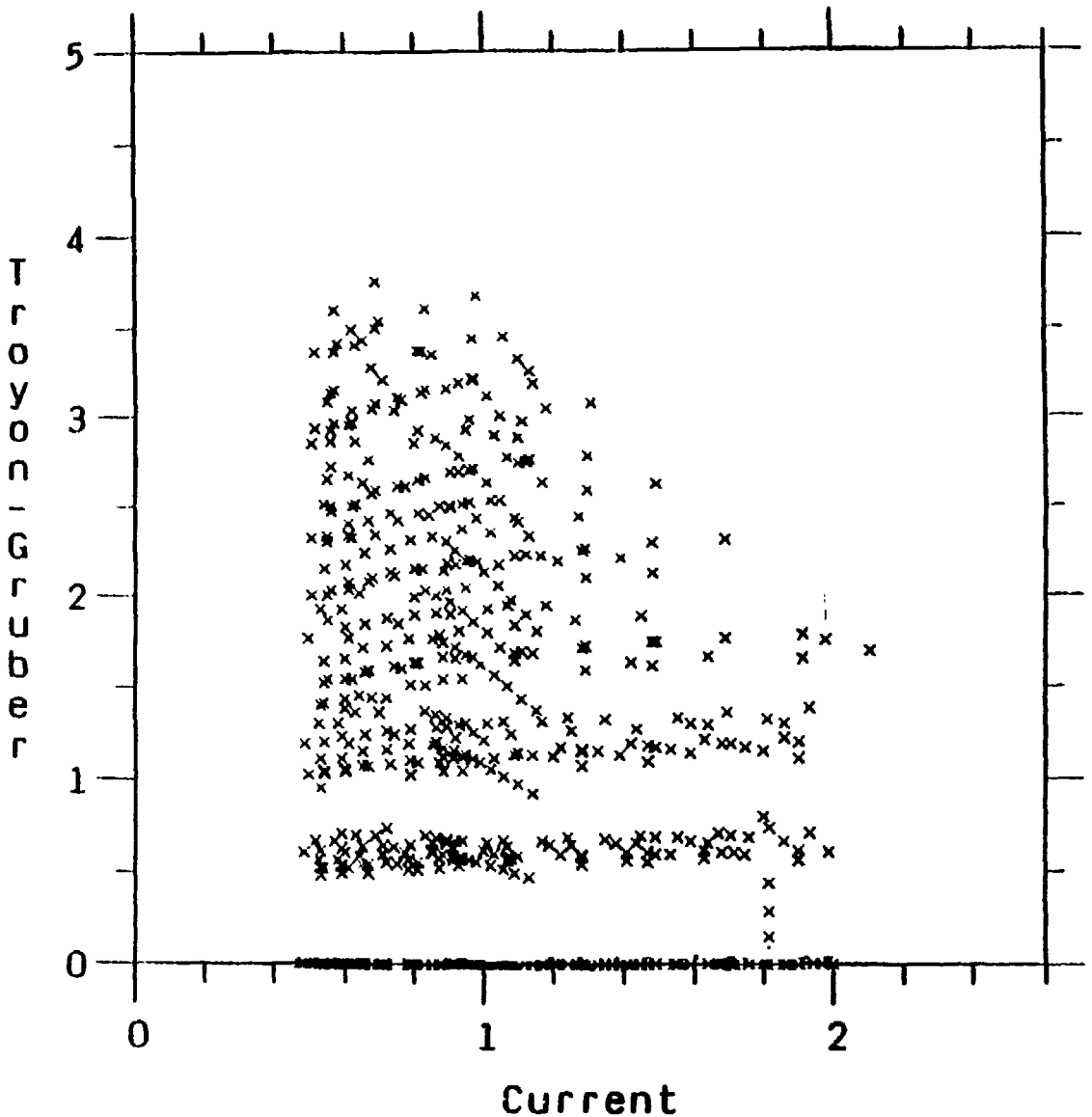

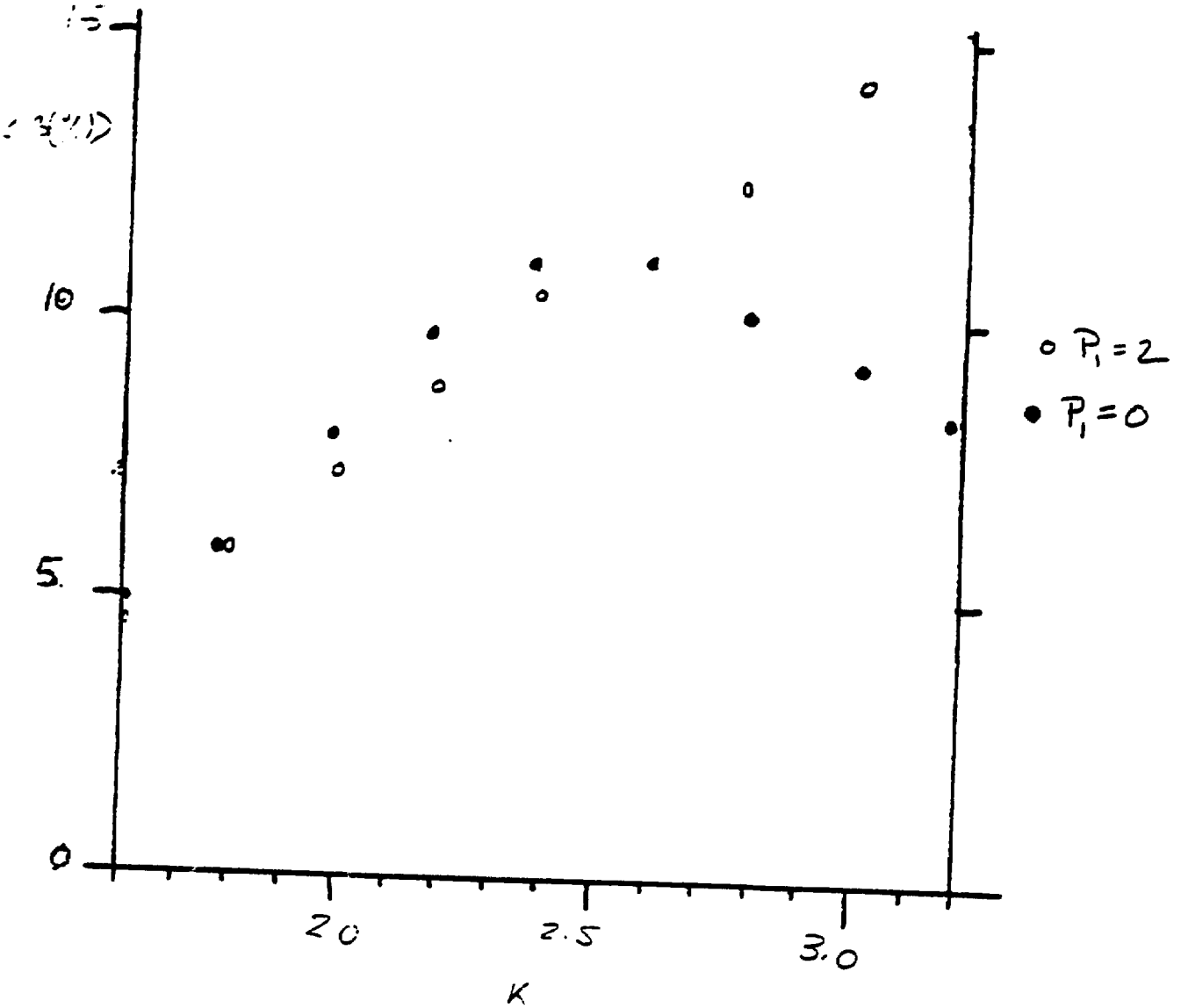
15
10
5.
0
2.0
2.5
3.0
K
○ $P_1 = 2$
● $P_1 = 0$

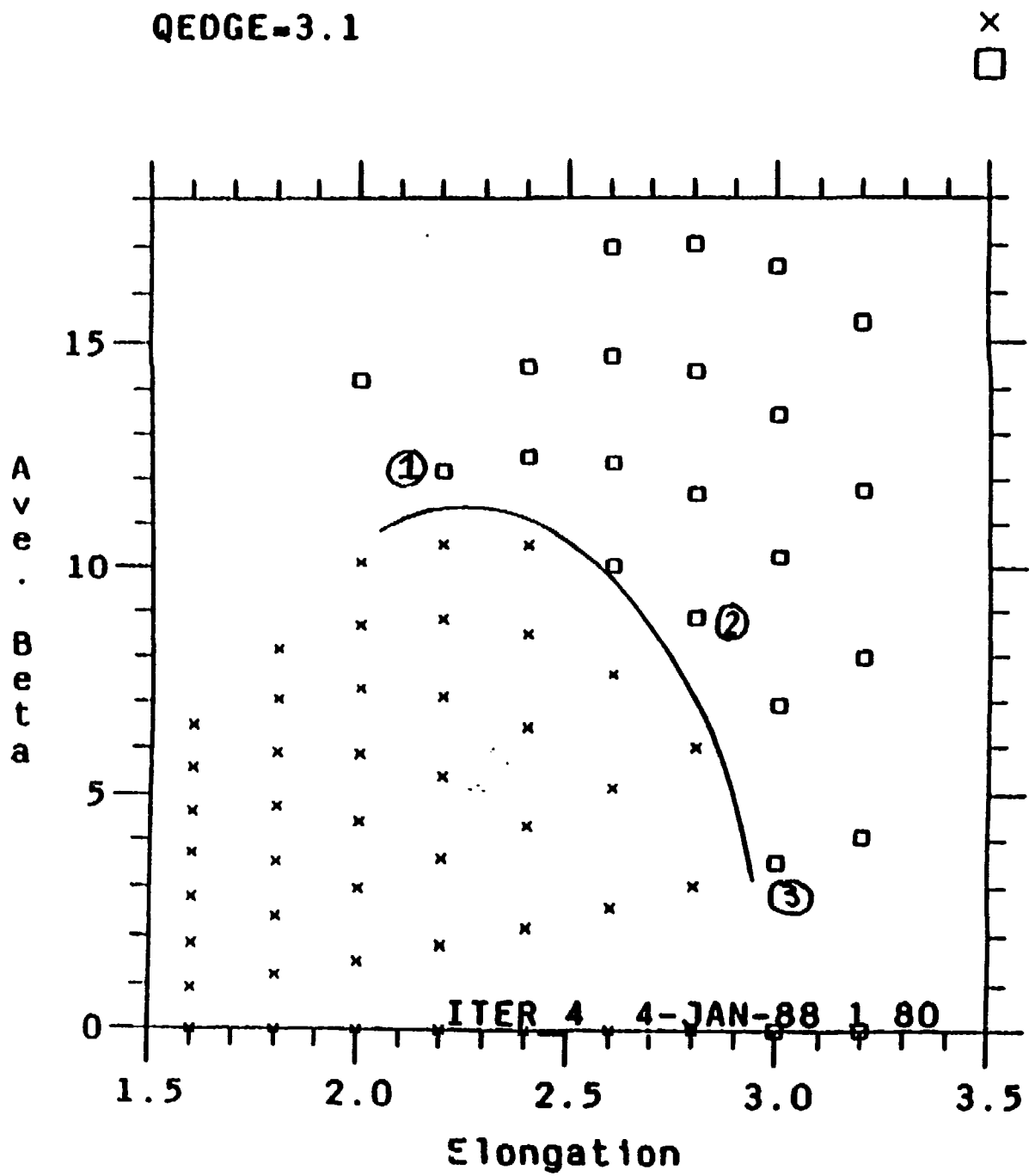
QEDGE=3.1
× PESST=1
□ PESST=0
Ave. Beta
15
10
5
0
1.5
2.0
2.5
3.0
3.5
Elongation
①
②
③
ITER 4 4-JAN-88 1 80

(β^max vs κ
n = 1, ballooning,
No fit

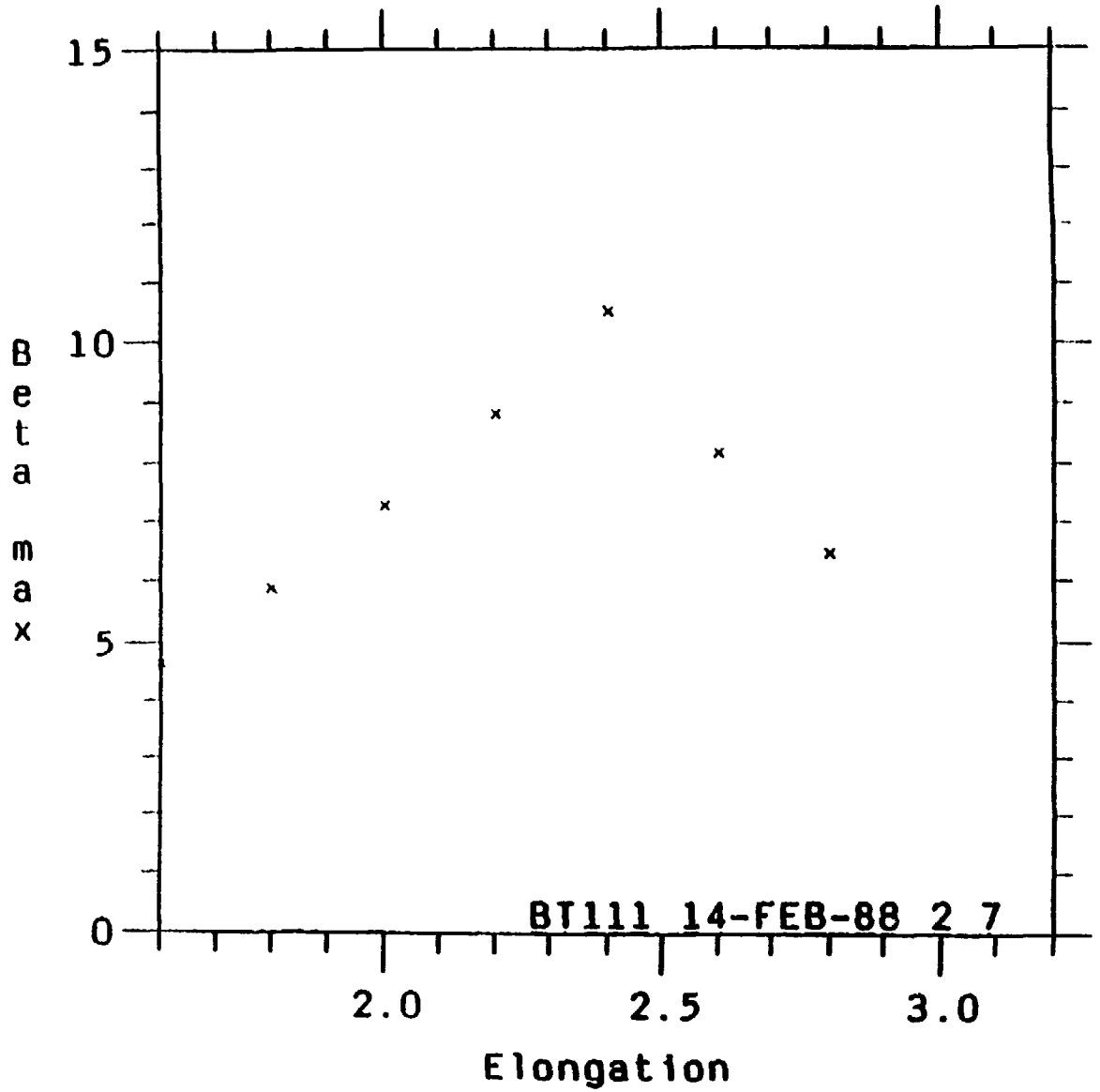

(8c)

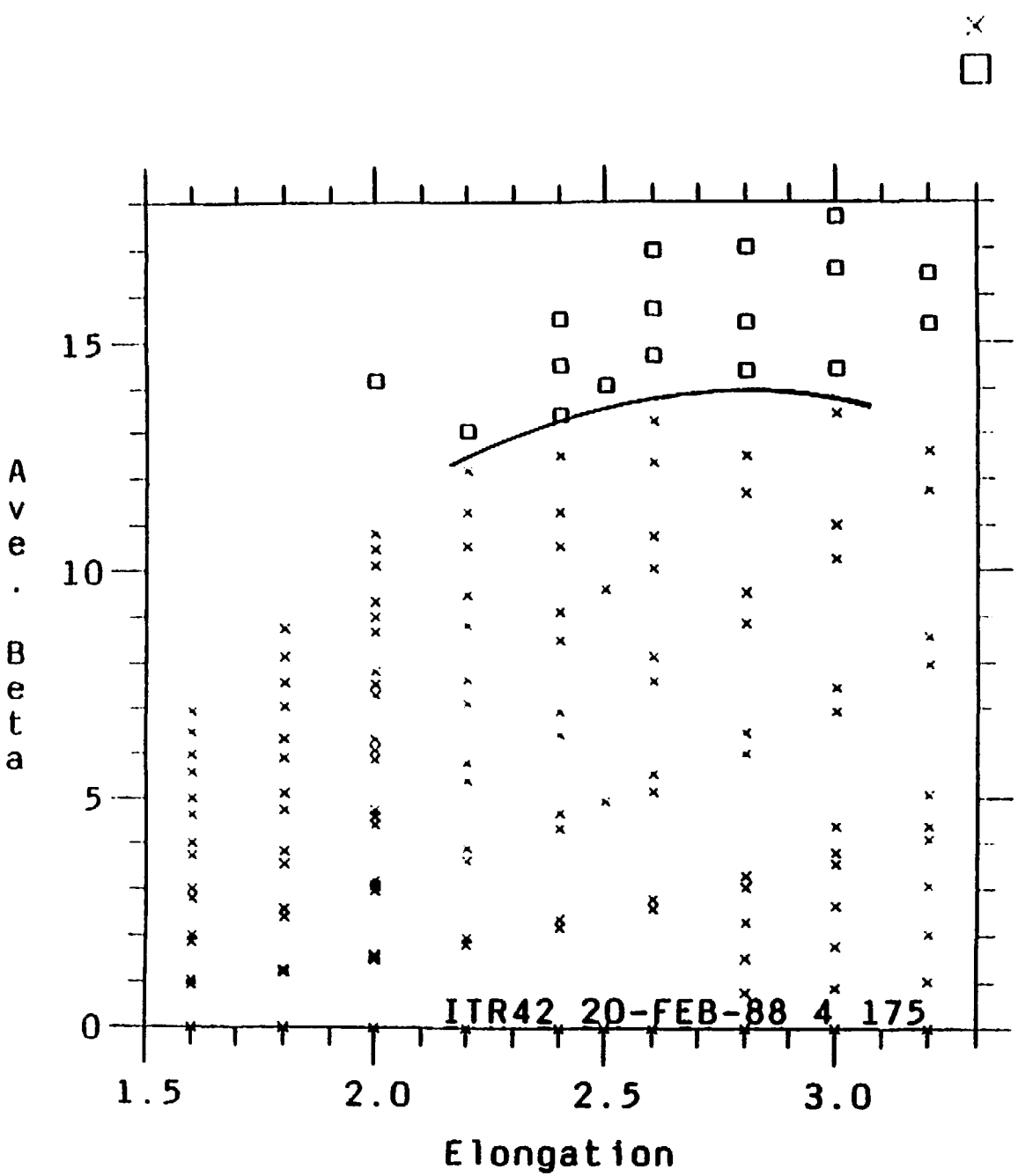
× PESST=1
□ PESST=0
Ave. Beta
15
10
5
0
1.5
2.0
2.5
3.0
Elongation
ITR42 20-FEB-88 4 175

ol.

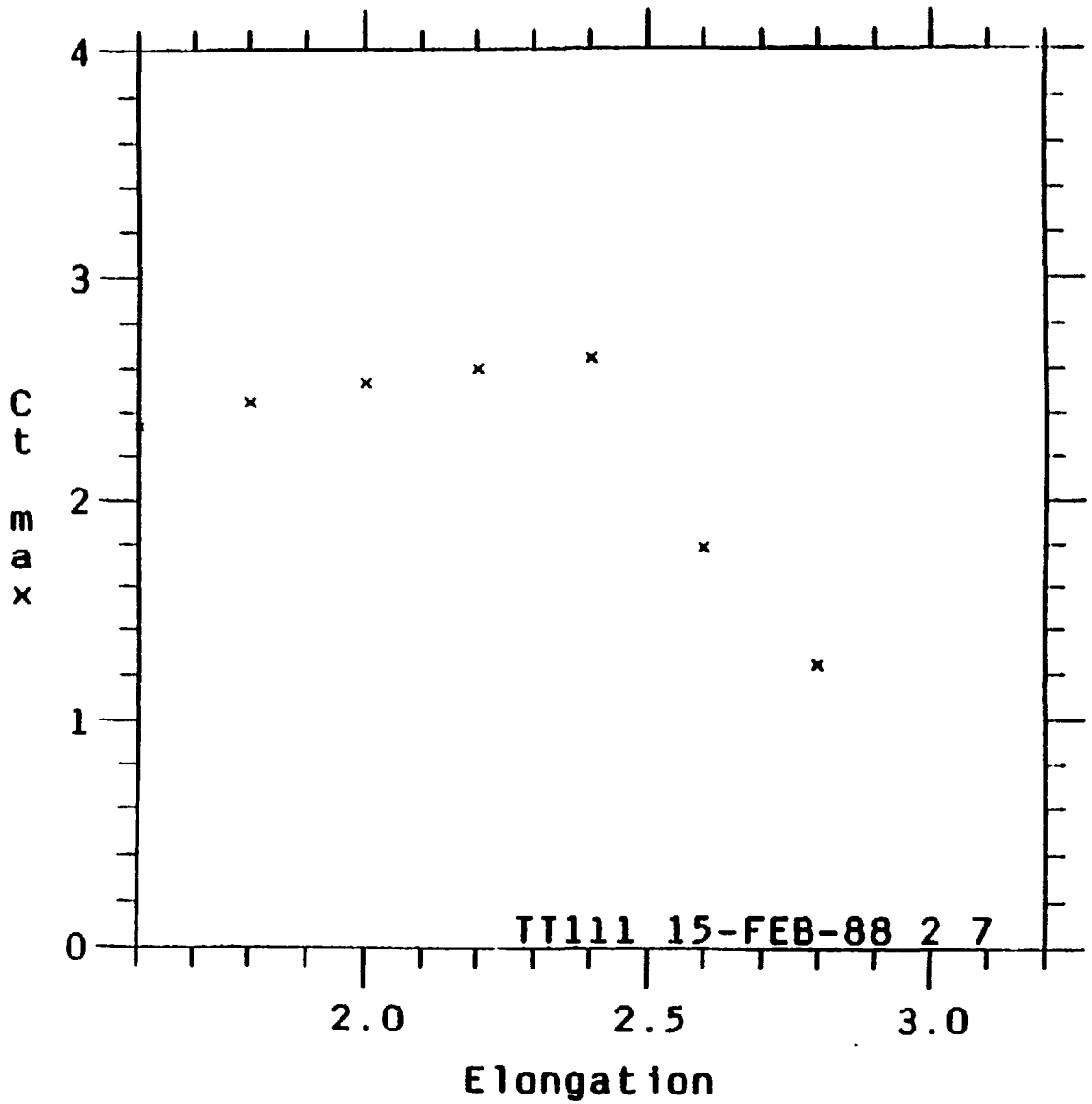

(8e)

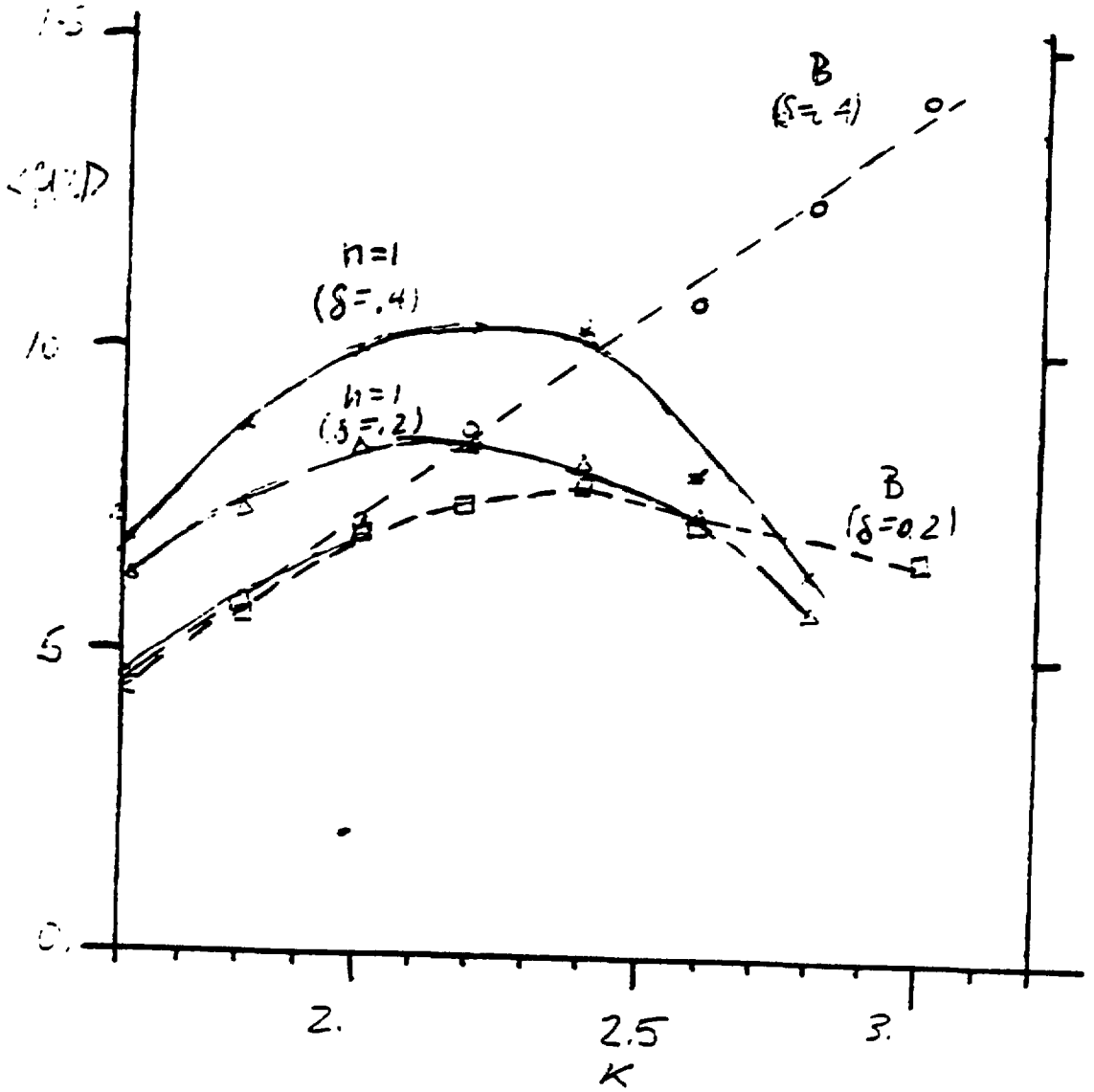

9a

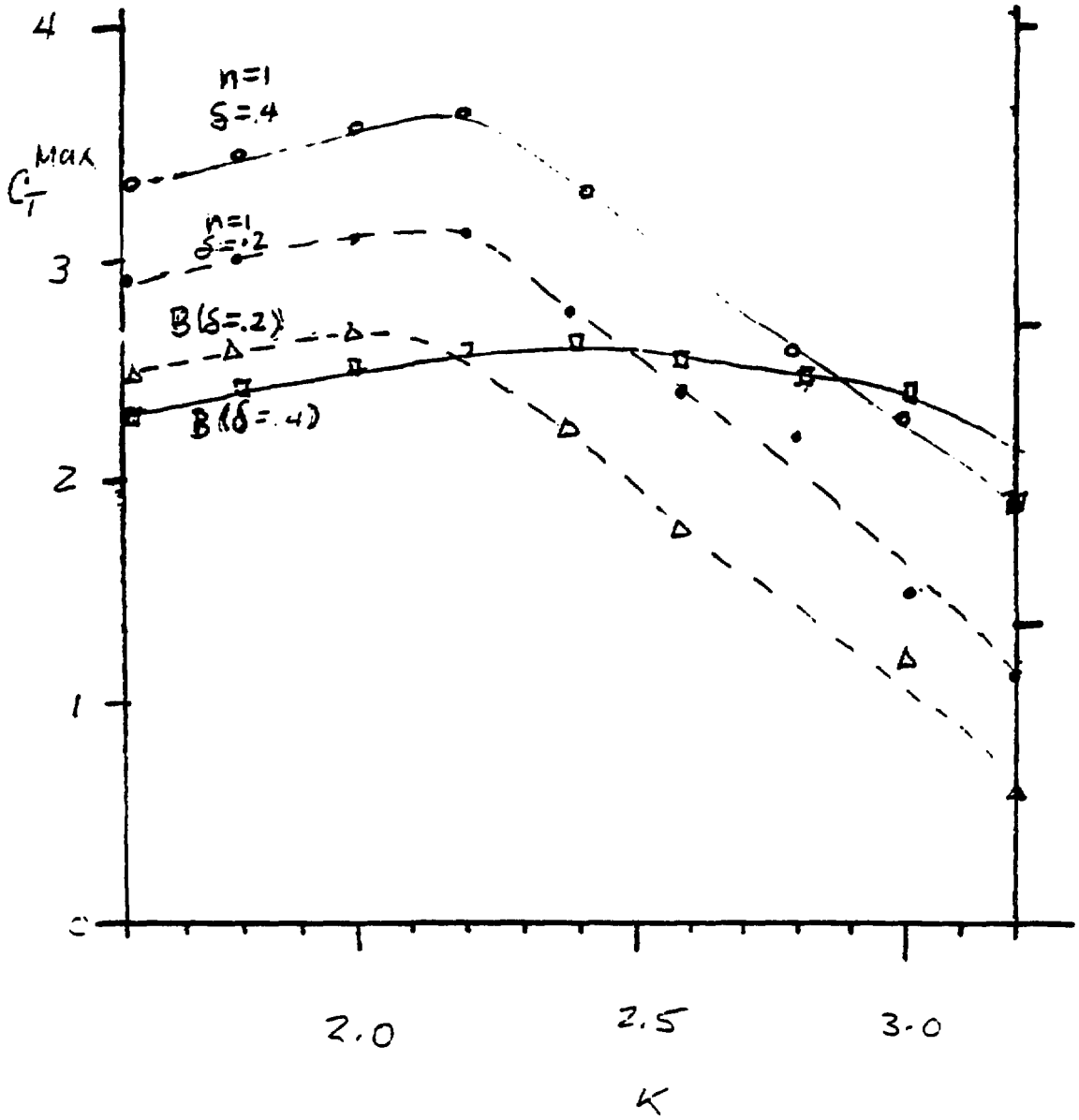
4
3
2
1
0
C_T^{MAX}
n=1
δ=.4
n=1
δ=.2
B(δ=.2)
B(δ=.4)
2.0
2.5
3.0
K

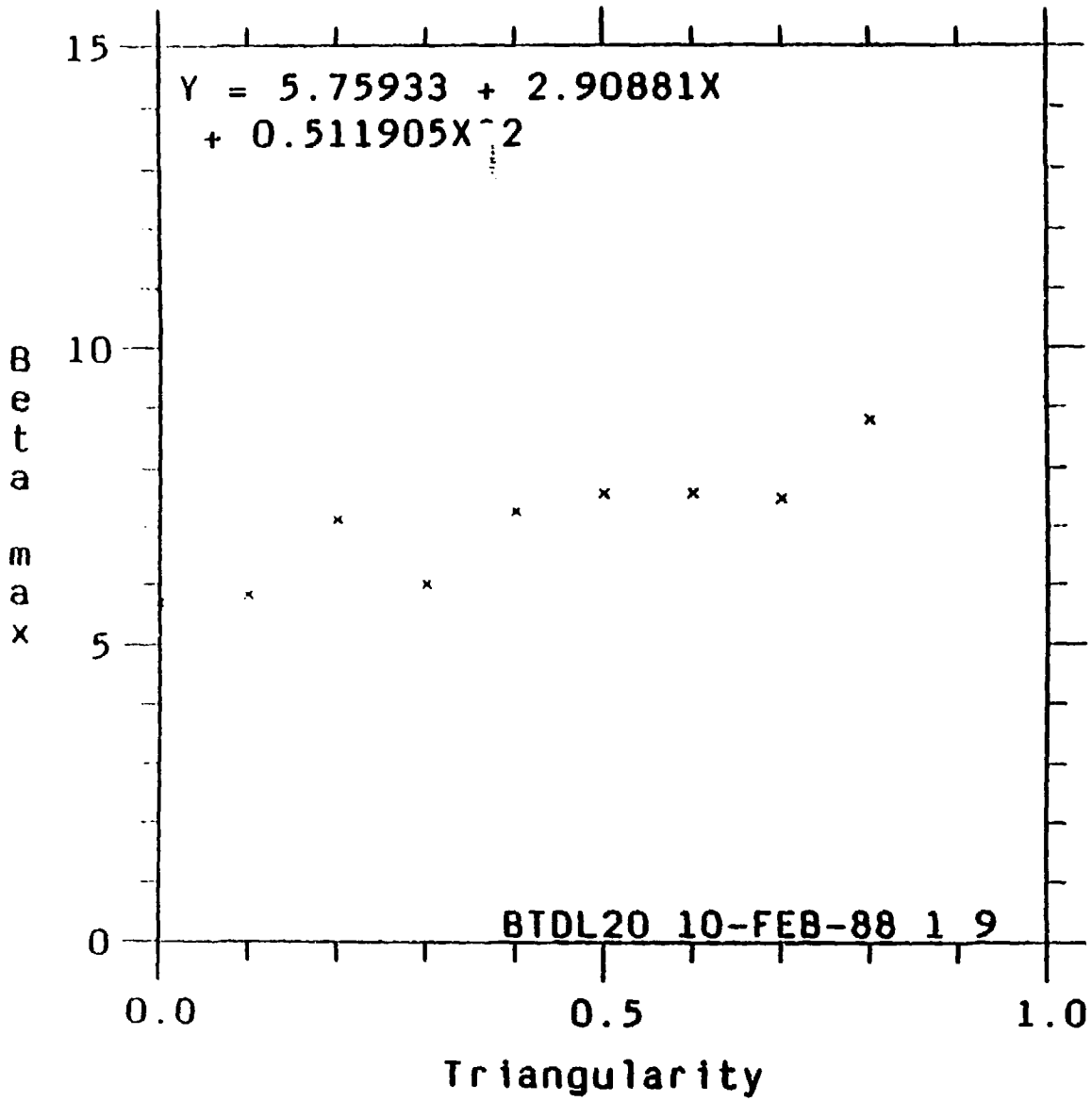
Y = 5.75933 + 2.90881X
+ 0.511905X^2
BTDL20 10-FEB-88 1 9
Beta max
Triangularity
15
10
5
0
0.0
0.5
1.0

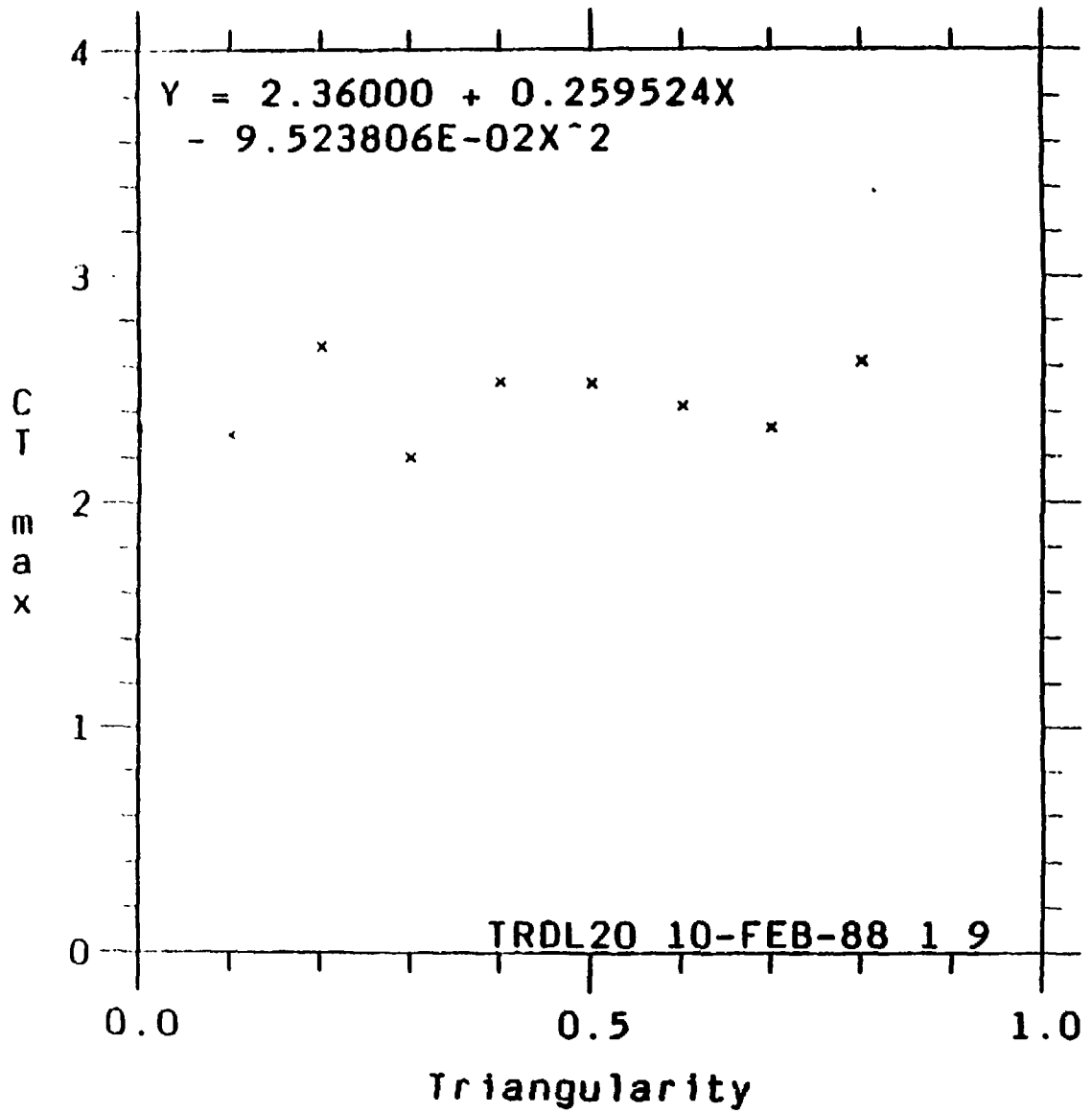
Y = 2.36000 + 0.259524X
- 9.523806E-02X^2
TRDL20 10-FEB-88 1 9
CT max
Triangularity
0
1
2
3
4
0.0
0.5
1.0

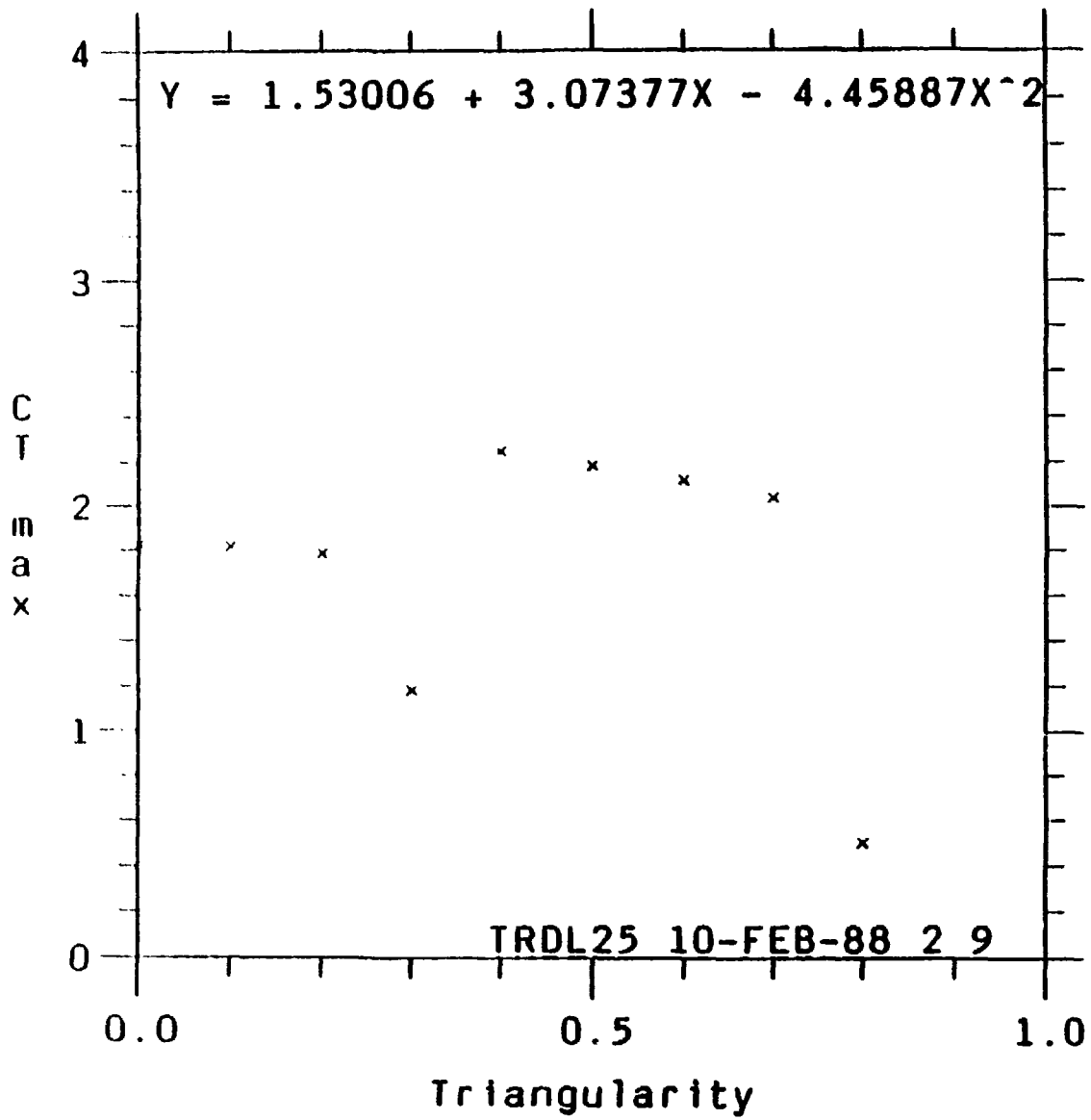
Y = 1.53006 + 3.07377X - 4.45887X^2
TRDL25 10-FEB-88 2 9
CT max
Triangularity
0
1
2
3
4
0.0
0.5
1.0

(11a)

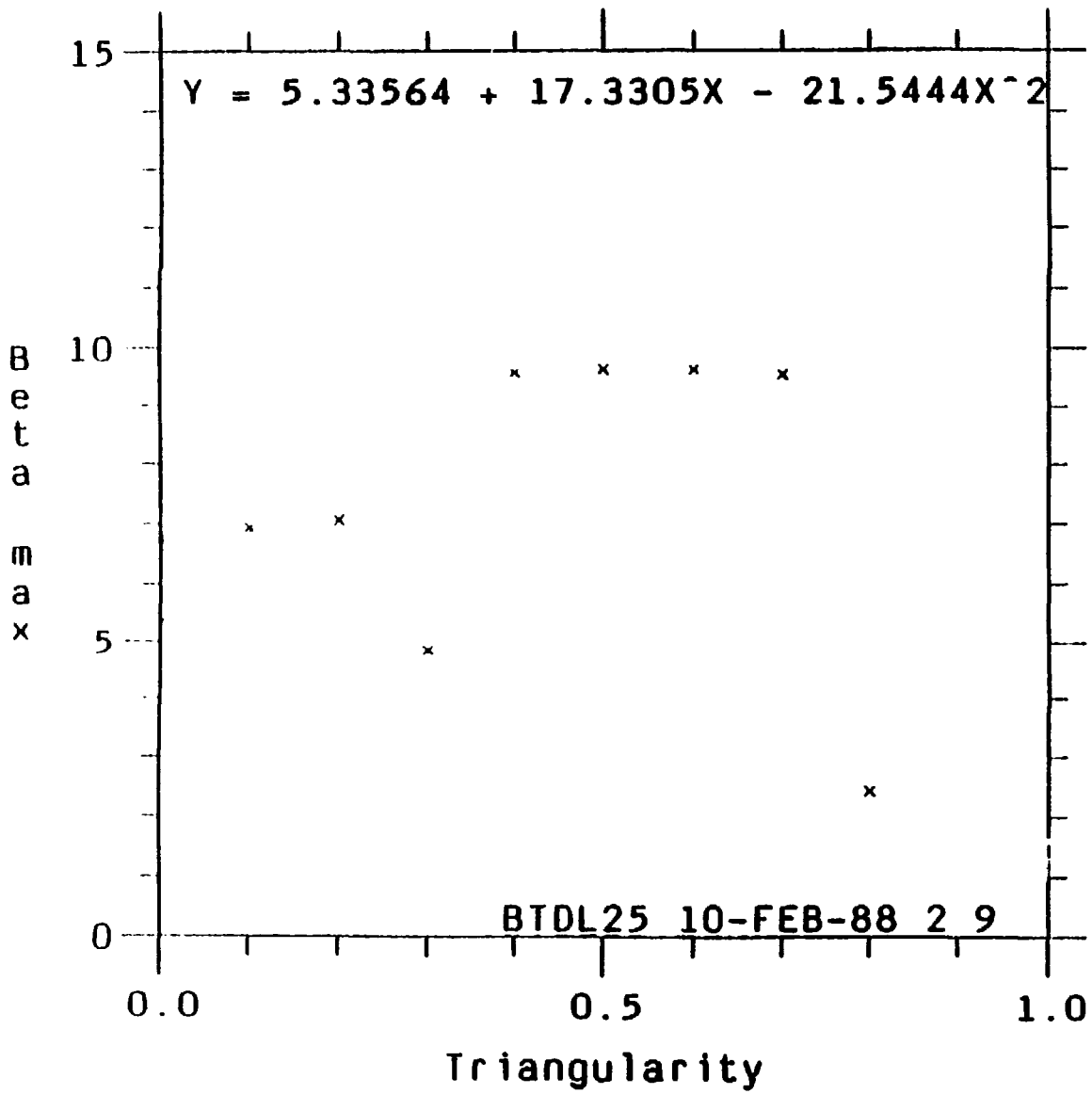
Y = 5.33564 + 17.3305X - 21.5444X^2
BTDL25 10-FEB-88 2 9
Beta max
Triangularity
15
10
5
0
0.0
0.5
1.0

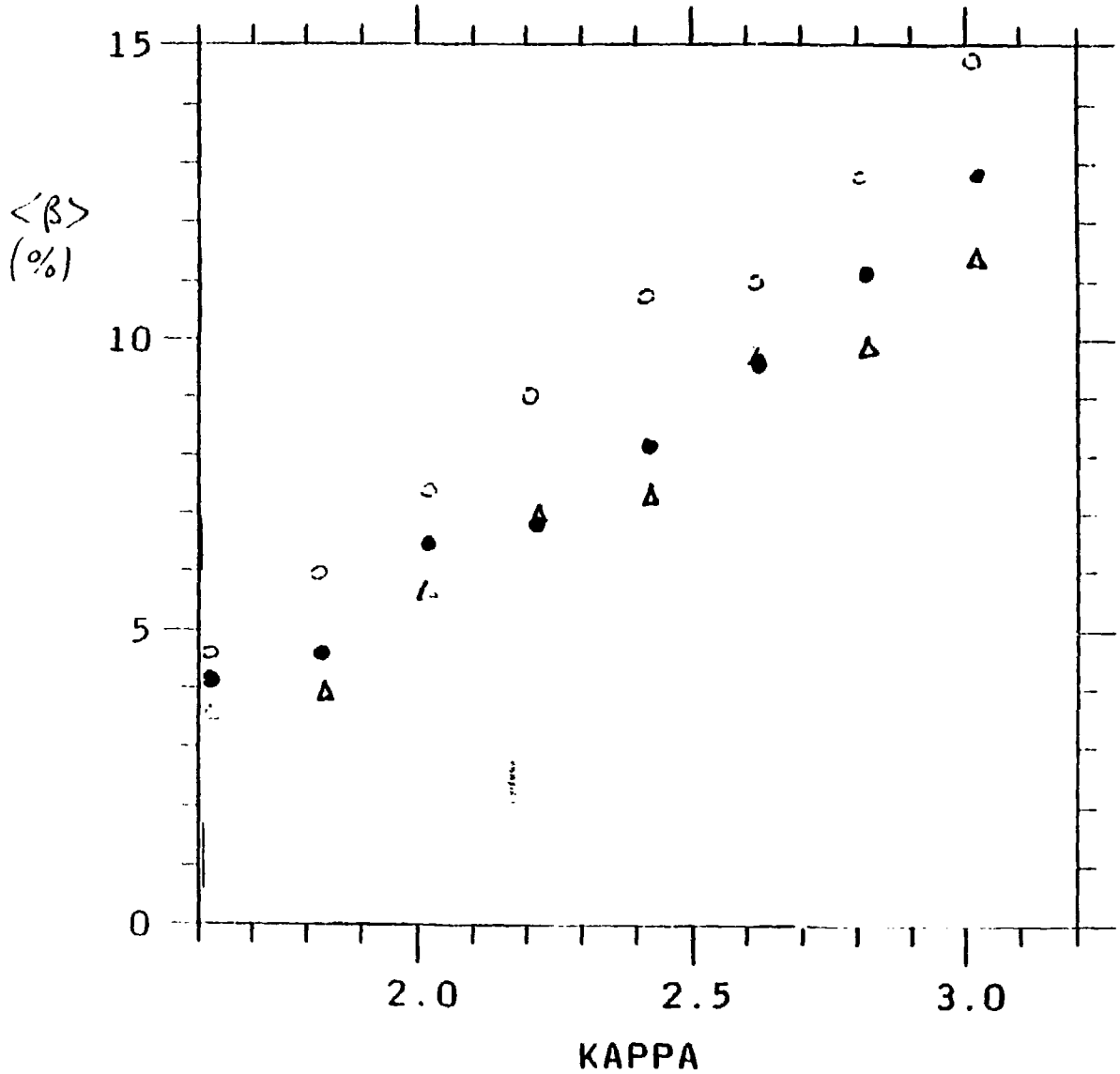
15
10
5
0
<β>
(%)
2.0
2.5
3.0
KAPPA

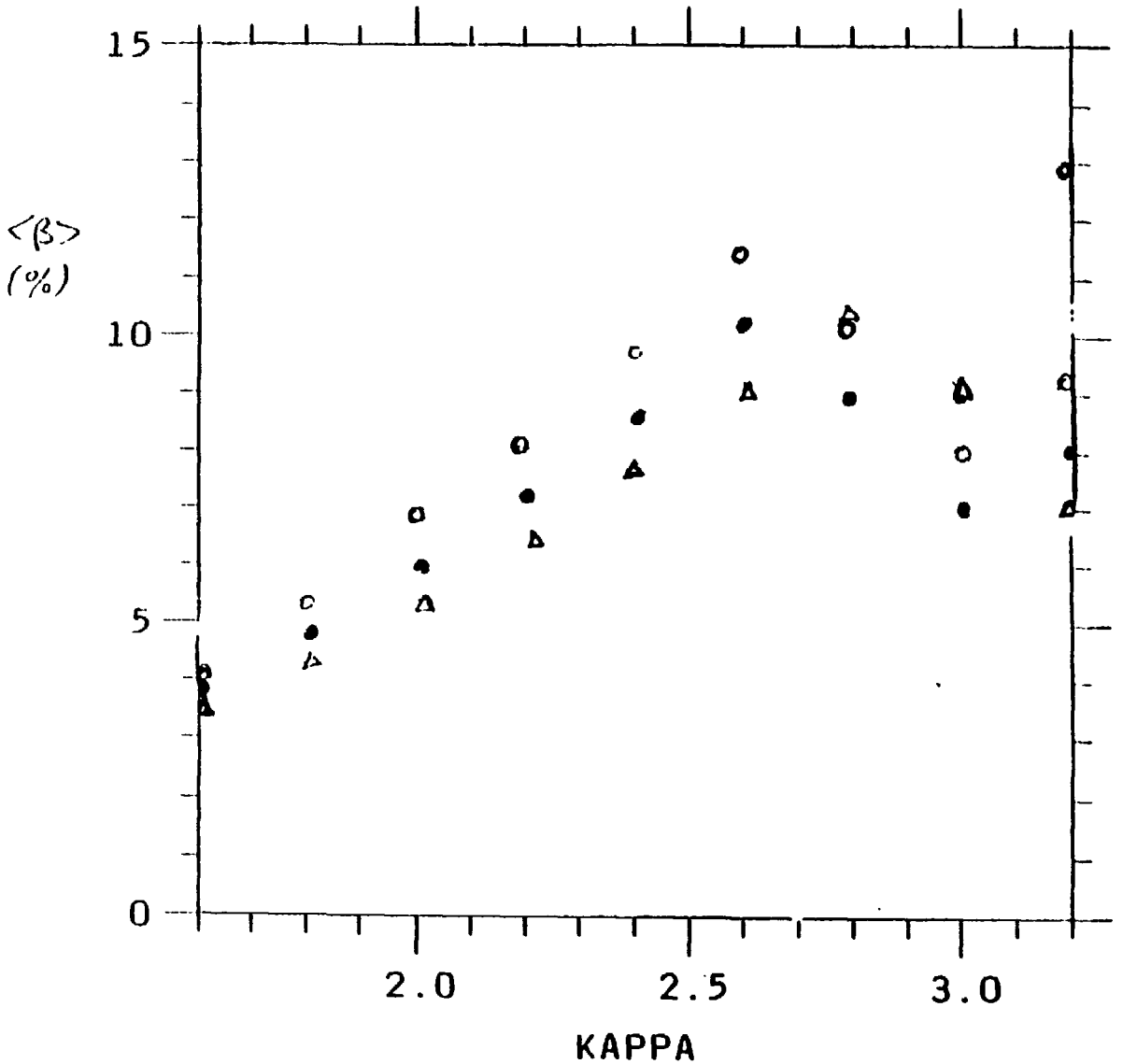
15
10
5
0
<β>
(%)
2.0
2.5
3.0
KAPPA

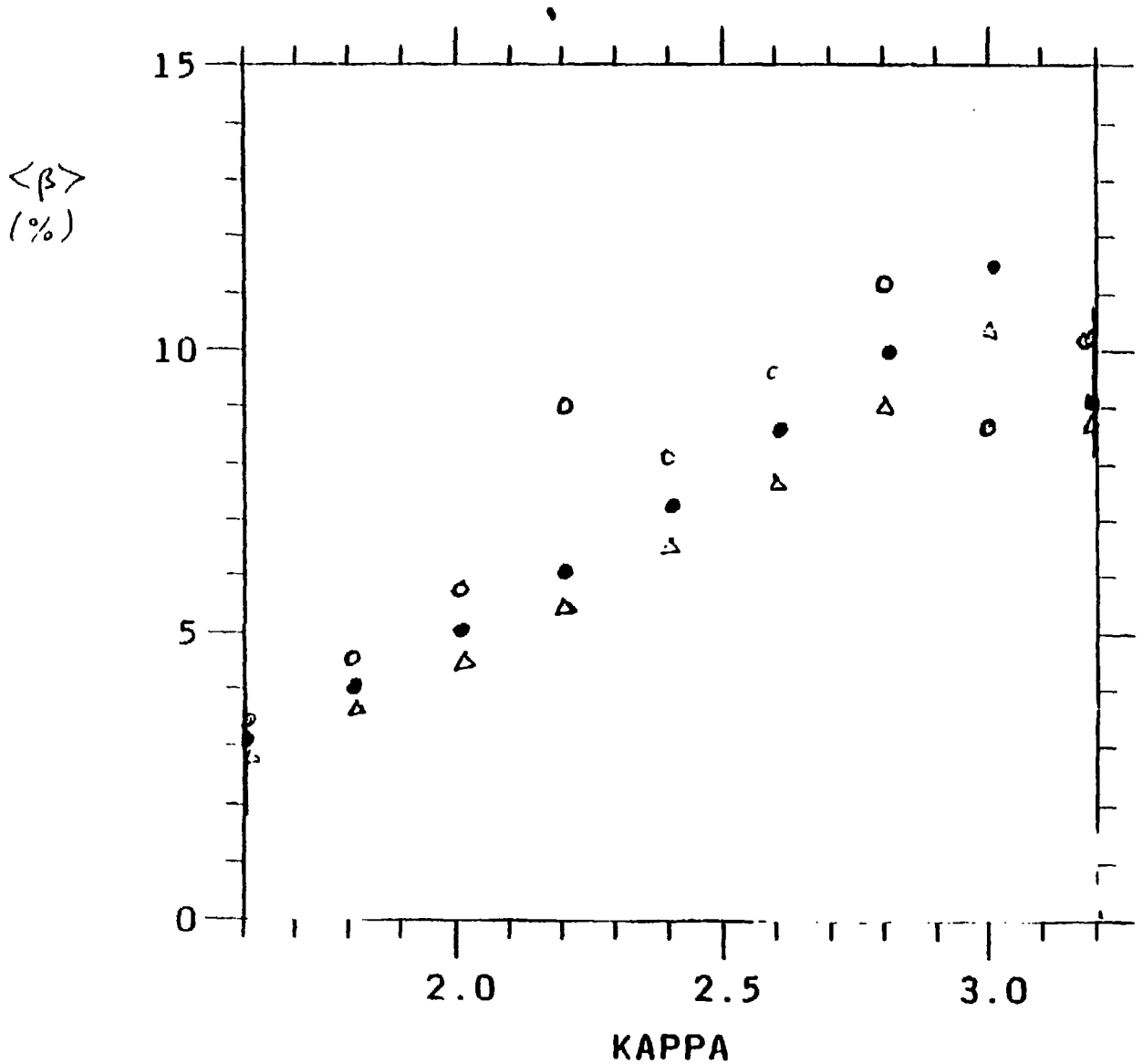
15
10
5
0
<β>
(%)
2.0
2.5
3.0
KAPPA

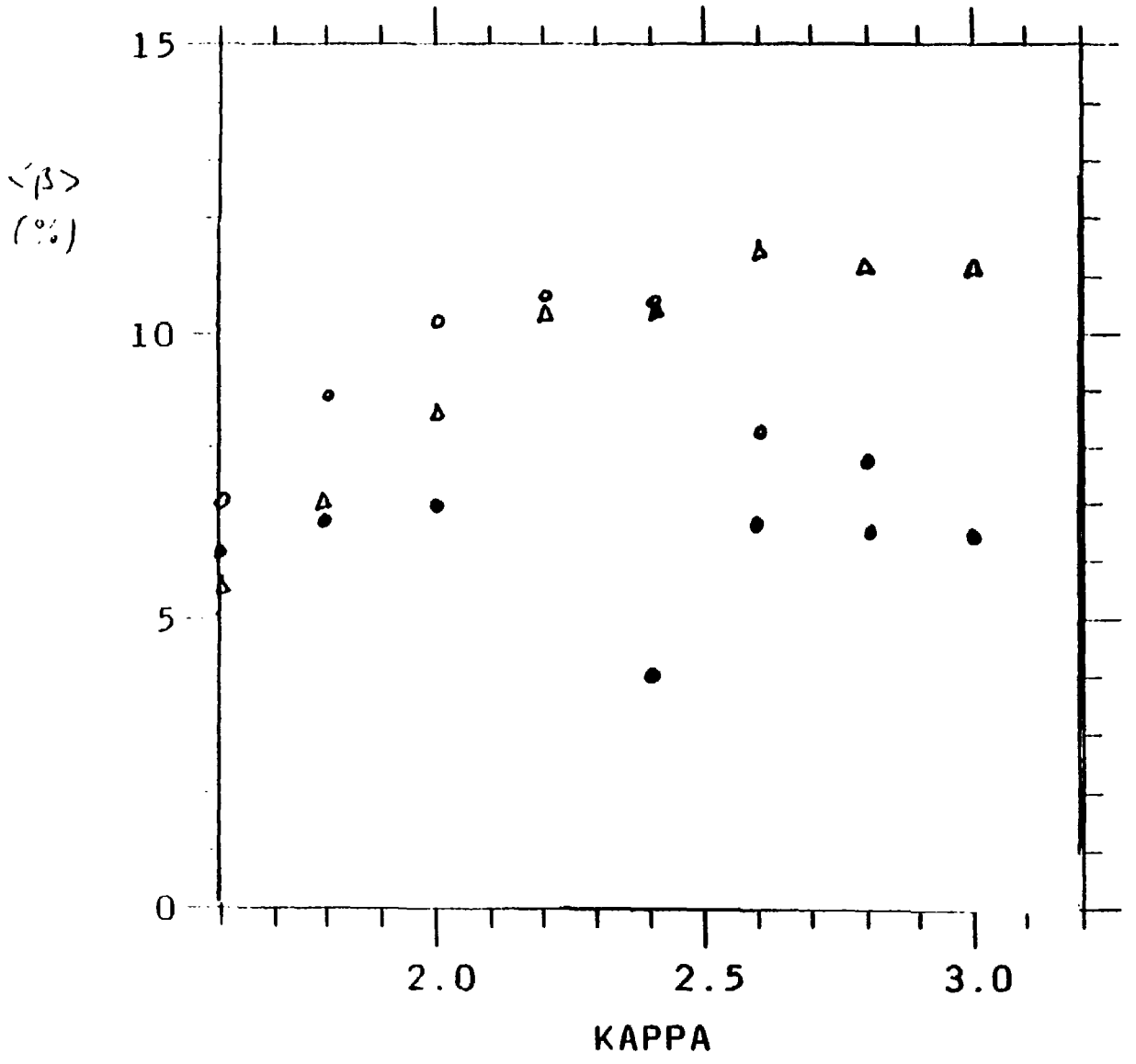

13a

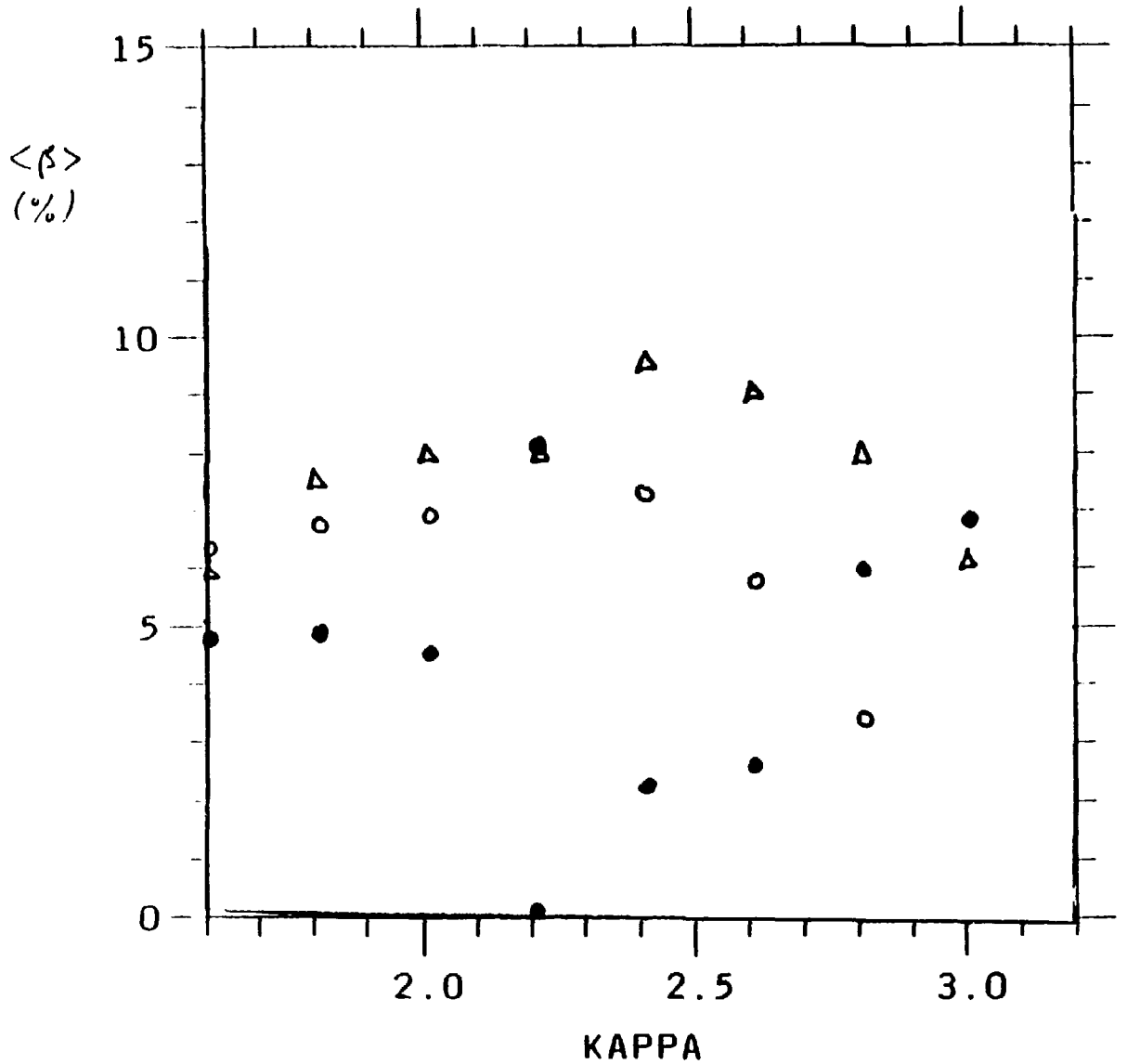
15
10
5
0
<β>
(%)
2.0
2.5
3.0
KAPPA

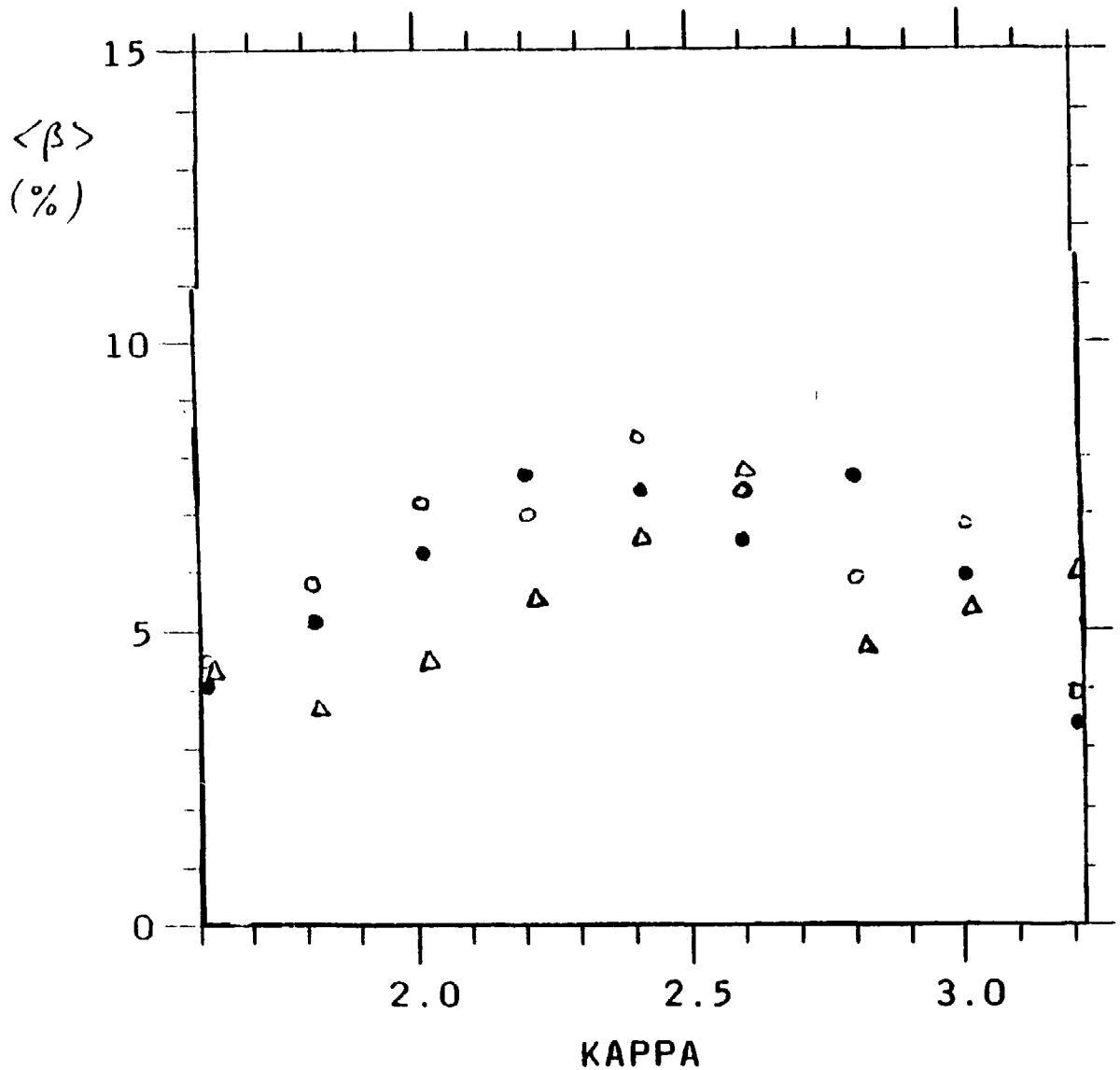

14a

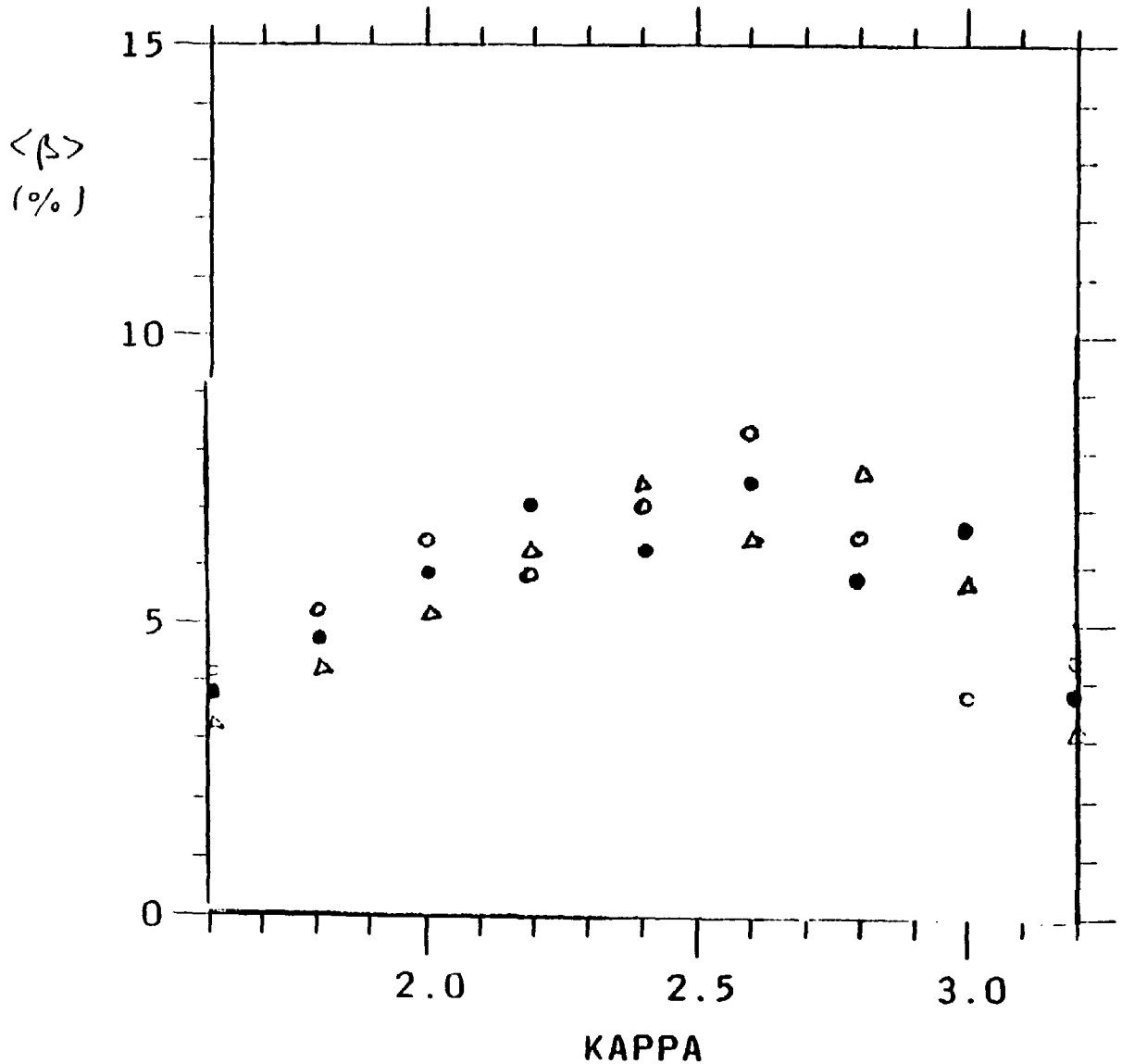
15
10
5
0
<β>
(%)
2.0
2.5
3.0
KAPPA

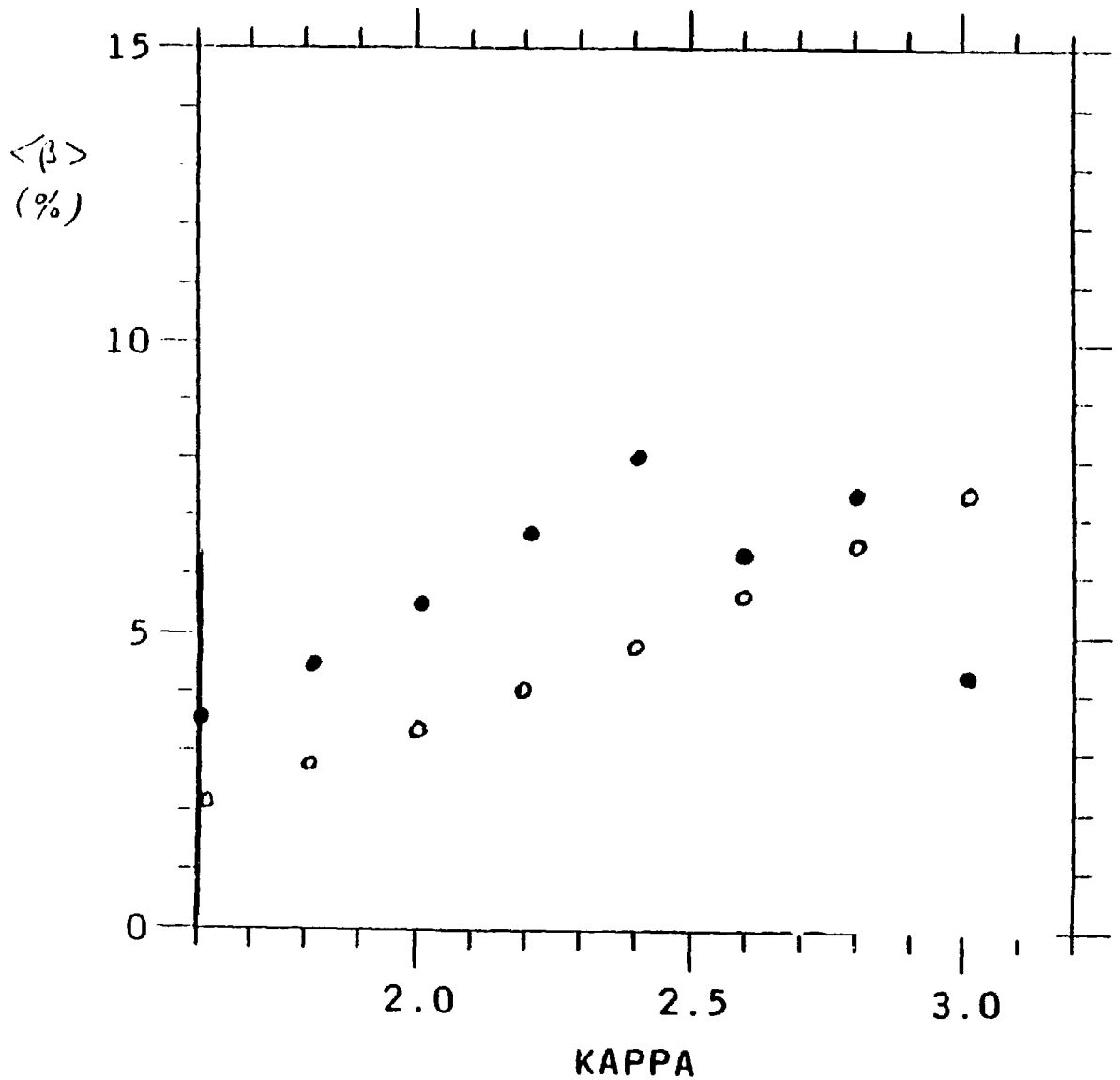

14c

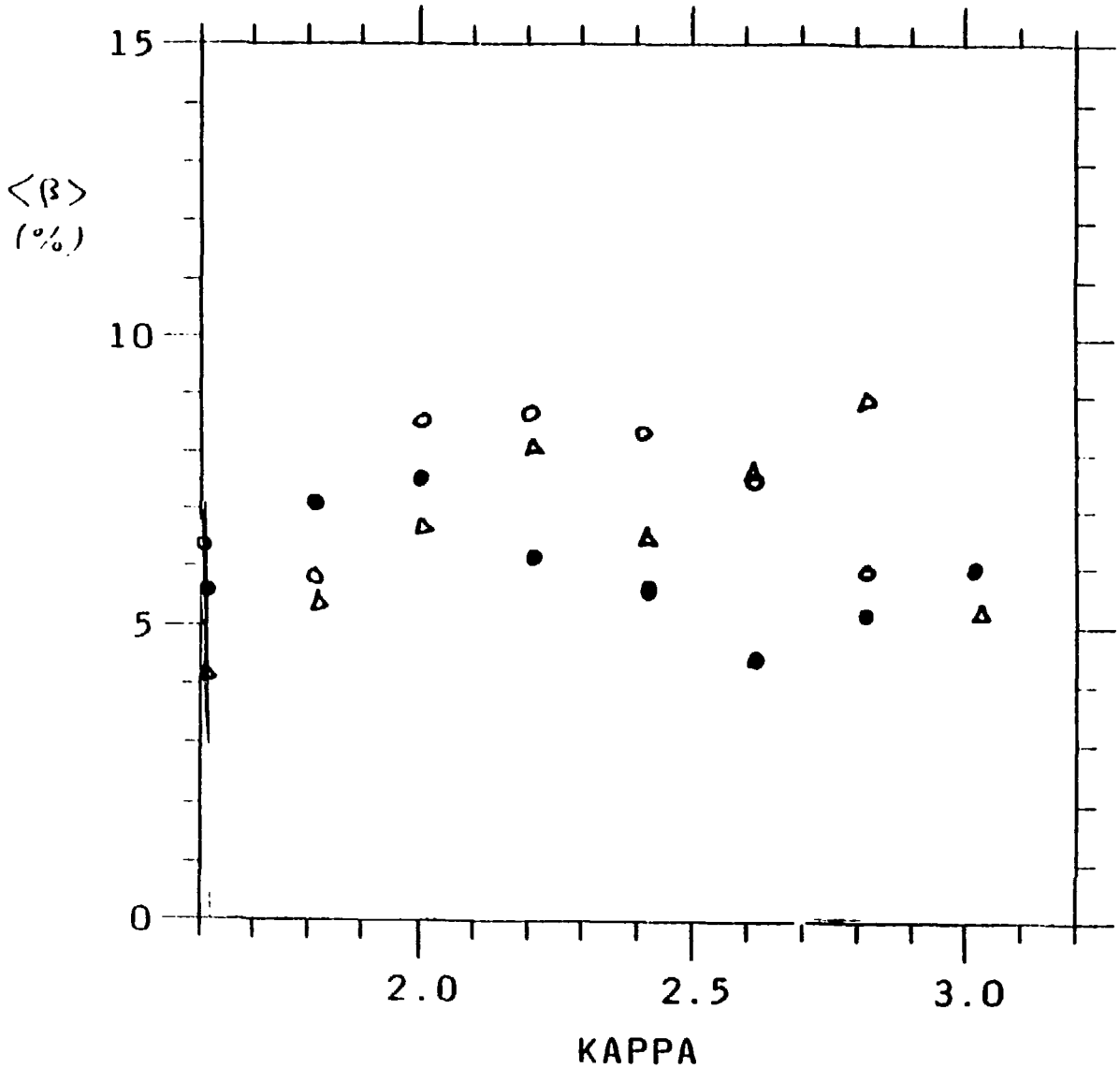
15
10
5
0
<β>
(%)
2.0
2.5
3.0
KAPPA

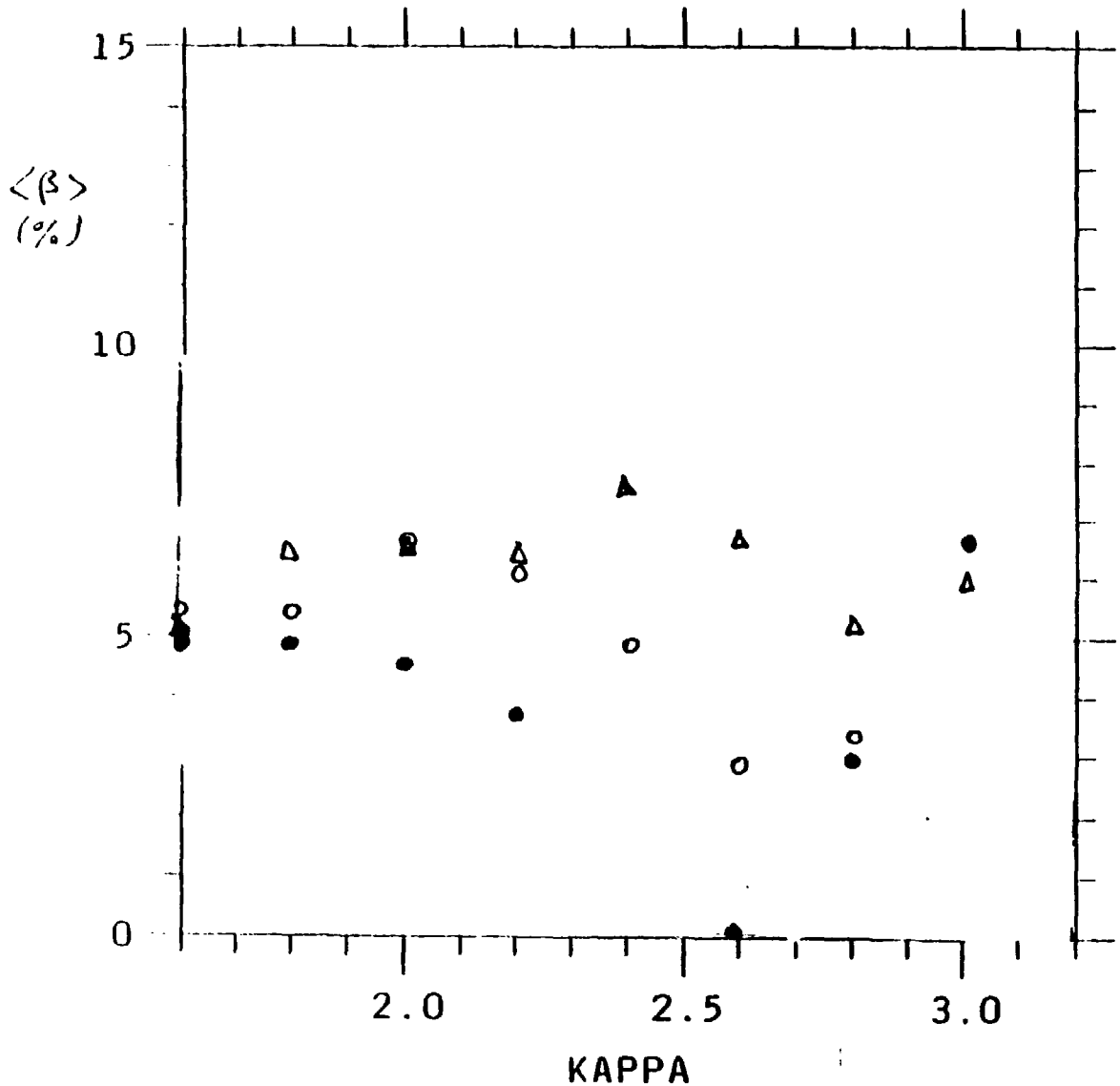
15
10
5
0
<β>
(%)
2.0
2.5
3.0
KAPPA

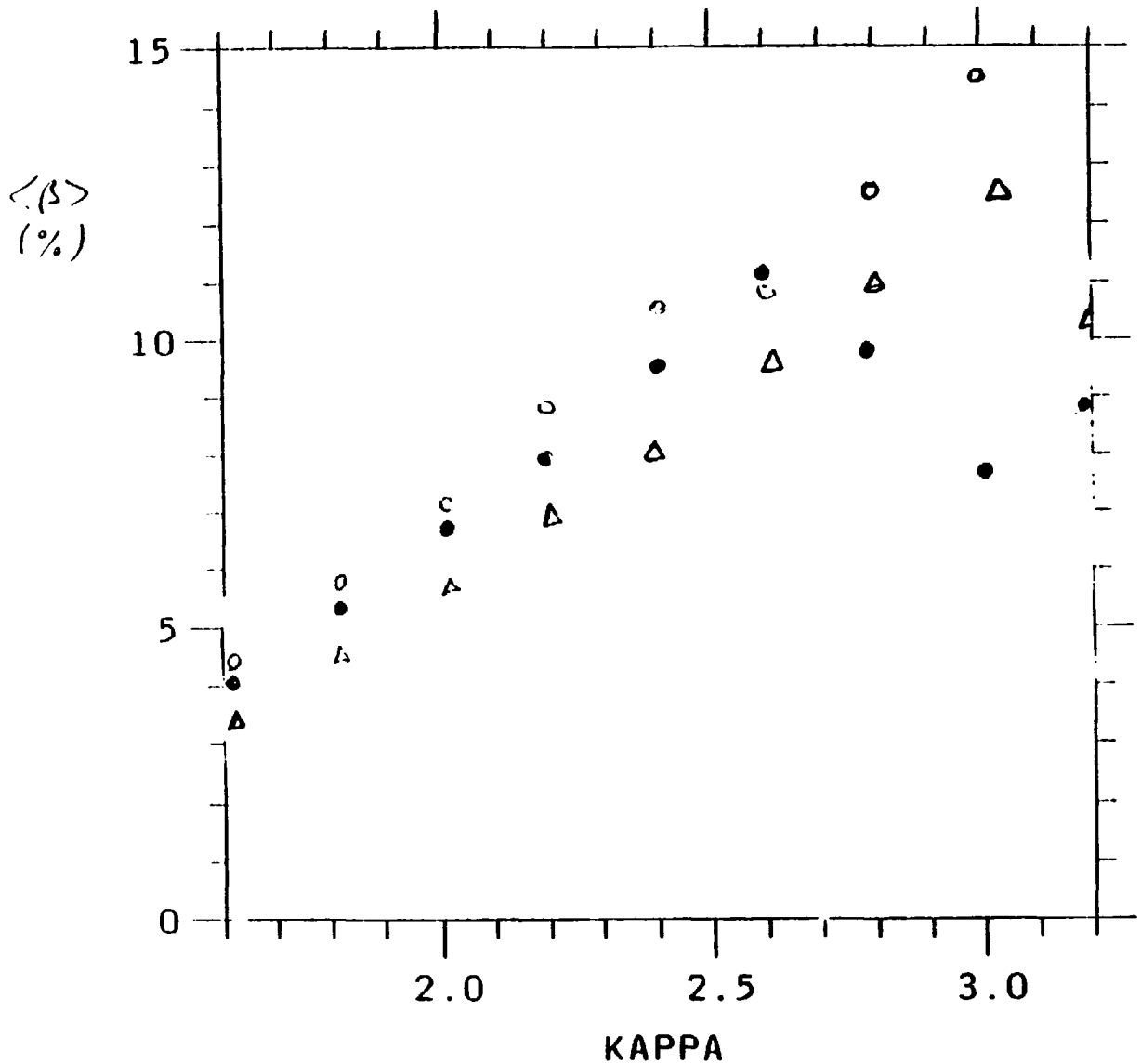

16a

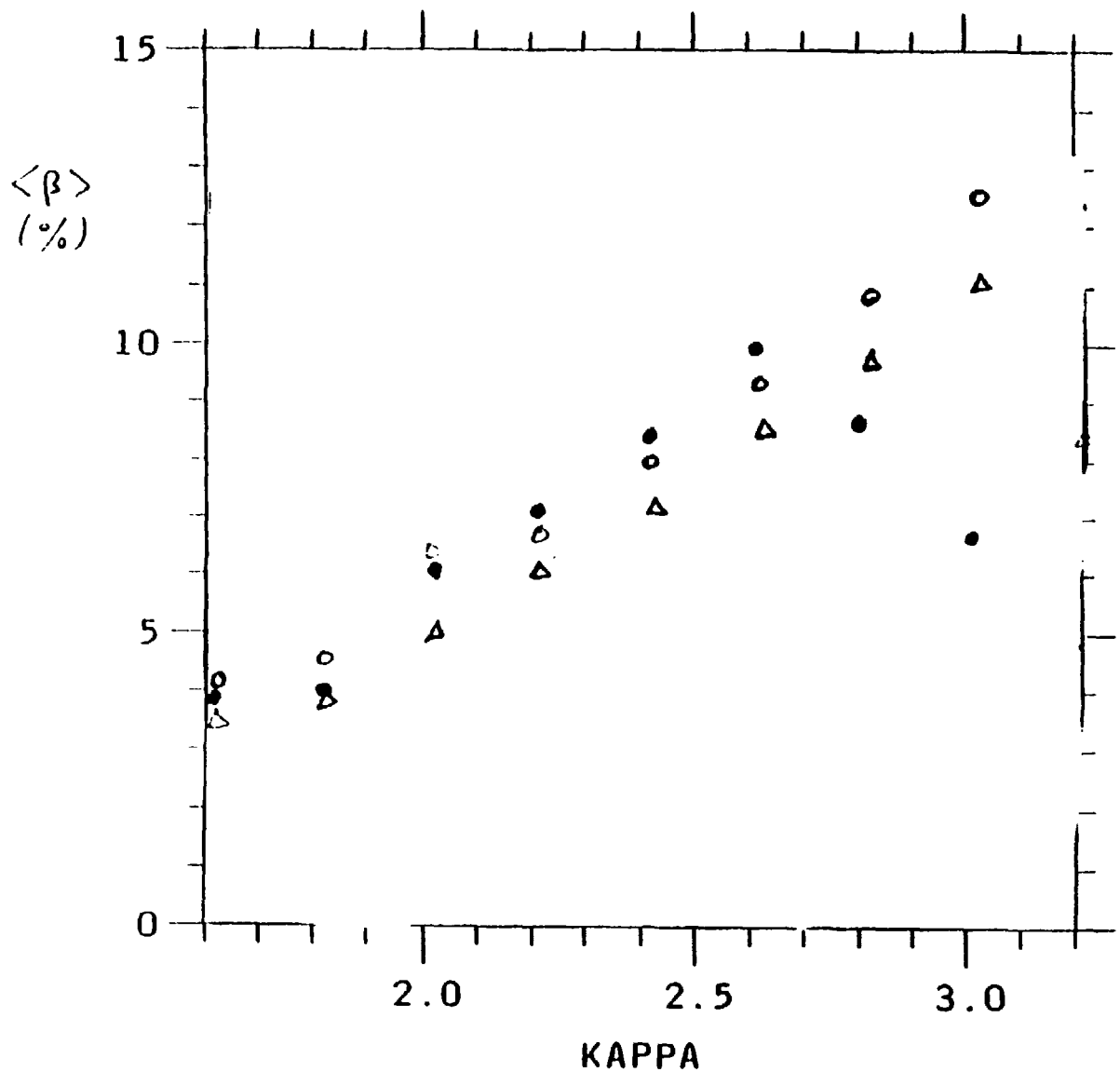
15
10
5
0
<β>
(%)
2.0
2.5
3.0
KAPPA

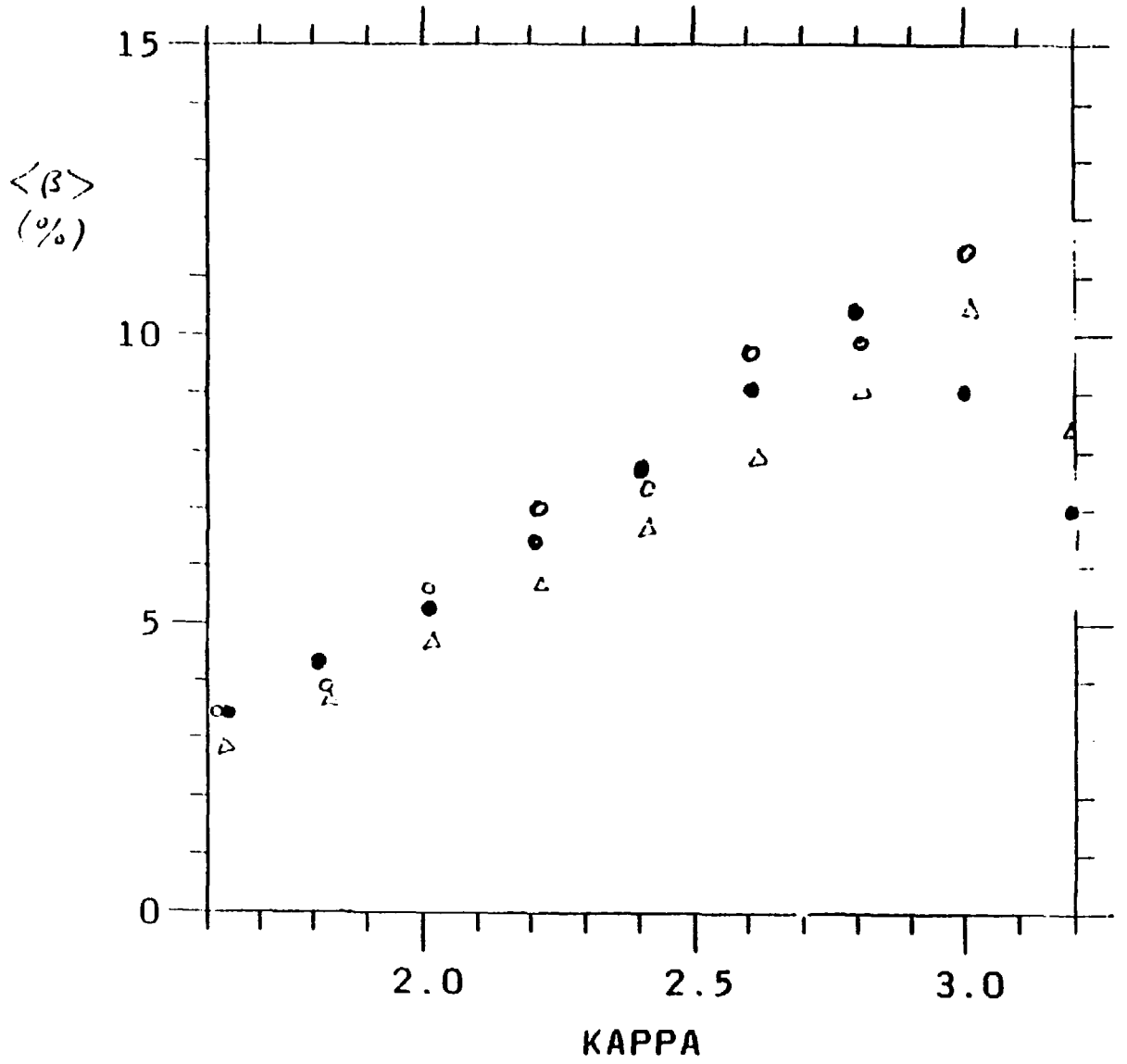

16c

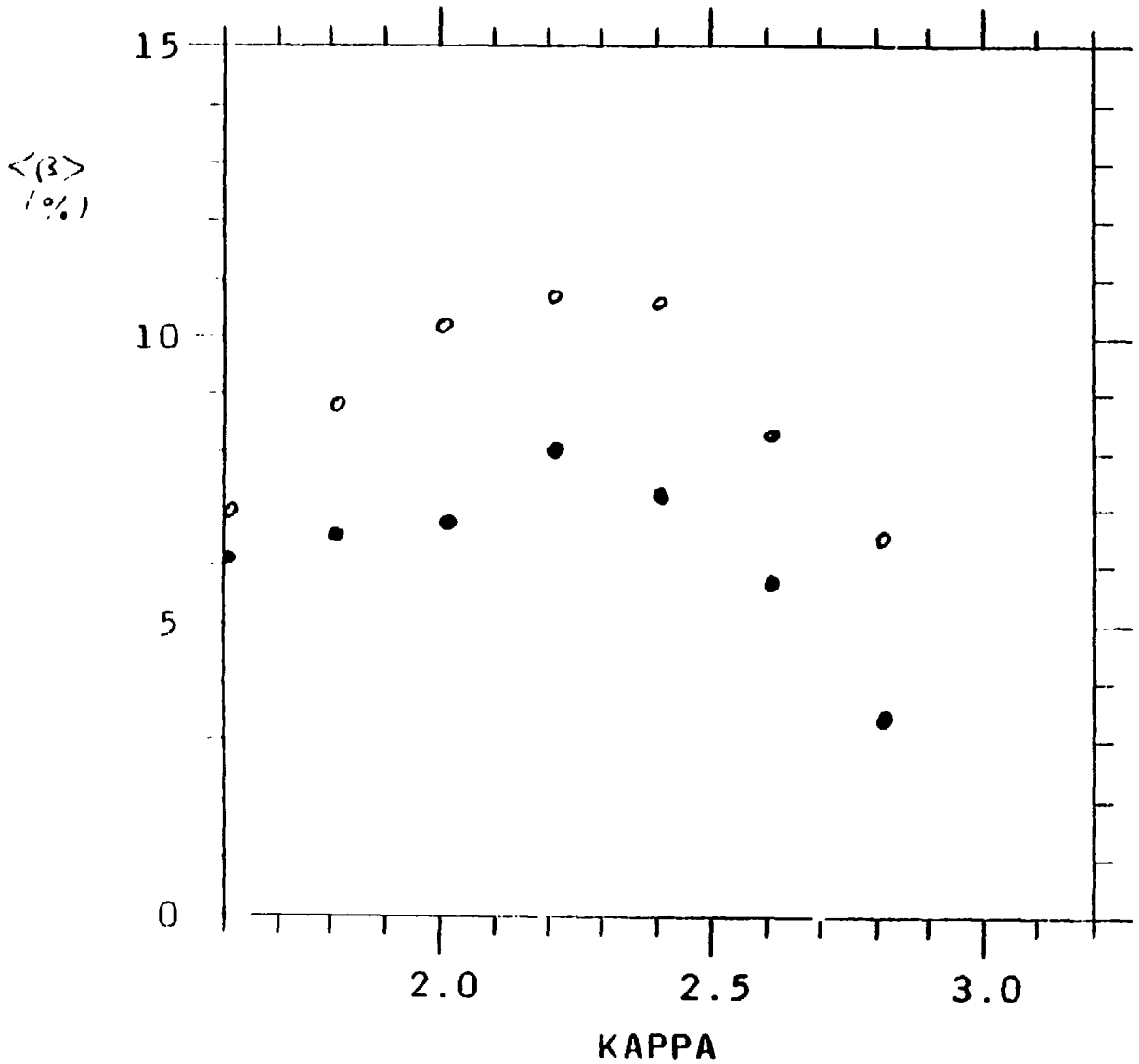

17a

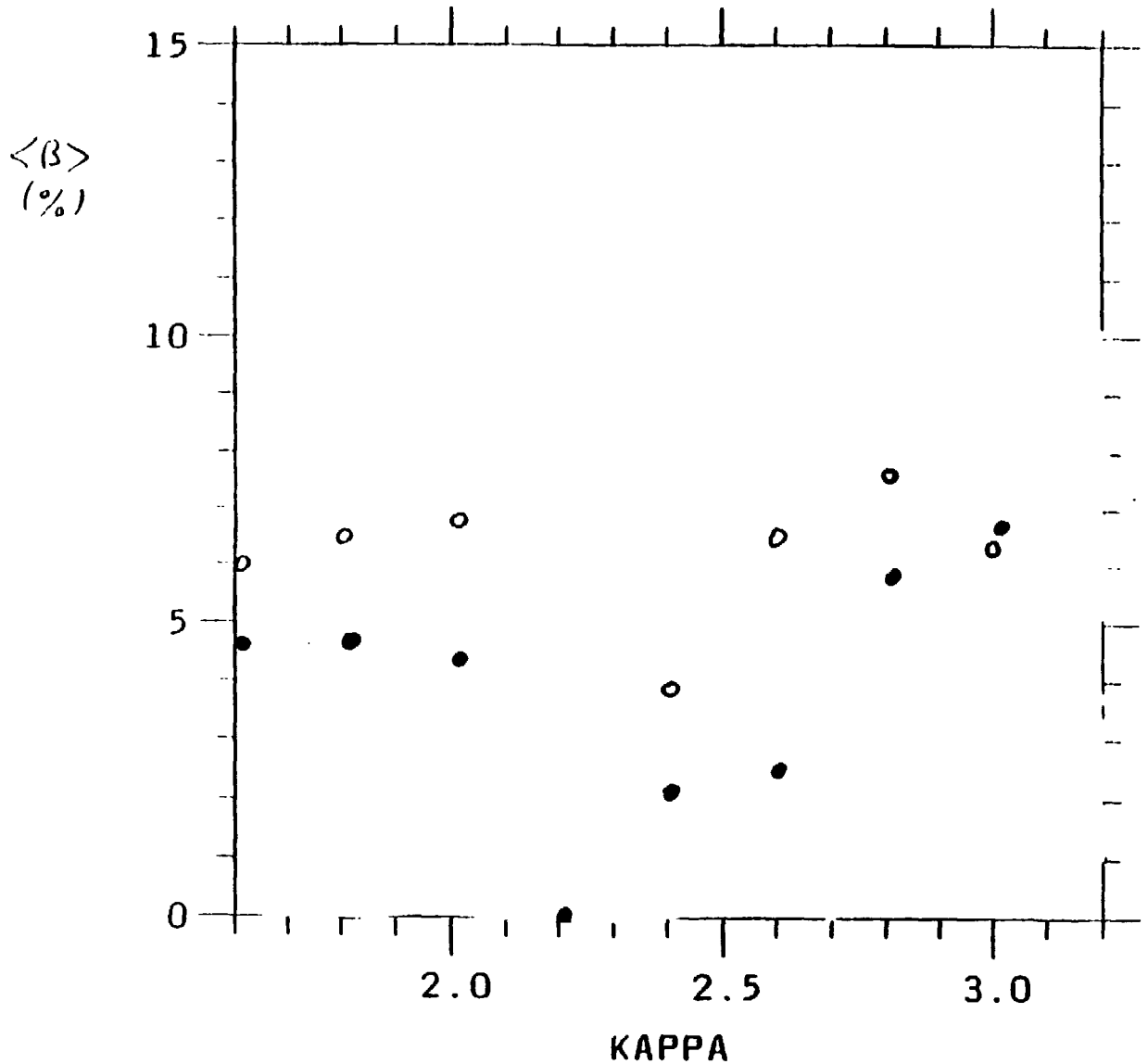
15
10
5
0
<β>
(%)
2.0
2.5
3.0
KAPPA

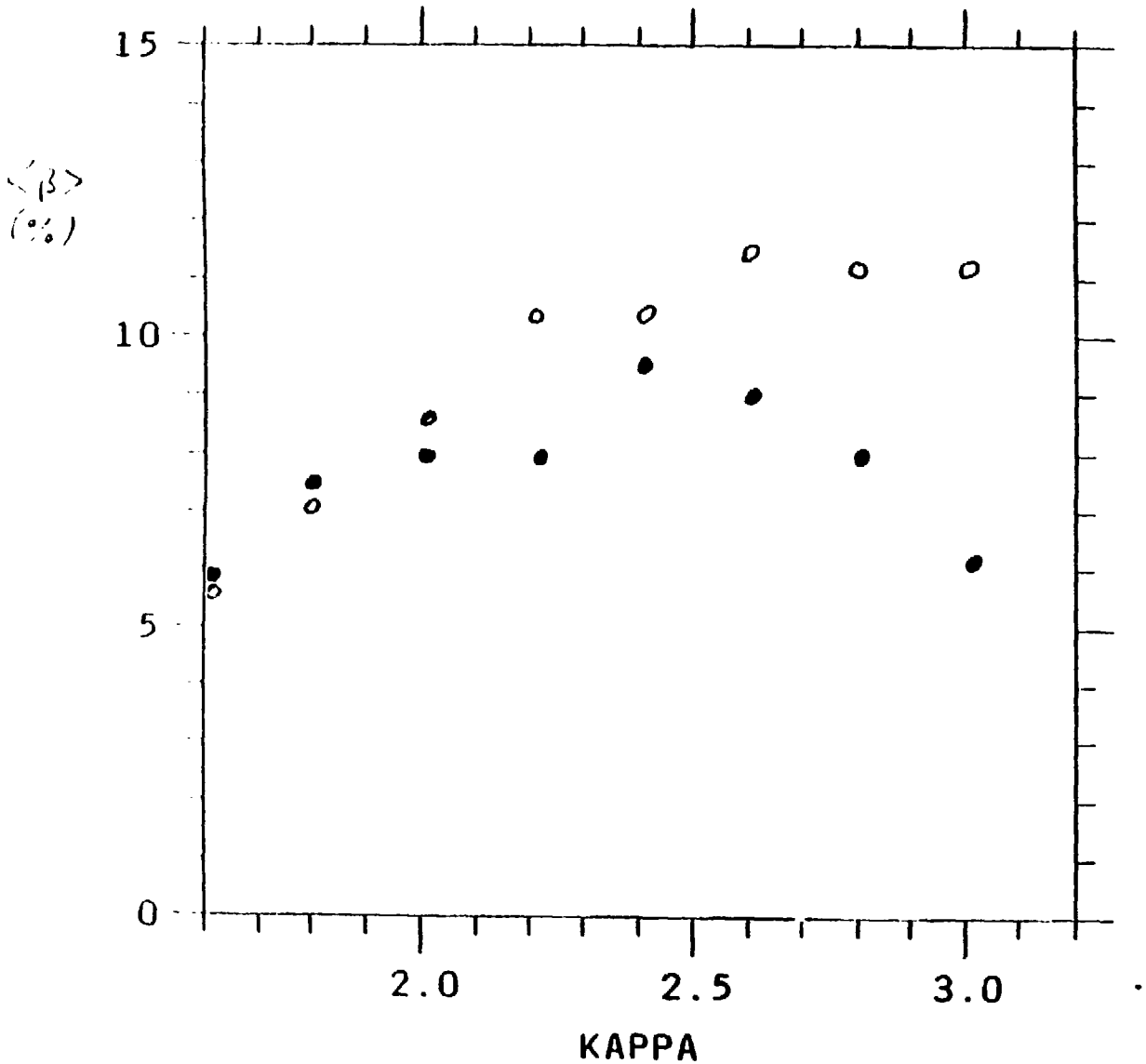
15
10
5
0
<β>
(%)
2.0
2.5
3.0
KAPPA

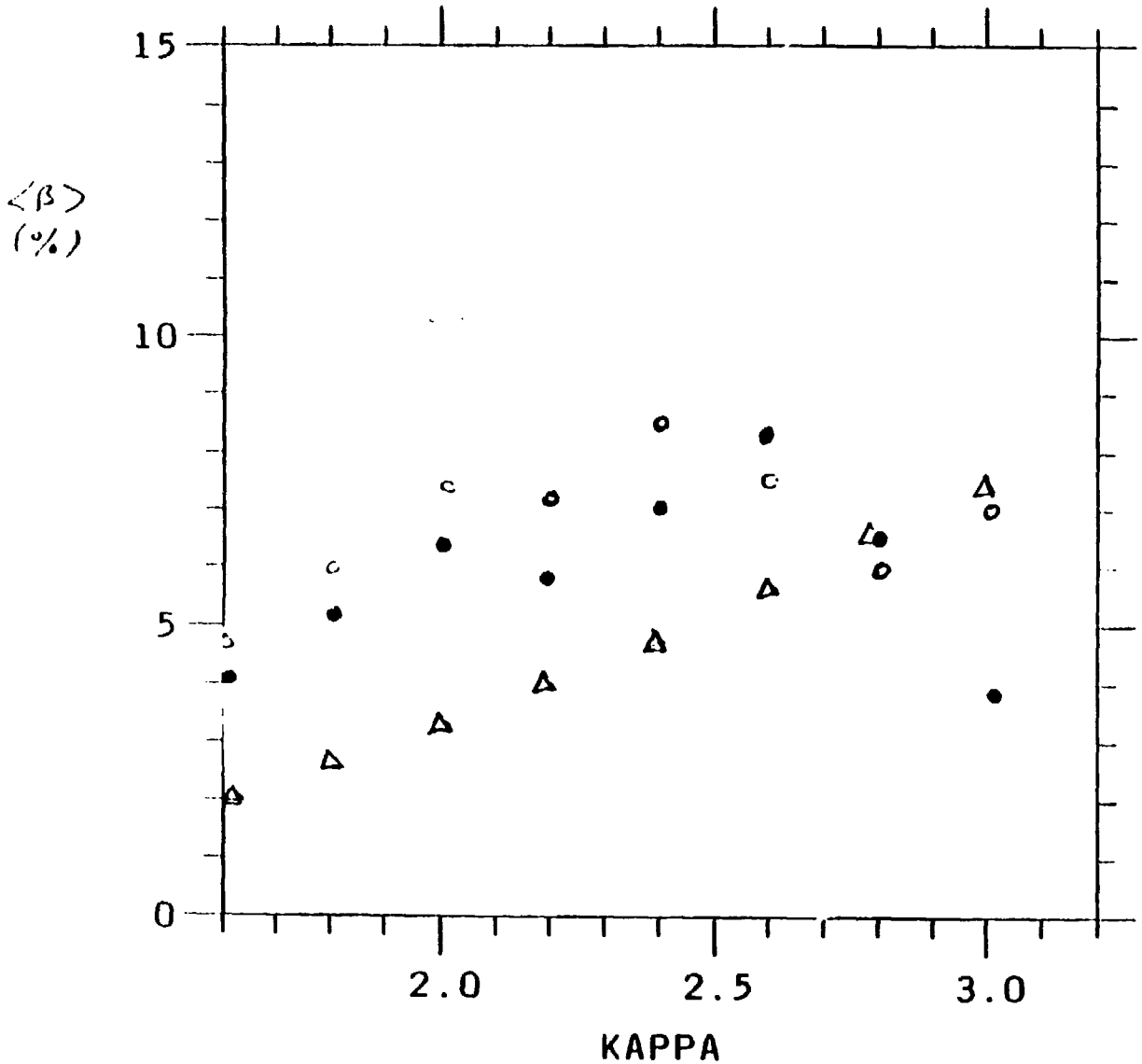

18a

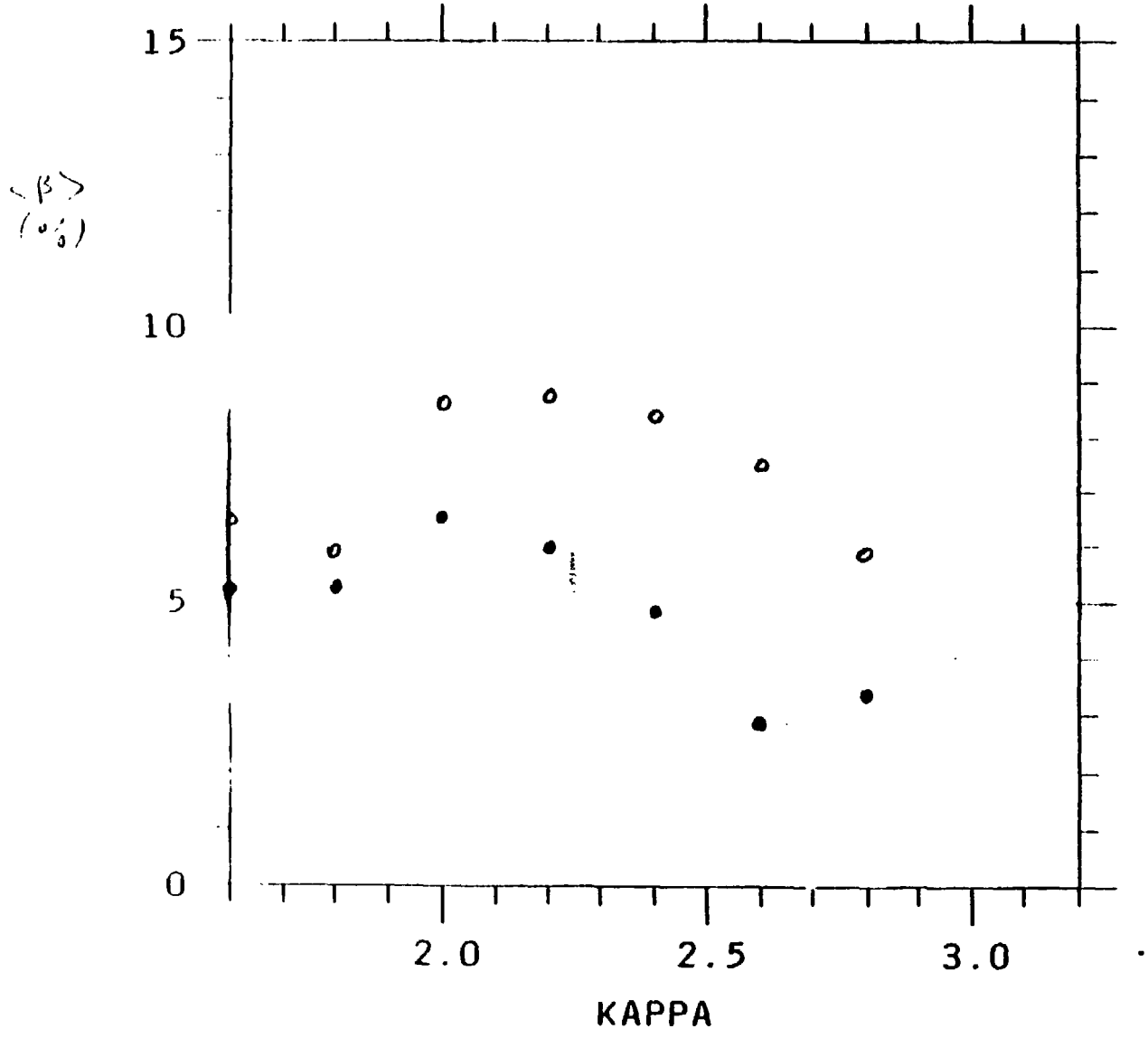

19a

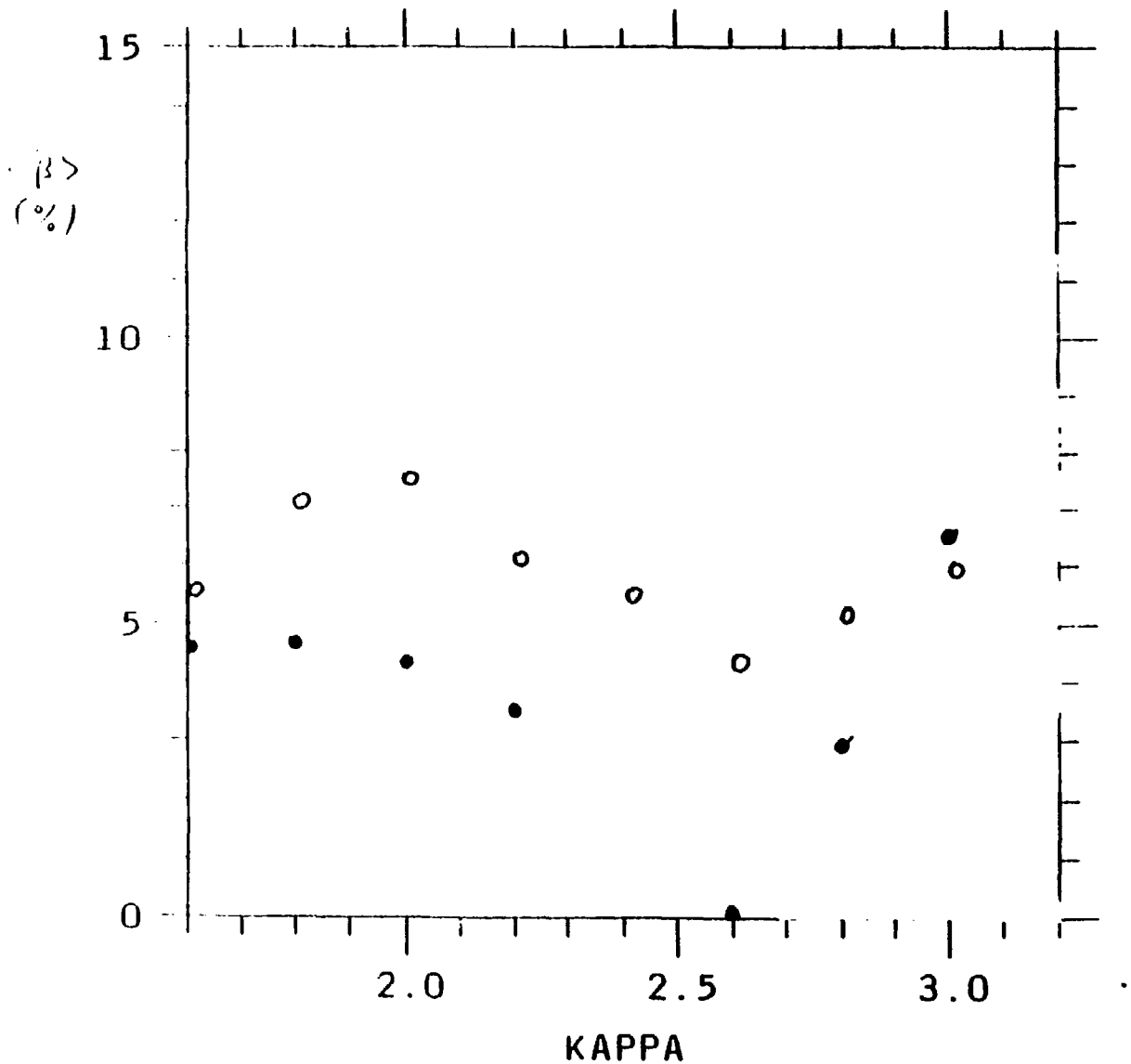
15
10
5
0
β>
(%)
2.0
2.5
3.0
KAPPA

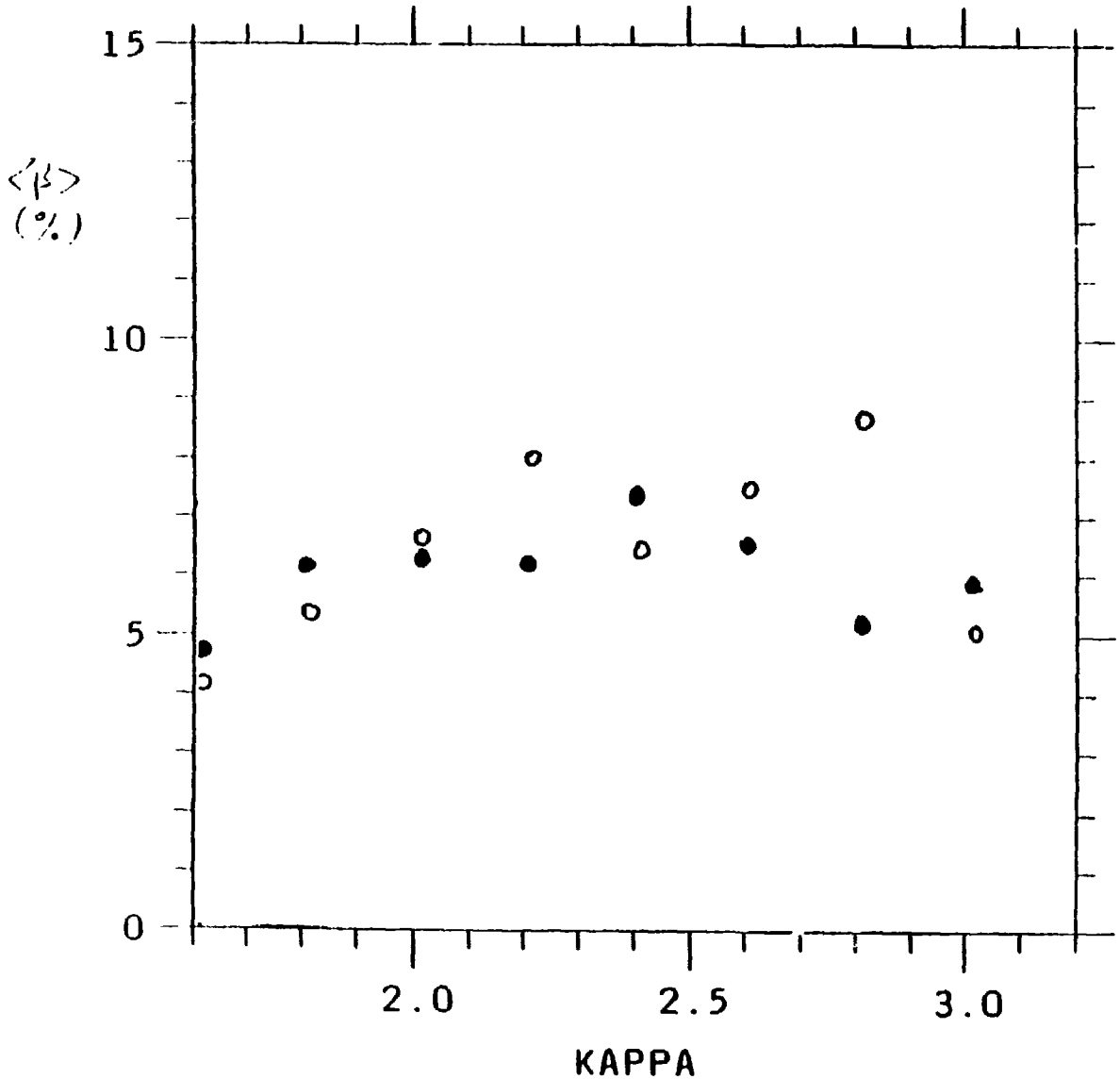
15
10
5
0
<β>
(%)
2.0
2.5
3.0
KAPPA

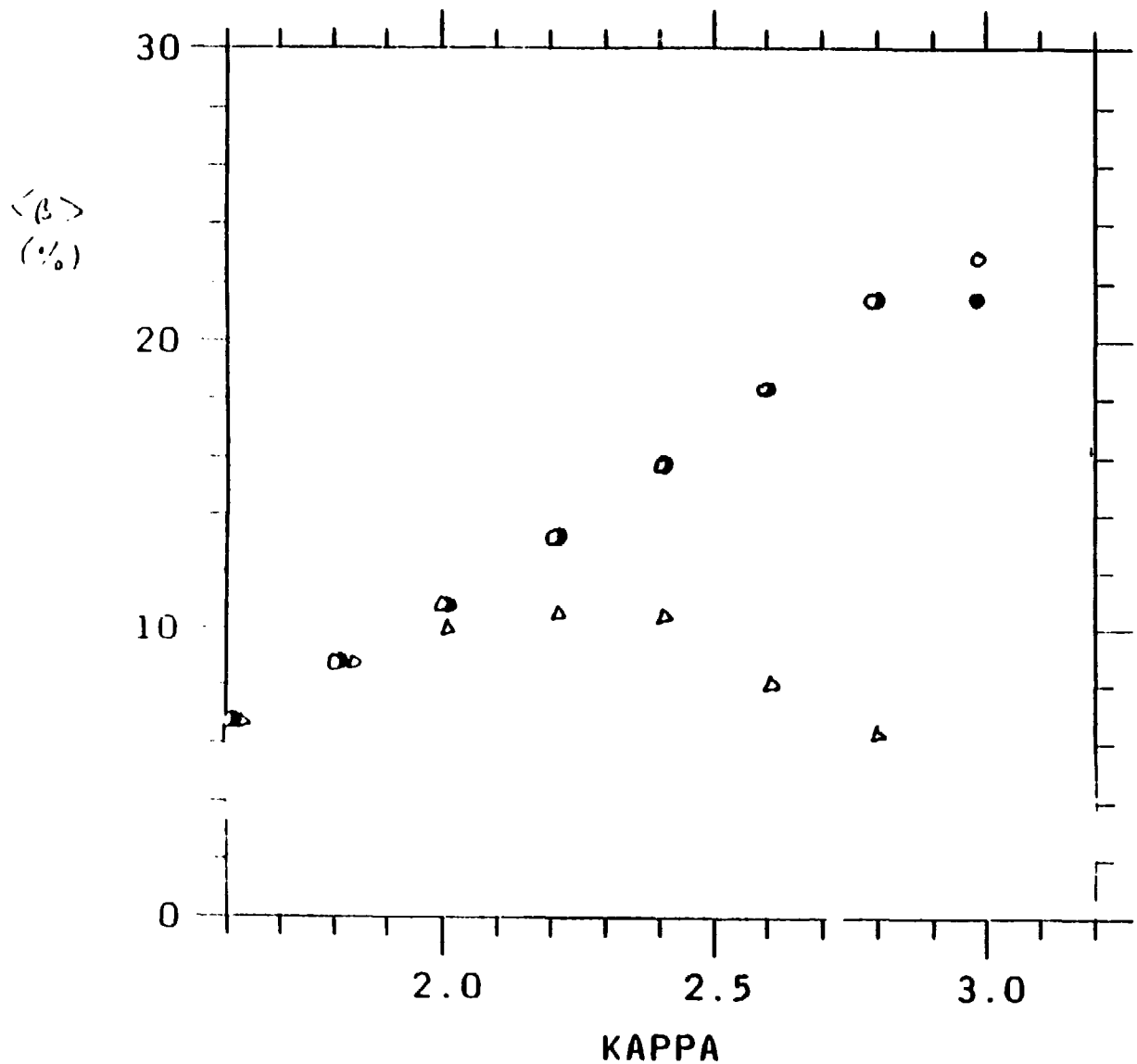

20a

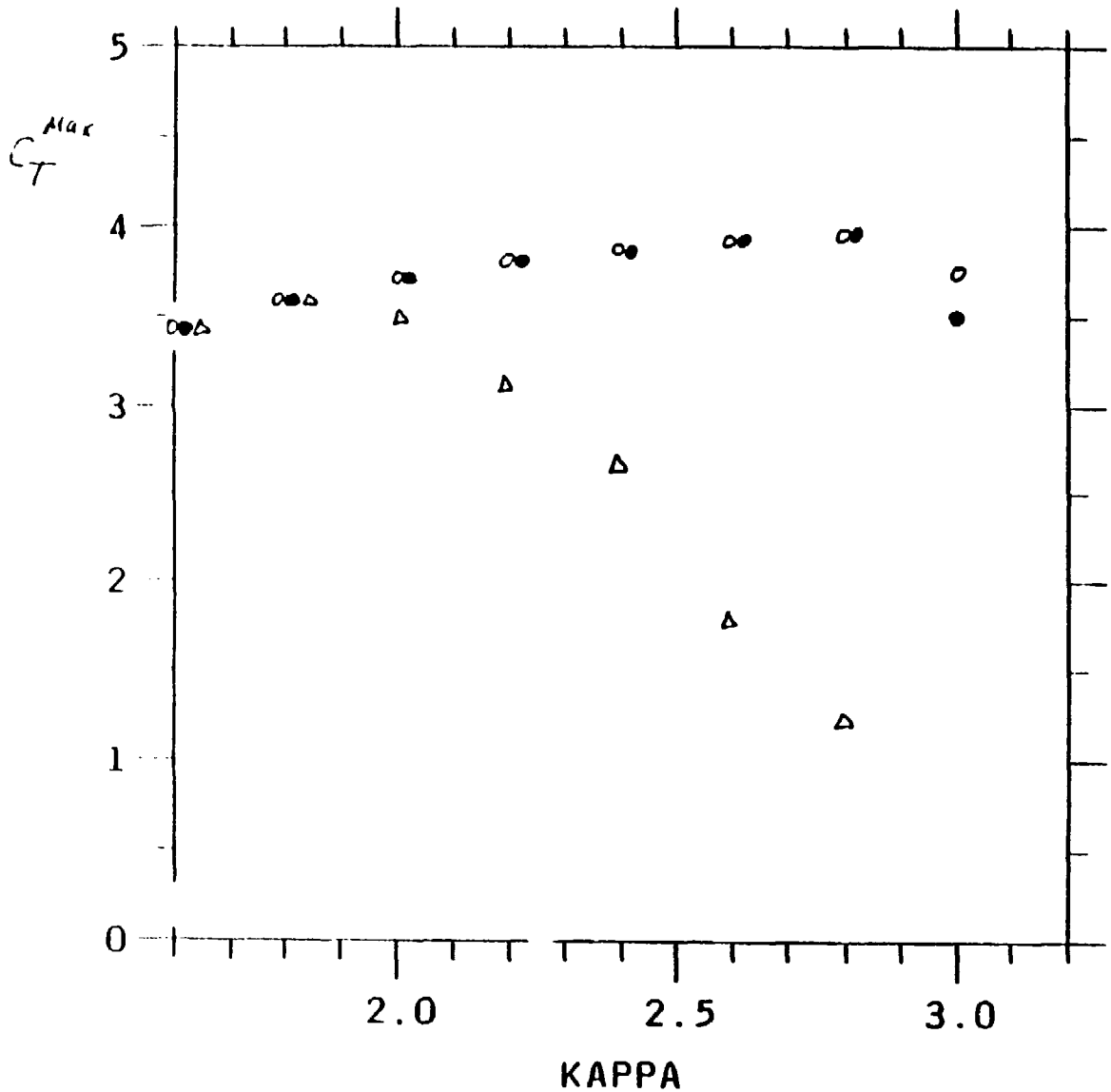

20b

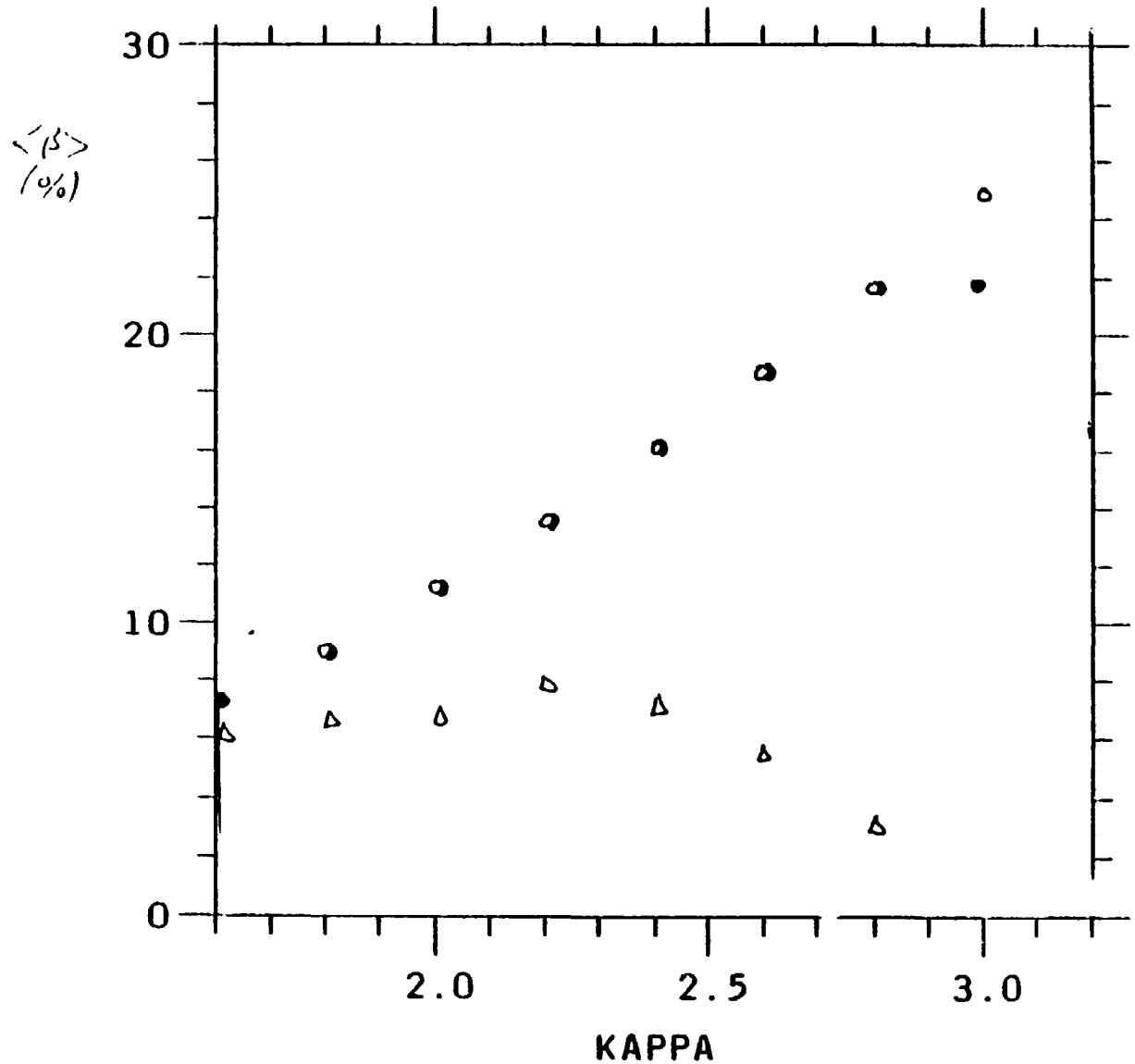
30
20
10
0
<β>
(%)
2.0
2.5
3.0
KAPPA

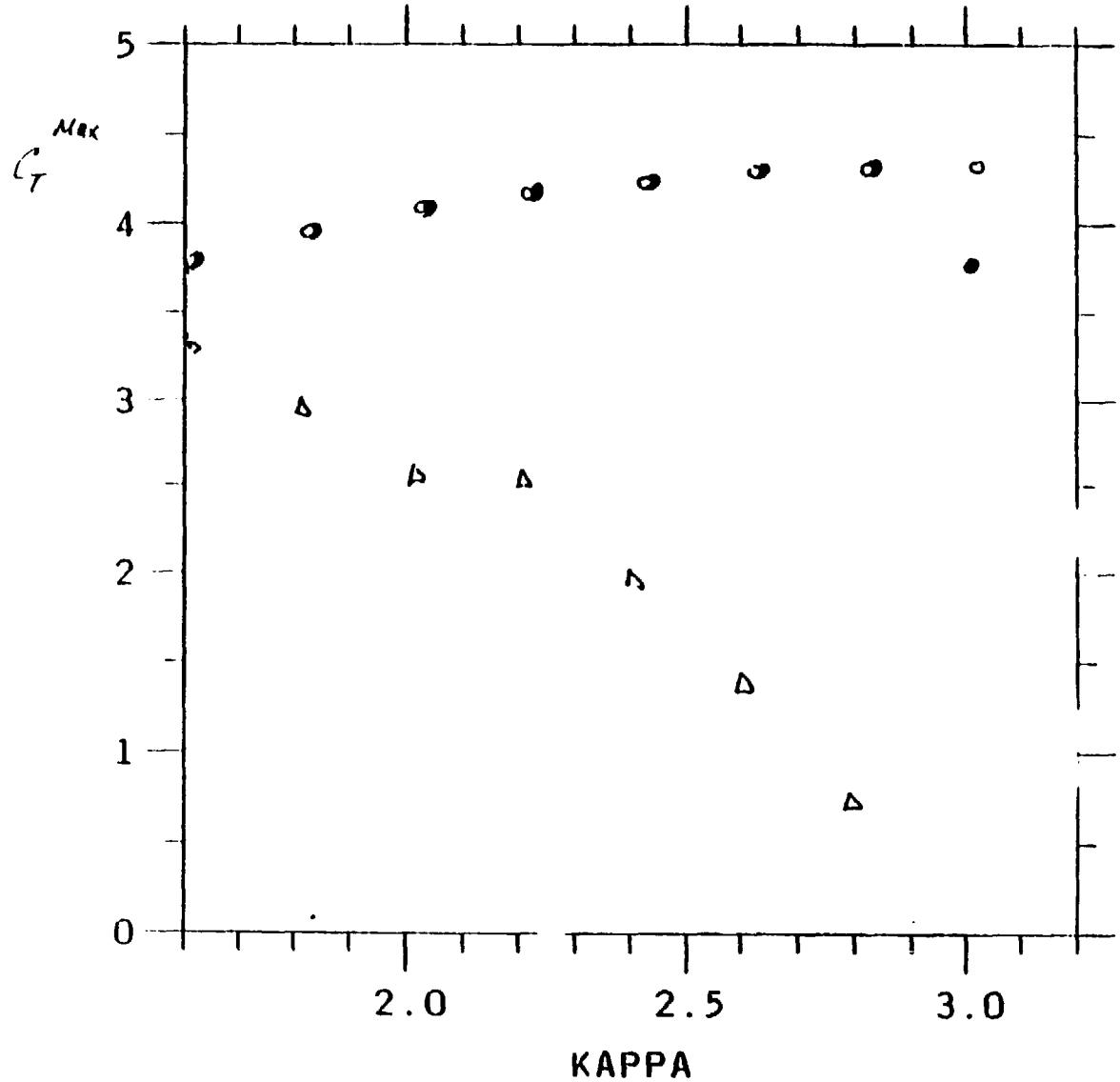
5
4
3
2
1
0
C_T^{MAX}
2.0
2.5
3.0
KAPPA

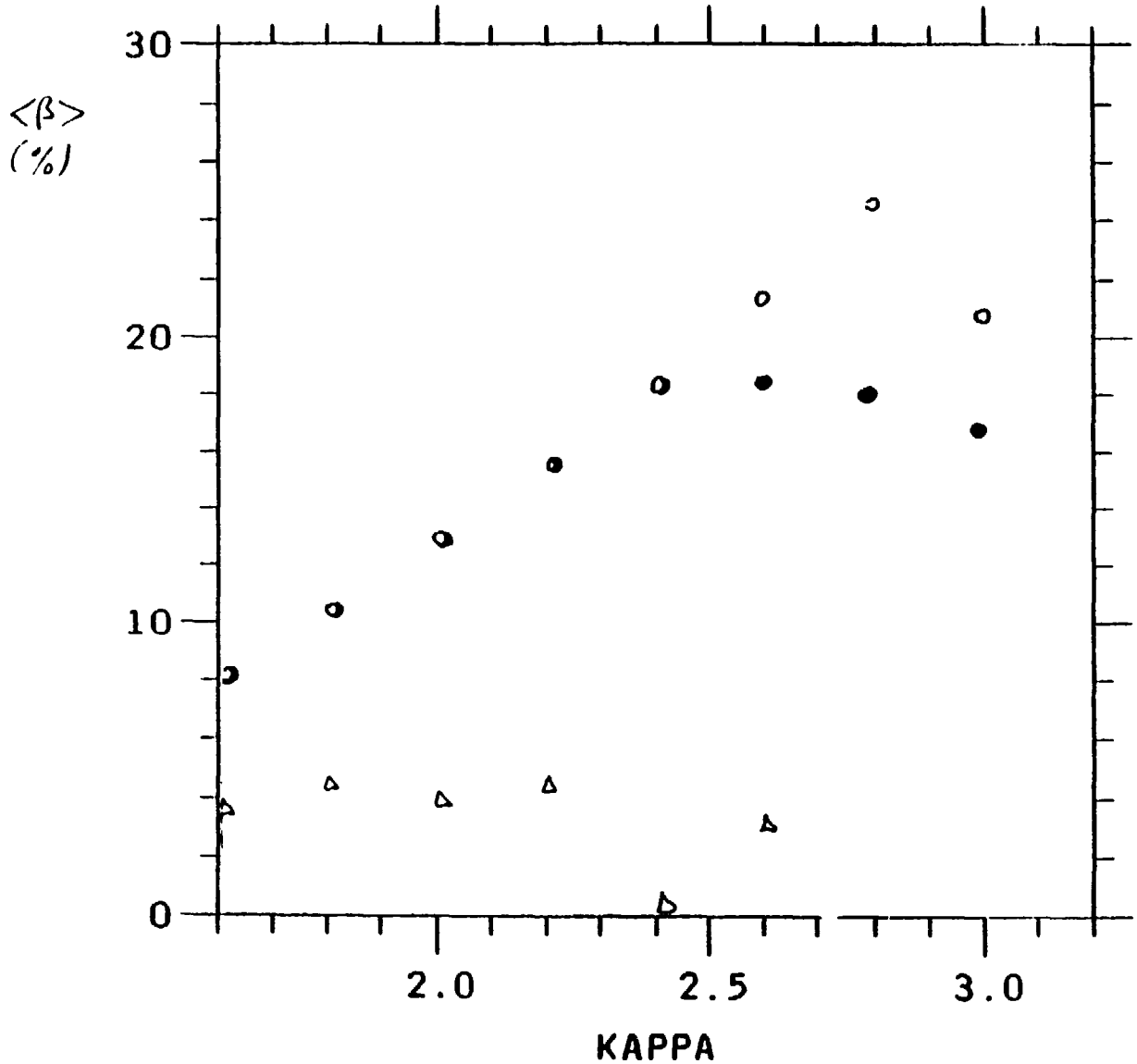
30
20
10
0
<β>
(%)
2.0
2.5
3.0
KAPPA

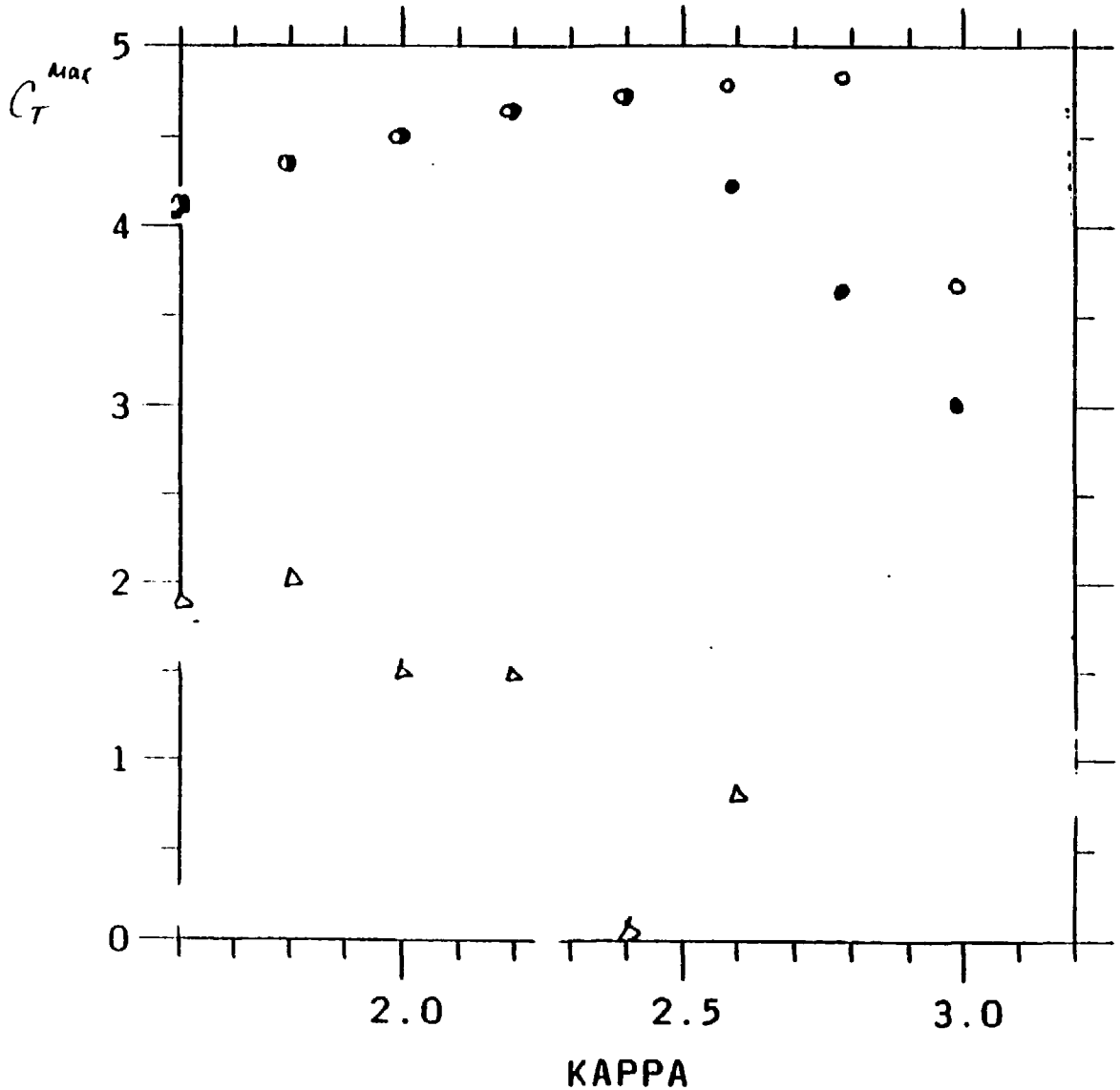
C_T^{MAX}
5
4
3
2
1
0
2.0
2.5
3.0
KAPPA

BALLOONING STABILITY BOUNDARY

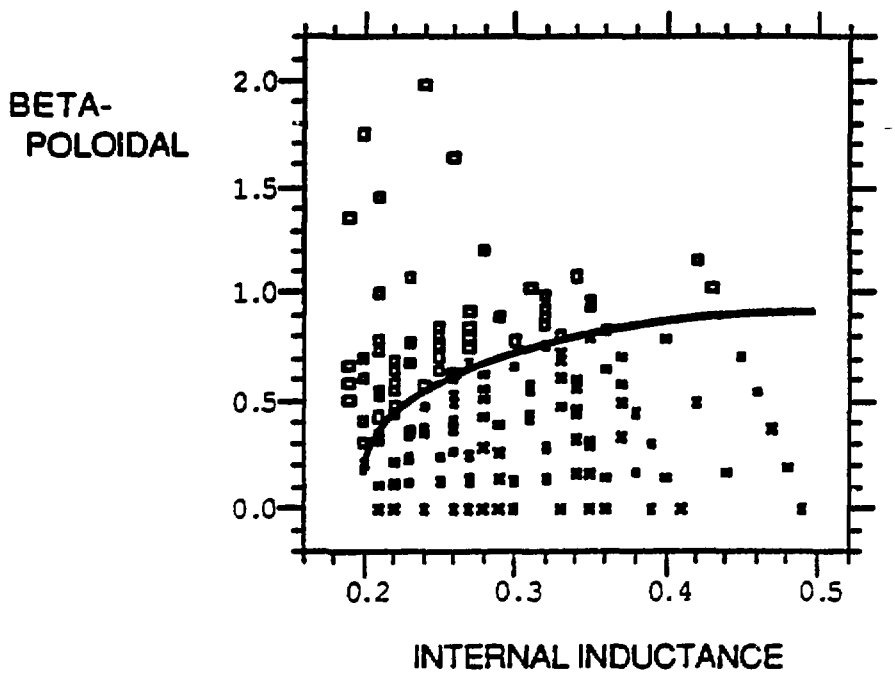

(li / 2)

LOW-n STABILITY
BOUNDARY

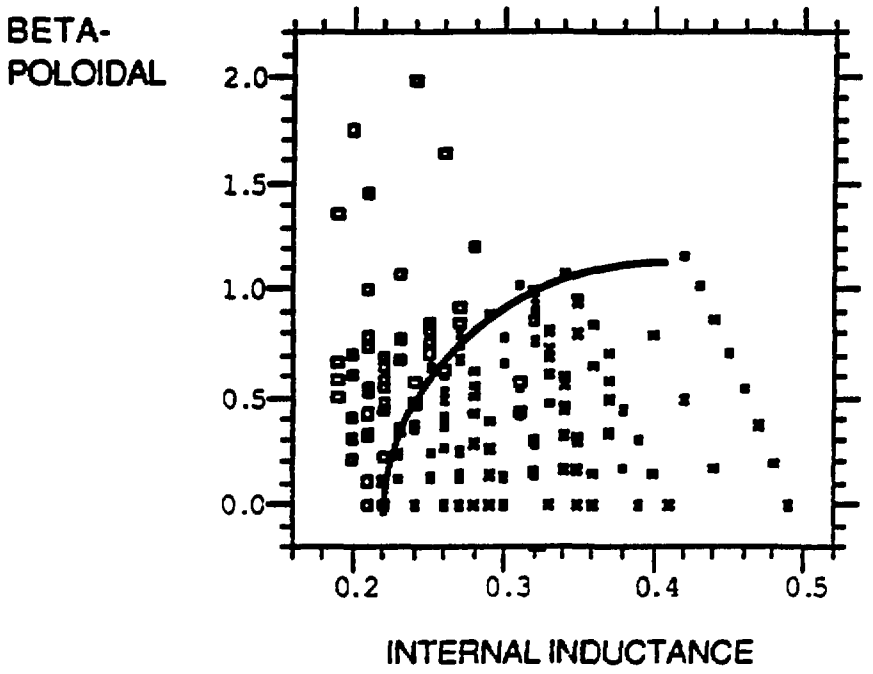

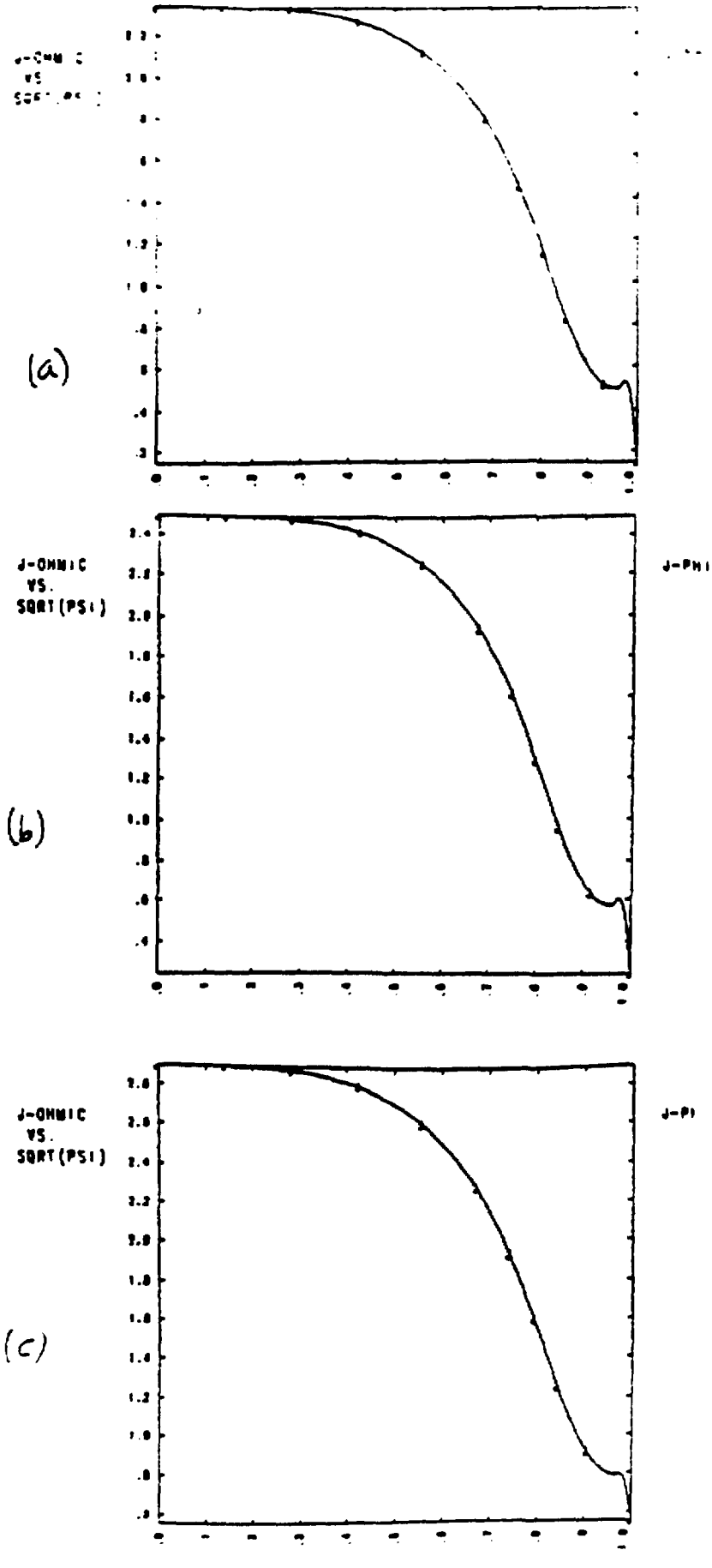

25 a-b-c

PEST I EIGENFUNCTION
ORNL DB ID ITR32

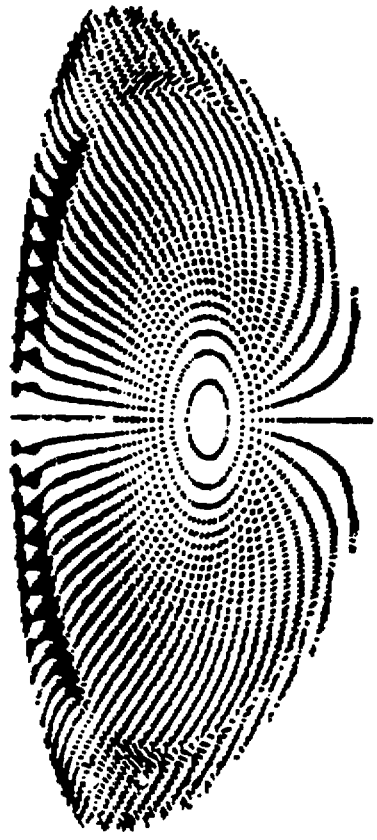

PEST 1 EIGENFUNCTION
ORNL DB ID ITR54

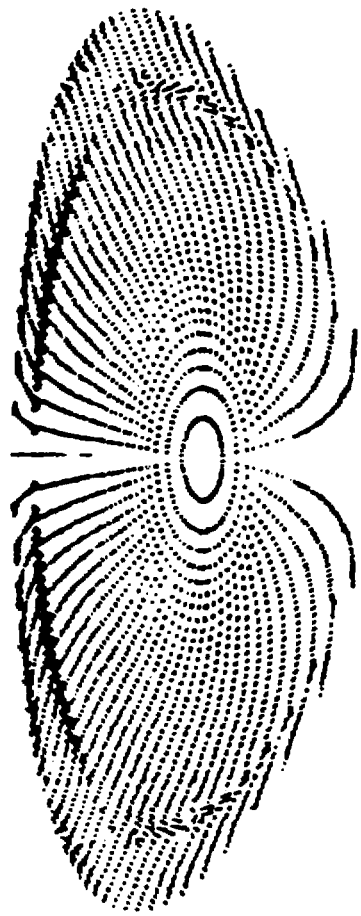

PEST I EIGENFUNCTION
ORNL DB ID ITR72

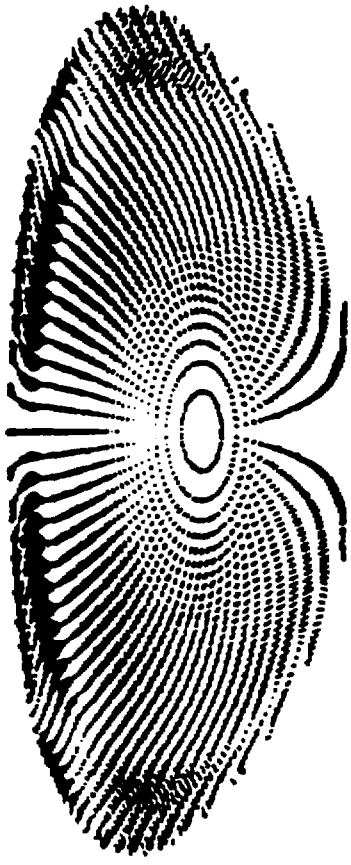

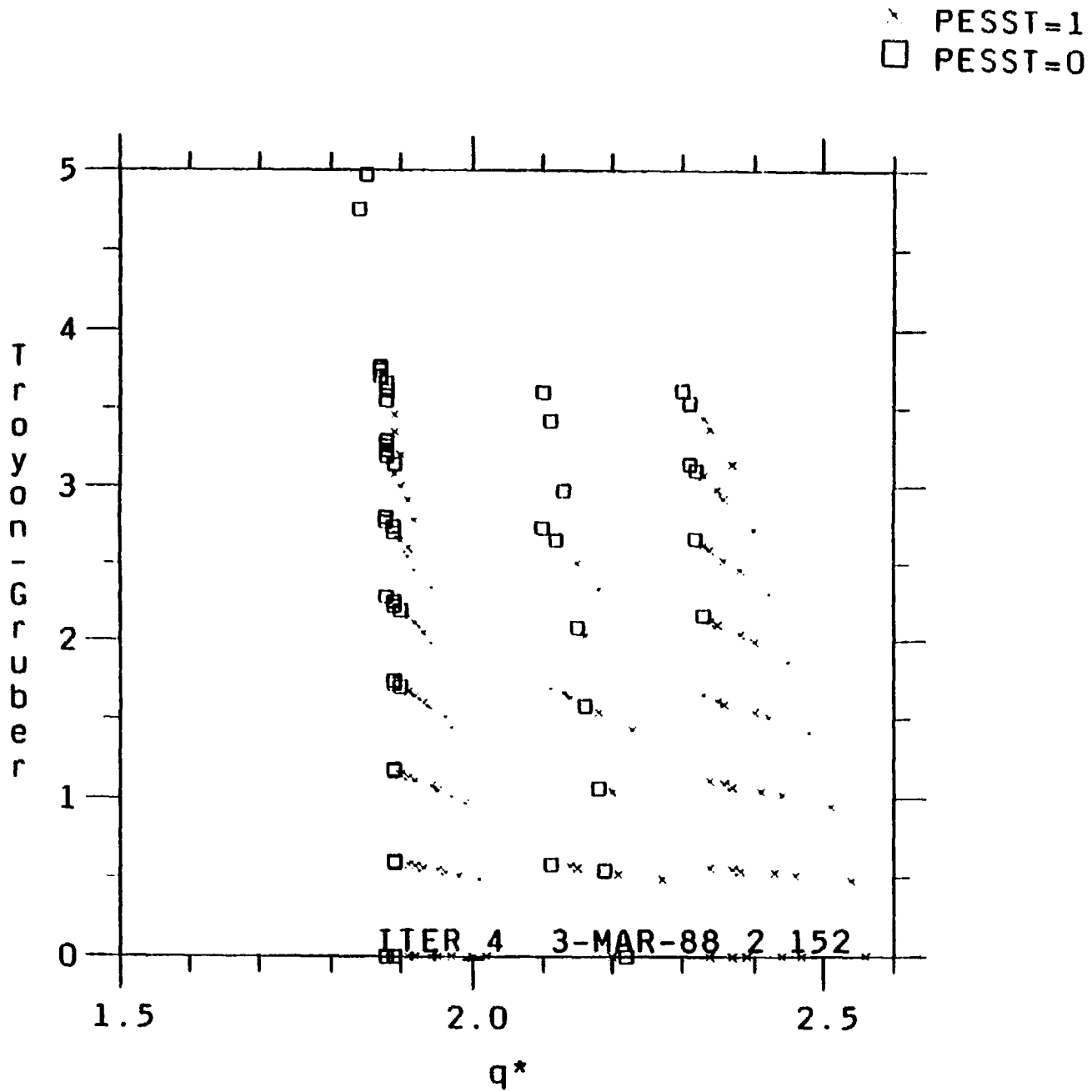
PESST=1
PESST=0
Troyon-Gruber
5
4
3
2
1
0
1.5
2.0
2.5
q*
ITER 4 3-MAR-88 2 152

2 10a

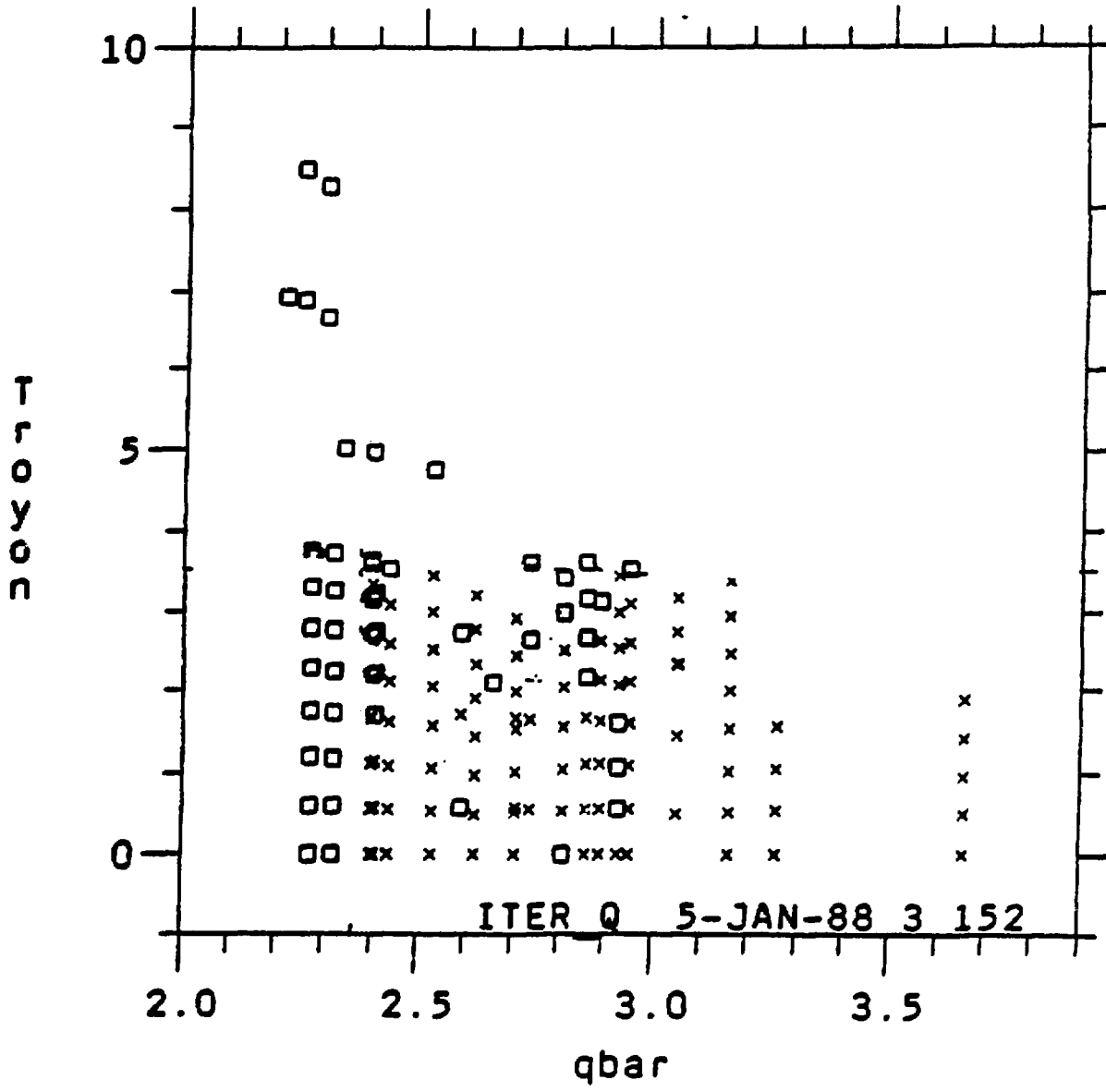

276

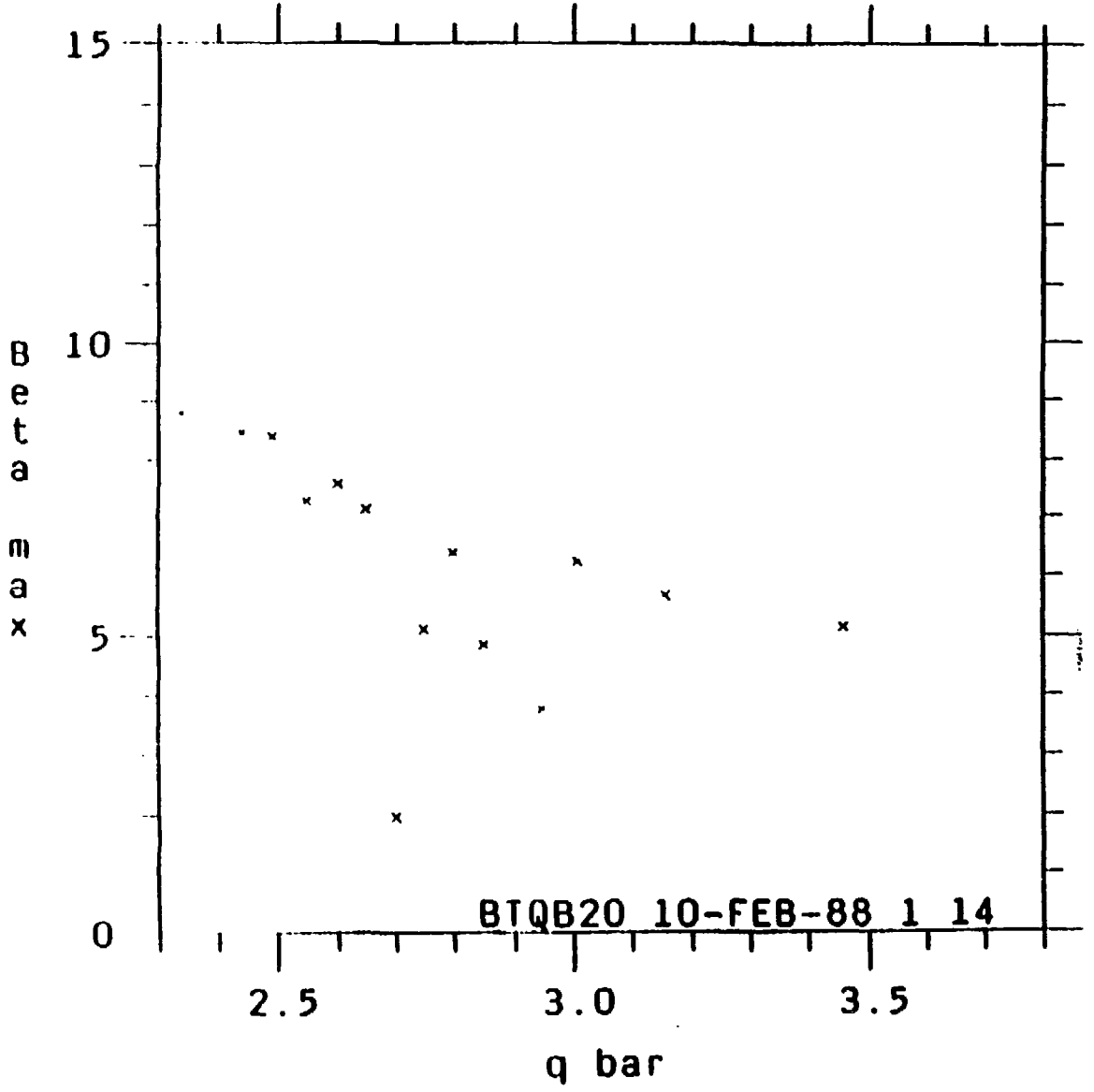
15
10
5
0
Beta max
BTQB20 10-FEB-88 1 14
2.5
3.0
3.5
q bar

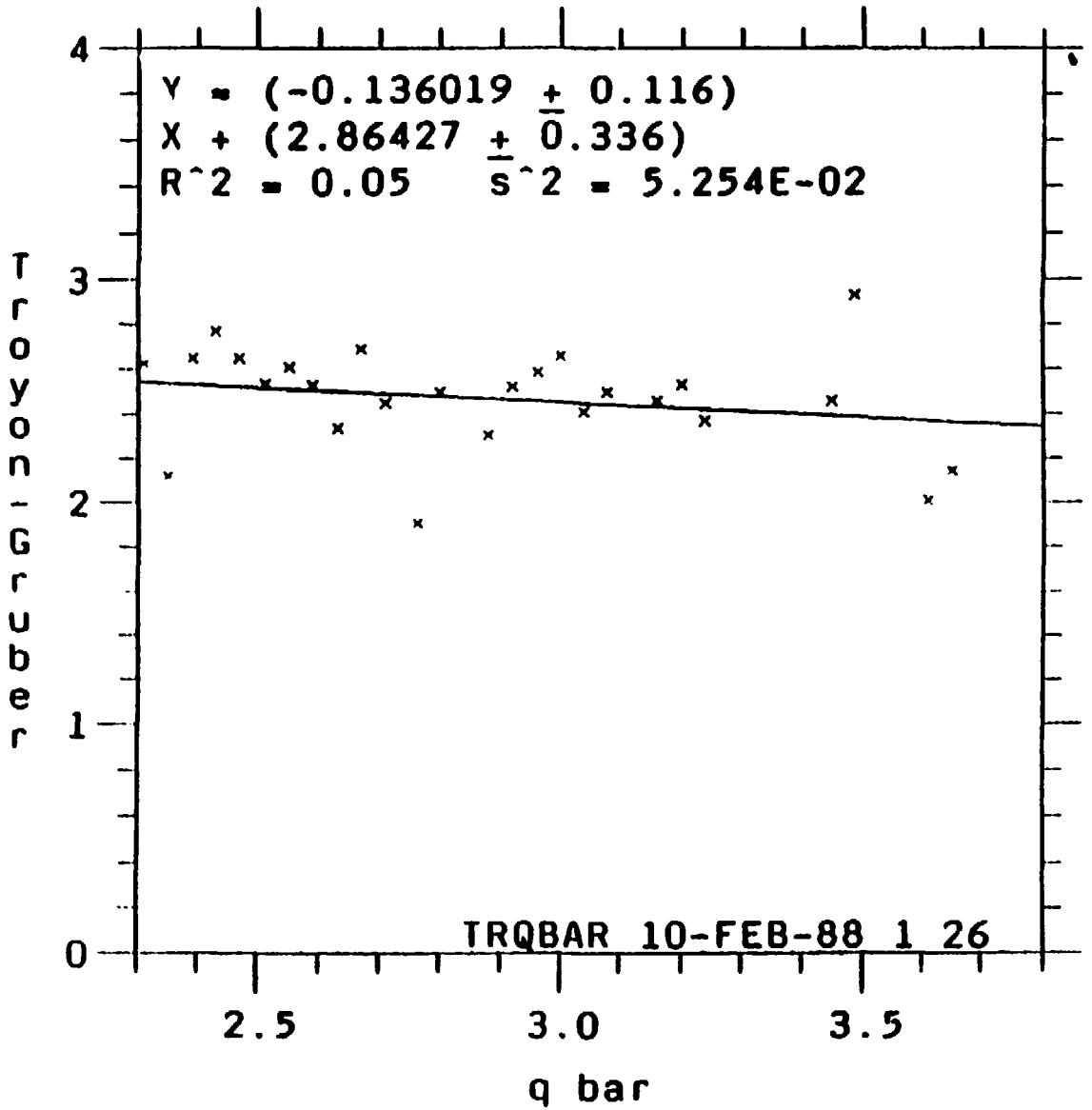
Y = (-0.136019 ± 0.116)
X + (2.86427 ± 0.336)
R^2 = 0.05 s^2 = 5.254E-02
TRQBAR 10-FEB-88 1 26
Troyon-Gruber
q bar
0
1
2
3
4
2.5
3.0
3.5

285

APPENDIX I

DATABASE DESCRIPTION MEMO

1. Introduction

Dr. J. Manickam of PPPL, in collaboration with J. A. Holmes of ORNL, has provided a version of the PEST stability package for use at ORNL. The code was installed and made operational by J. A. Holmes.

Since the ORNL applications of the PEST codes are typical of those at other fusion laboratories, and since the benefits of a collaborative accumulation of the results of more-or-less routine ideal stability calculations are an obvious way to improve the efficiency of our work, this report is being circulated to describe the application of a database management system to the collection and analysis of data from PEST runs.

It should be noted that some of the details of the system are specialized to the ORNL version of PEST, but the approach is general enough to suggest a common format. If this is perceived to be a desirable course of action, creation of a common database could be a valuable contribution of the IPSG.

Both PEST 1.0 and PEST 2.4 are included in the code suite. The advantage of PEST 2.4 is that it eliminates the sound continuum, and solves for marginal stability. Hence, a yes/no answer for stability can be obtained without a convergence scan for each case, but at the cost of losing a solution for the unstable mode structure. PEST 1 does provide a description of unstable mode structures, but grid convergence studies are required. The ORNL database is composed mostly of PEST 2 runs, hence little attention has been paid to DBMS organisation for the accumulation and evaluation of convergence scans. This application is well suited to DBMS capabilities, however, and can be included easily.

The application described in this report deals only with scalar data, because of the limited access to output in the ORNL code versions. Eigenfunction (or δW) arrays can easily be incorporated in the system, if they are available from the code.

The constraints in the current implementation of PEST at ORNL are:

- Only CRAY-1 controllees are available at for the stability codes
- PEST scans generate large quantities of data, and only the equilibrium and mapper output can be controlled by the user.

The system as constructed has four major components:

1. COSMOS job submission files for equilibrium and stability (VAX)
2. FILEM storage system for re-usable mapper, equilibrium, and kinetic energy matrix files (LLNL)
3. A System 1032 DBMS structure for storing and retrieving equilibrium, high- and low-n stability results. (VAX)
4. A FORTRAN interface with the PPPL Locus software for plotting the results. (VAX)

2. COSMOS control file system

The PEST task on the CRAY consists of condensing the voluminous PEST output and constructing a small data base output file for CRAY → VAX transfer. This file has ingredients from as many as 5 different codes. The component sections are:

HEADER - identifies the equilibrium case
EQUILIBRIUM DATA - from the input file and results
CURRENT DENSITY - the internal inductance
BALLOONING CODE - Mercier and ballooning output
PEST 1.0 - Results of the PEST 1 calculation
PEST 2.4 - Results of the PEST 2 calculation

The batch job submission system (COSMOS) separates the PEST task into a preparatory equilibrium and mapper phase, and a subsequent low-n stability evaluation phase. The motivation for this separation is that there is a large parameter space required to be surveyed. Thus, stored equilibrium and mapper files can be re-used to investigate stability for new choices of toroidal mode number and for new boundary conditions.

2.a Equilibrium job submission

The COSMOS file COSMOS_BATCH_EQUIL generates a sequence of equilibrium, ballooning and mapper runs and stores the results in FILEM. It contains all the input data files required for an equilibrium survey. The equilibrium run generates the header file for the eventual database entry file, consisting of the pertinent parameters from the input dataset, and the key equilibrium properties from the equilibrium solution.

2.b Stability job submission.

The COSMOS stability file COSMOS_BATCH_LOWN

- retrieves equilibrium files from FILEM
- generates internal kinetic energy files for FILEM storage, if not previously run for a given mode,
- runs PEST 1.0 and/or PEST 2.4 for a specified sequence of mode numbers and wall conditions.

The internal K.E. files generated during this step can be re-used (for the same mode) for changes in wall conditions.

3. FILEM storage of map and equilibrium data base files

The equilibrium and mapper codes run as part of the PEST system generate disk files which specify the profiles, metrics, etc., for the case chosen. They need only be calculated once for each configuration, and are re-used as the mode number and wall boundary conditions are varied.

In addition, the ∞-n ballooning and Mercier calculations are attributes of the equilibrium, and the collected equilibrium properties and the results of Mercier and ballooning analyses form the equilibrium dataset.

3.a Equilibrium ID

The mapper and dataset files are stored in FILEM areas identified by an equilibrium ID (EQUIL_ID), which is subsequently used as the key index for the stability results.

In the ORNL implementation this ID has the structure:

ABnmm

where

AB is a two letter Data Set ID (e.g. ER to denote ETR)

n identifies a family of equilibria in this data set.

mm identifies the individual family member

3.b FILEM ID

The PEST files referring to an equilibrium sequence with equilibrium ID equal to ABn are stored in FILEM area .ABn . The naming conventions are described in Table 1.

4. PEST / System 1032 Database Management System

The CRAY-generated data file is read by a FORTRAN program on the VAX, (PEST_1032.FOR), where the data are converted into a 1032-readable record. This record is added by PEST_1032.FOR to the relevant 1032 dataset and database, as directed by the database output file header produced on the CRAY.

The 1032 DBMS database-dataset structure allows use of the 1032 commands for selecting interesting data collections for examination. The software is designed to allow complex search criteria to be specified, and to join related datasets (e.g. equilibrium, high-n, and low-n) which meet these criteria. System 1032 macro instructions (PRINT) are used to construct output files which are then read and manipulated by the LOCUS code.

The steps in producing the data set are:

4.a CRAY data file generation for 1032 data base

4.a.1 Data file header

The four code steps involved in a stability calculation (equilibrium, current density, high-n and low-n stability) each contribute data to the data base data file. This file is constructed by the COSMOS routine as the job proceeds. Thus, a header is constructed before the equilibrium sequence is run, and contains the information shown in Table 2.

4.a.2 Equilibrium data added to data file

The equilibrium (go100jh) and current density (gocurryb) evaluation steps add the basic equilibrium data to this header described in Table 3.

4.a.3 High-n data added to data file

The Mercier and ballooning stability analysis (gobalyb) contribute additional data to the accumulating data file. These data will be stored by 1032 in the dataset associated with the EQUIL_ID value of the equilibrium. The data are described in Table 4.

4.a.4 Low-n stability

Finally, the data describing the low-n stability results are shown in Table 5.

4.b PEST - 1032 transfer

The CRAY generated data files are concatenated into a single file (`FOR020.DAT`). The FORTRAN program PEST_1032.FOR reads and records the data. This program uses 1032 macro files BETA.DMC and BETDEL.DMC.

A listing of this FORTRAN routine is given in Appendix 1.

5. LOCUS interface

The data base structure of 1032 allows the selection of desired data combinations using constraints on the data recorded. For example, one might typically select only cases with toroidal mode number = 1, with central safety factor in the range $1.01 \leq q(0) \leq 1.1$, $1.5 \leq \kappa \leq 2.5$ and so on. These selection criteria are then used to create simpler data files for use with the PPPL LOCUS software for display. The 1032 PRINT command is used to construct a data file `P1032.DAT` which is read by the LOCUS FORTRAN interface code `1032_LOCUS.FOR` to produce output database files readable by LOCUS.

The interface code 1032_LOCUS.FOR reads the `P1032.DAT` file, and produces the .DBC file required for LOCUS input. A listing of a typical variant is given in Appendix 2.

At the completion of this step, LOCUS is invoked to plot the results. Figures 1 and 2 show a sample data base scatter plot for ETR calculations, both a total plot of $< \beta_p >$ vs internal inductance, and a refined plot showing only those cases which are both balooning and low-n mode stable.

The value of the data base becomes readily apparent when translation from physical quantities (e.g., q_ψ) to engineering approximations (e.g., q^*) is required.

Table 1

FILEM STORAGE

STEP	PEST FILENAME	FILEM DESIGNATION (All in Directory .ABnmm)	
Equilibrium	EQB1	qdskABnmm	
PEST 2.4 mapper	MAPDSK	dk2ABnmm	
PEST 2.4 mapper	MPOUT1	mp2ABnmm	
PEST 1.0 mapper	MAPDSK	dk1ABnmm	
PEST 1.0 mapper	MAPOUT1	mp1ABnmm	
PEST 2.4	EQJIN, EQJOUT	j2iABnmm,	j2tABnmm
PEST 1.0	EQJIN, EQJOUT	j1iABnmm,	j1tABnmm

Table 2

DATA BASE DATA FILE HEADER

EQUIL_ID	Equilibrium ID
DATE	Date (1032 format) Month-day-year
COMMENT	comment
EQDSN	Data set name for equilibrium portion
HNDSN	Name for high-n portion
LNDSN	Name for low-n portion
IEQ IMOD IWAL	Number of equilibrium, mode, and wall cases in data set

Table 3

DATA ADDED IN EQUILIBRIUM STEP

NTHE	Number of θ points
NPSIE	Number of ψ points
ALPHA	Pressure profile parameter
BETA	Pressure profile parameter
ELLIPT	Elongation
DEITY	Triangularity
QLIM2	q profile parameter
QPOF2	q profile parameter
P1	Pressure profile parameter
ALPHA2	Pressure profile parameter
BETA2	Pressure profile parameter
Q0	q profile parameter
QLIM	q profile parameter
QPOF	q profile parameter
XMAG	Axis shift
BETAEQ	Average β
BETAI	Engineering β_{pol}
AREA	Cross section
PBAR	P-profile shape factor
CURRENT	Total current
P00	Axis β
LI	Internal inductance

Table 4
HIGH-N DATA

Quantity	Description	Comment
LAMBDA	Ballooning growth rate	(0. if stable)
KAPPAS	Geodesic curvature contribution to growth rate	
KAPPAP	Normal curvature contribution to growth rate	
ALPHAB	Line bending contribution to growth rate	
BALLOON_STABLE	Logical	Overall Balooning Stability
MRCSTB_SURF5	Logical	Mercier stability for surface 5
MRCSTB_SURF15	Logical	" 15
MRCSTB_SURF25	Logical	" 25
MRCSTB_SURF35	Logical	" 35
MRCSTB_SURF45	Logical	" 45
MRCSTB_SURF55	Logical	" 55
MRCSTB_SURF65	Logical	" 65
MERCIER_STABLE	Logical	Overall Mercier stability

Table 5
LOW-N DATA

Quantity	Description	Comment
Betapol	Real	Poloidal beta
B	Real	Plasma/ wall radius
INFWAL	Logical	Yes if at ∞
SURF	Logical	Yes is at surface
P_2_STABLE	logical	Yes if PEST_2 stable
P_1_STABLE	logical	Yes if PEST_1 stable
P_2_Hiquality	Logical	Yes if numerics OK
P_1_Hiquality	Logical	Yes if numerics OK

REFERENCES

1. System 1032 User's Guide, Software House, Cambridge, MA, Sept. 1986.
2. J. A. Murphy, LOCUS Database System, ISAM Version 5.0, PPPL Internal Memo, July 1987.

APPENDIX 2

SCALING FITS

The fits for cases discussed in Section 5 are presented here. The specific cases treated are :

C_T^{max} vs κ for δ=0.2 and 0.4

q_0 = 1.05, 1.20, 1.40

q_ψ = 3.1, 3.6, 4.1

The least squares fits to the maximum values of C_T found in the database as a function of κ are given in the form :

$$C_T = a_0 + a_1 \cdot \kappa + a_2 \cdot \kappa^2$$

and the values for the coefficients are given in the Table.

Table : Fitting coefficients

Figure	δ	q_ψ	q(0)	a_0	a_1	a_2
A.1	0.4	3.1	1.05	-7.23857	9.7625	-2.40179
A.2			1.20	10.9932	-7.7875	1.54464
A.3			1.40	-1.02497	3.04349	-0.662879
A.4	0.4	3.6	1.05	-7.11929	9.78334	-2.50595
A.5			1.20	16.3424	-12.7827	2.60417
A.6			1.40	-2.81784	4.89125	-1.14123
A.7	0.4	4.1	1.05	4.20549	-1.12196	-0.129466
A.8			1.20	16.4382	-13.3110	2.68507
A.9			1.40	-1.17857	3.25804	-0.825893
A.10	0.2	3.1	1.05	-5.12268	8.13185	-2.12351
A.11			1.20	3.76217	-0.309416	-0.21158
A.12			1.40	3.33175	-0.177207	-0.16829
A.13		3.6	1.05	-0.315717	3.70238	-1.22619
A.14			1.20	11.4254	-7.62066	1.35465
A.15			1.4	-2.40393	4.95046	-1.25027

The Figures showing these fits are given as A 1-15.

APPENDIX 2

SCALING FITS

The fits for cases discussed in Section 5 are presented here. The specific cases treated are :

C_T^{max} vs κ for δ=0.2 and 0.4

q_0 = 1.05, 1.20, 1.40

q_ψ = 3.1, 3.6, 4.1

The least squares fits to the maximum values of C_T found in the database as a function of κ are given in the form :

$$C_T = a_0 + a_1 \cdot \kappa + a_2 \cdot \kappa^2$$

and the values for the coefficients are given in the Table.

Table : Fitting coefficients

Figure	δ	q_ψ	q(0)	a_0	a_1	a_2
A.1	0.4	3.1	1.05	-7.23857	9.7625	-2.40179
A.2			1.20	10.9932	-7.7875	1.54464
A.3			1.40	-1.02497	3.04349	-0.662879
A.4	0.4	3.6	1.05	-7.11929	9.78334	-2.50595
A.5			1.20	16.3424	-12.7827	2.60417
A.6			1.40	-2.81784	4.89125	-1.14123
A.7	0.4	4.1	1.05	4.20549	-1.12196	-0.129466
A.8			1.20	16.4382	-13.3110	2.68507
A.9			1.40	-1.17857	3.25804	-0.825893
A.10	0.2	3.1	1.05	-5.12268	8.13185	-2.12351
A.11			1.20	3.76217	-0.309416	-0.21158
A.12			1.40	3.33175	-0.177207	-0.16829
A.13		3.6	1.05	-0.315717	3.70238	-1.22619
A.14			1.20	11.4254	-7.62066	1.35465
A.15			1.4	-2.40393	4.95046	-1.25027

The Figures showing these fits are given as A 1-15.

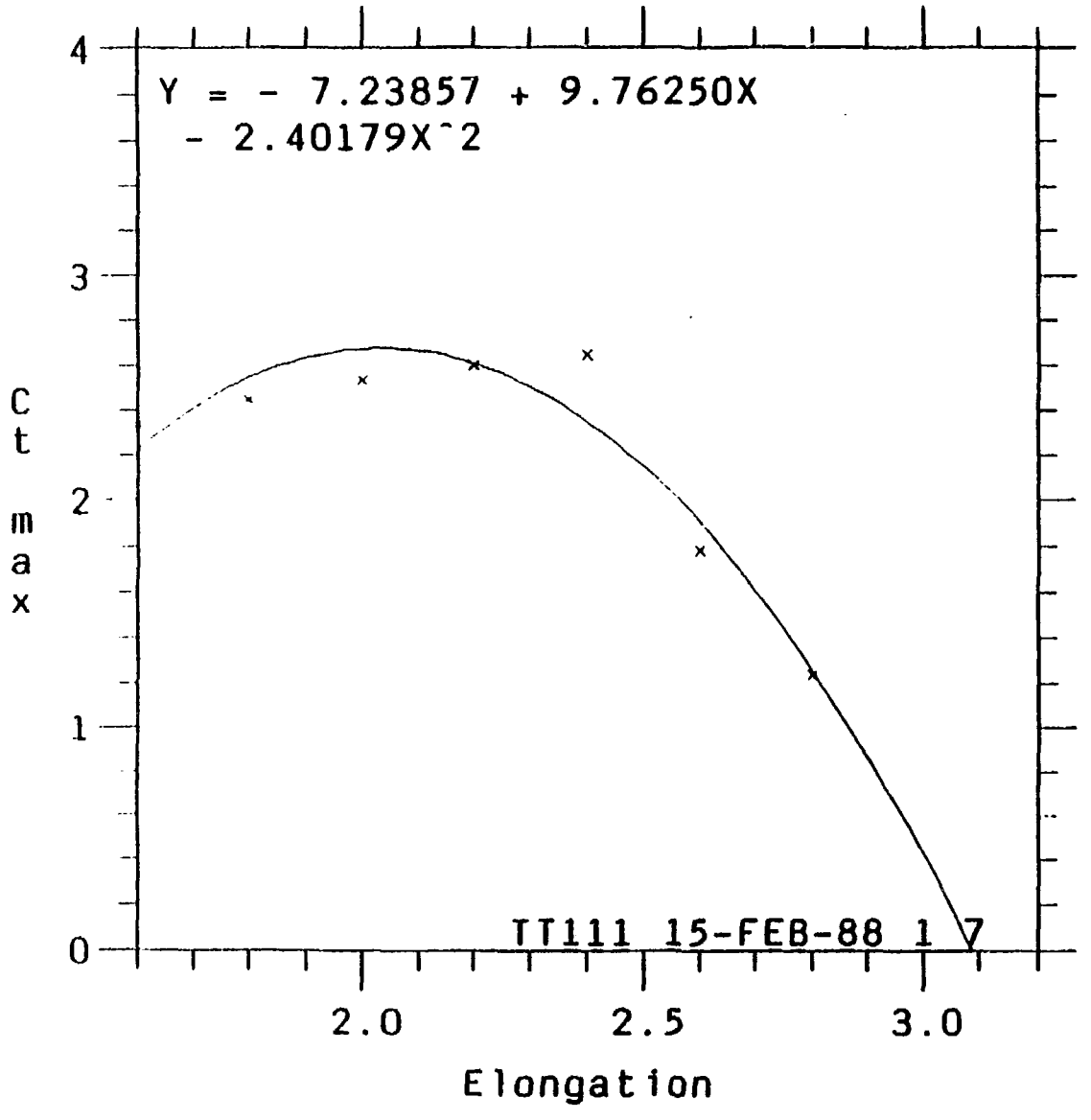
Y = - 7.23857 + 9.76250X
- 2.40179X^2
TT111 15-FEB-88 1 7
Ct max
Elongation
0
1
2
3
4
2.0
2.5
3.0

A.1

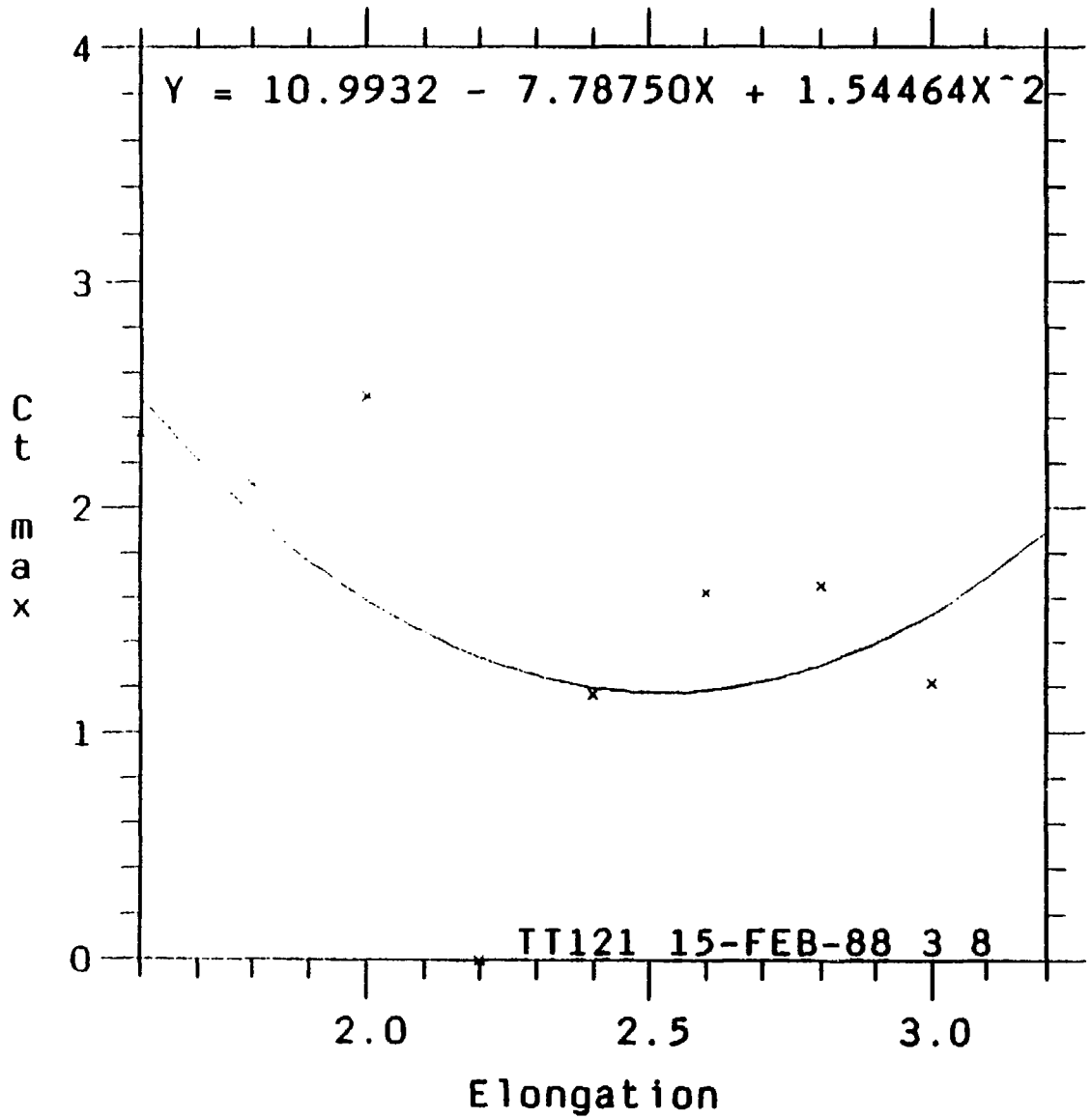
Y = 10.9932 - 7.78750X + 1.54464X^2
Ct max
4
3
2
1
0
2.0
2.5
3.0
Elongation
TT121 15-FEB-88 3 8

A.2

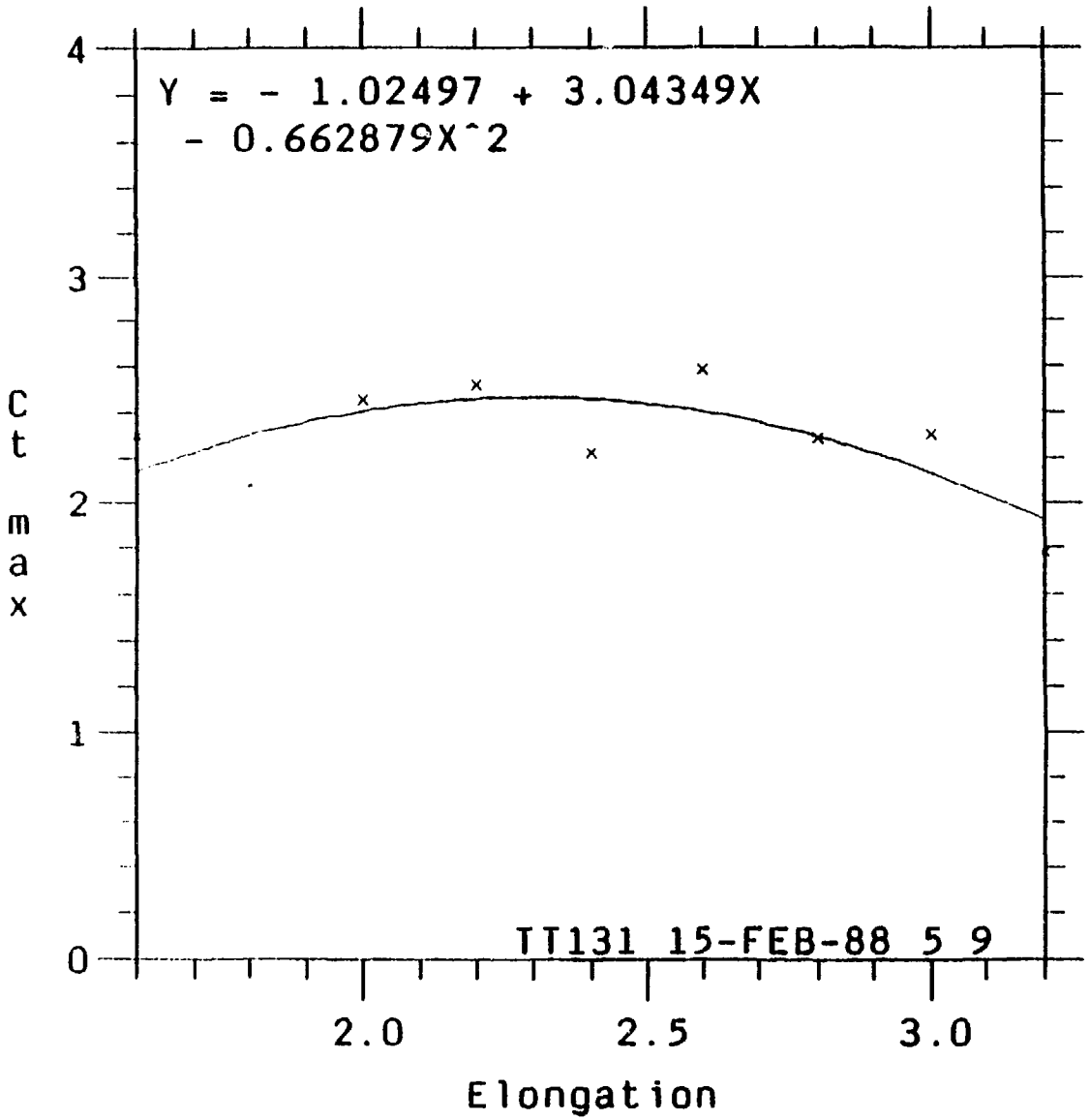
Y = - 1.02497 + 3.04349X
- 0.662879X^2
TT131 15-FEB-88 5 9
Ct max
Elongation
0
1
2
3
4
2.0
2.5
3.0

A.3

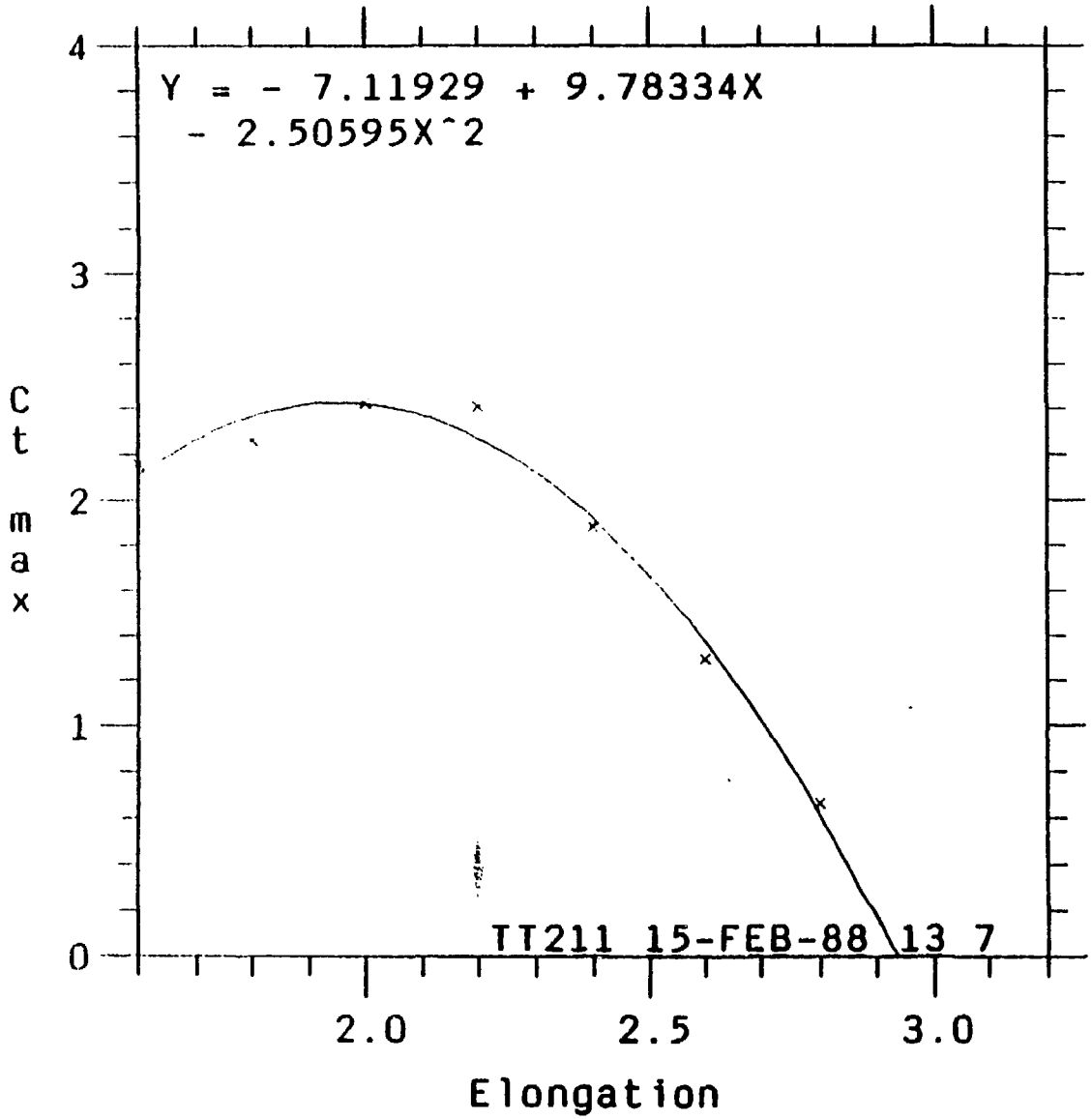
Y = - 7.11929 + 9.78334X
- 2.50595X^2
TT211 15-FEB-88 13 7
Ct max
Elongation
0
1
2
3
4
2.0
2.5
3.0

A.4

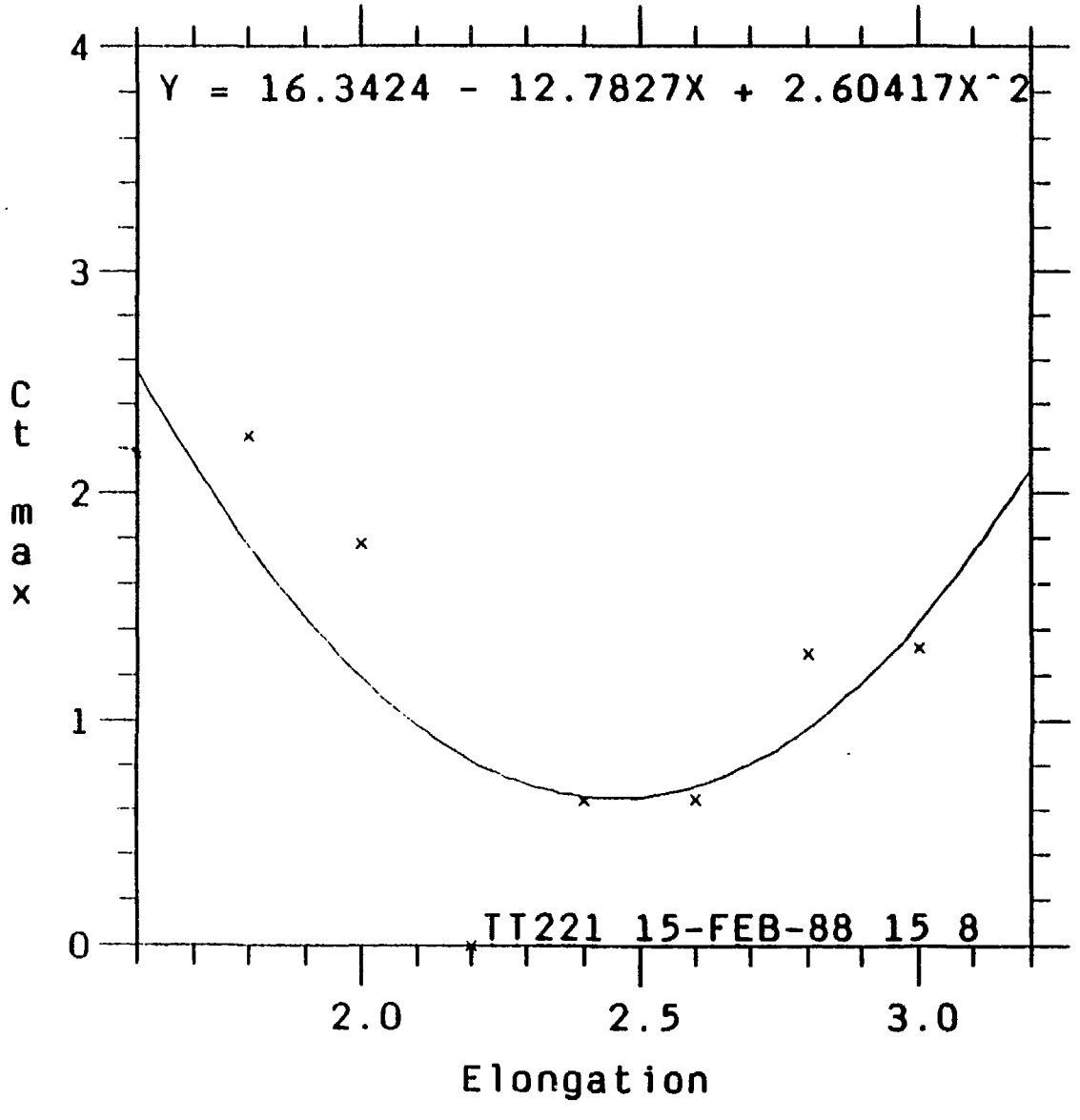
Y = 16.3424 - 12.7827X + 2.60417X^2
TT221 15-FEB-88 15 8
Ct max
Elongation
0
1
2
3
4
2.0
2.5
3.0

A.5

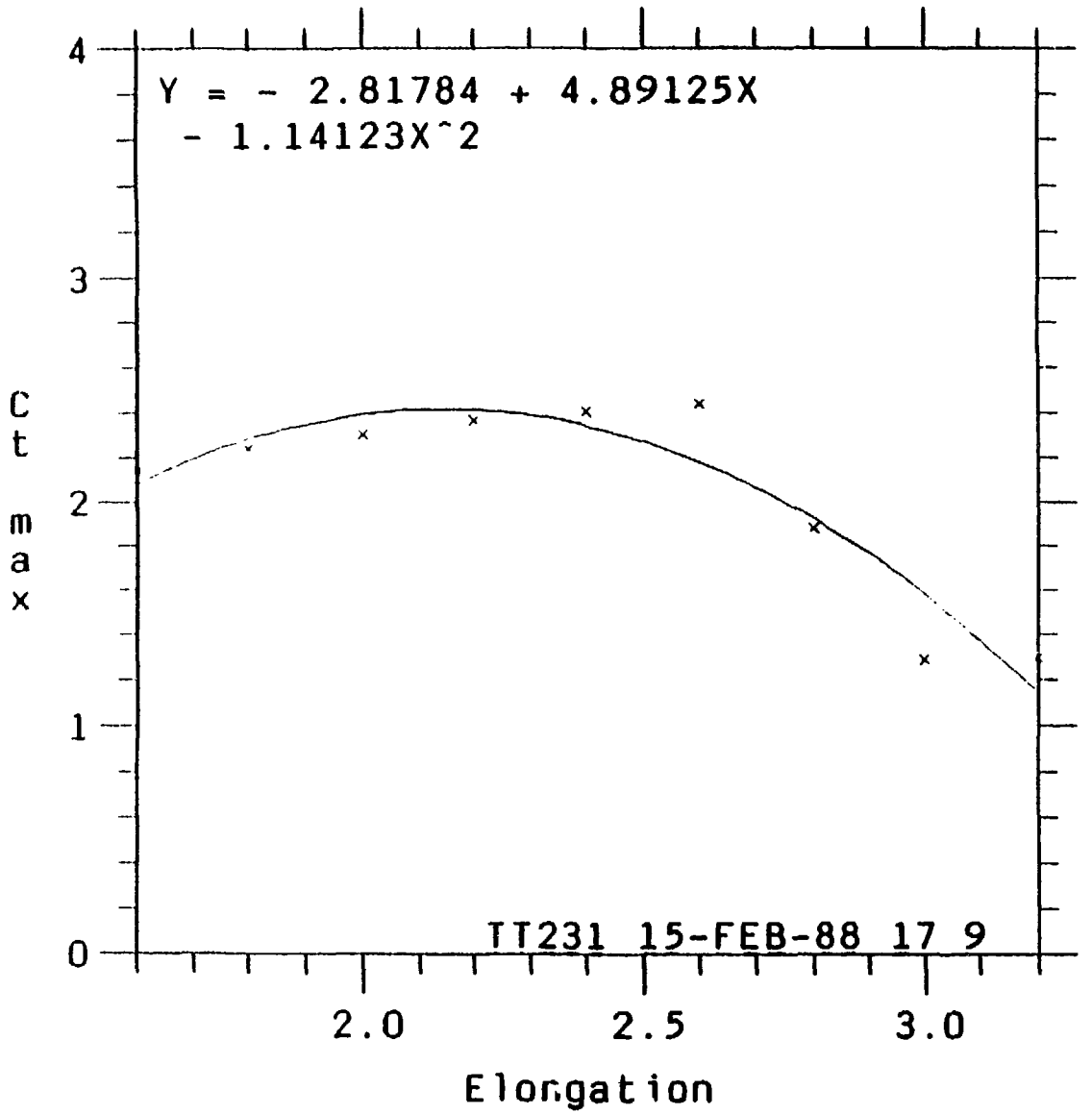
Y = - 2.81784 + 4.89125X
- 1.14123X^2
TT231 15-FEB-88 17 9
Ct max
Elongation
0
1
2
3
4
2.0
2.5
3.0

A.6

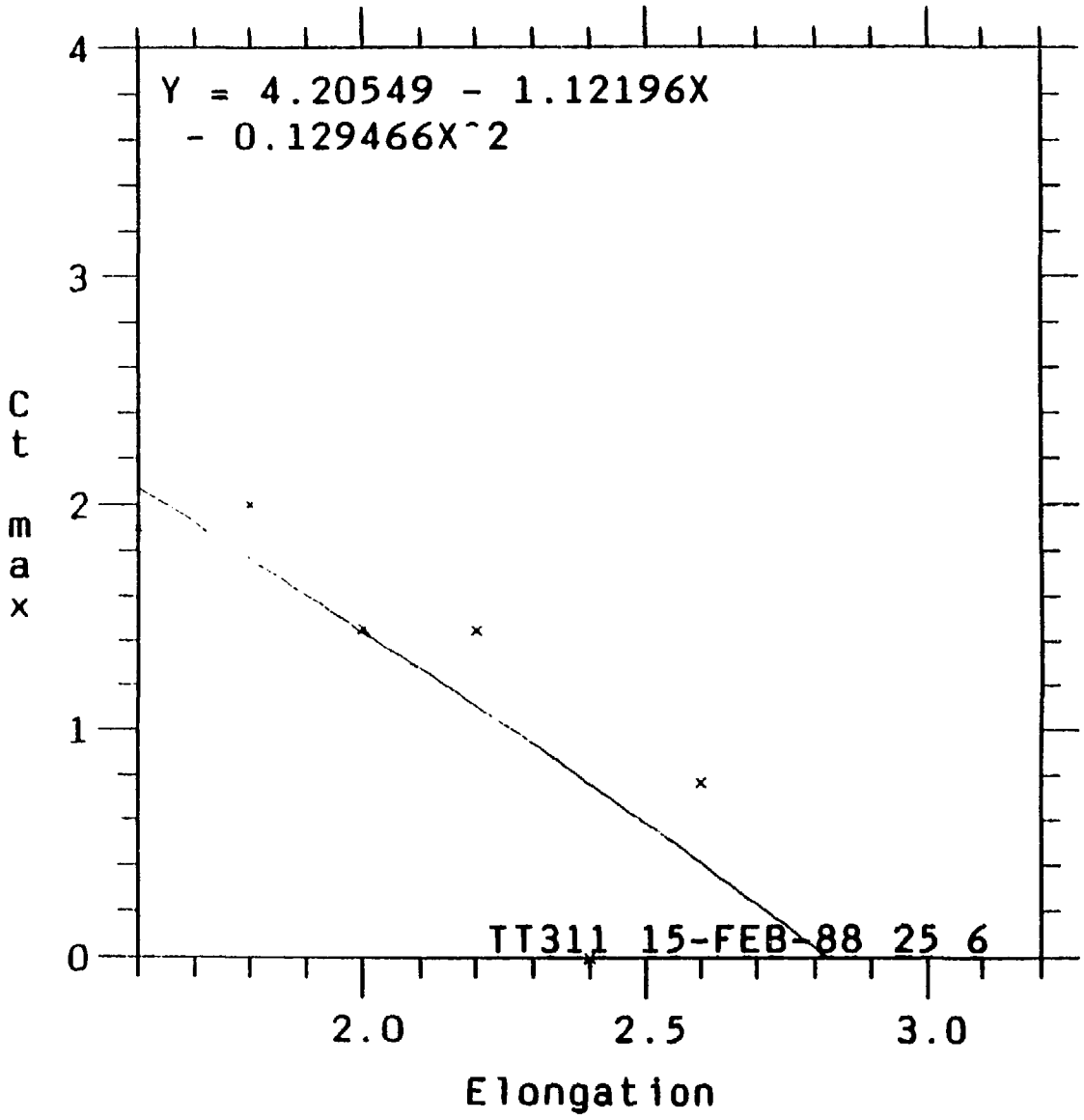
Y = 4.20549 - 1.12196X
- 0.129466X^2
TT311 15-FEB-88 25 6
Ct max
Elongation
0
1
2
3
4
2.0
2.5
3.0

A.7

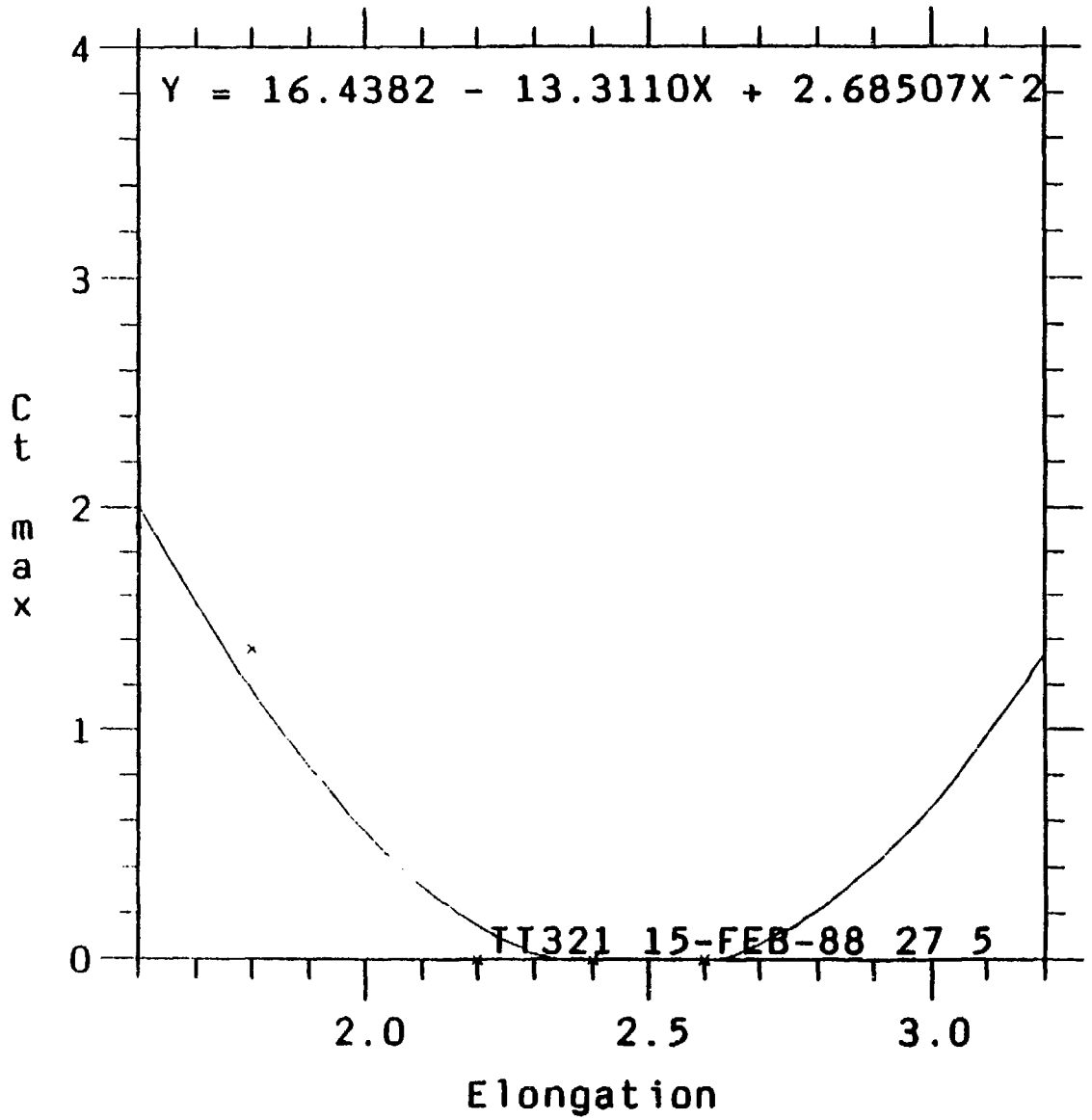
Y = 16.4382 - 13.3110X + 2.68507X^2
TI321 15-FEB-88 27 5
Ct max
Elongation
0
1
2
3
4
2.0
2.5
3.0

A.8

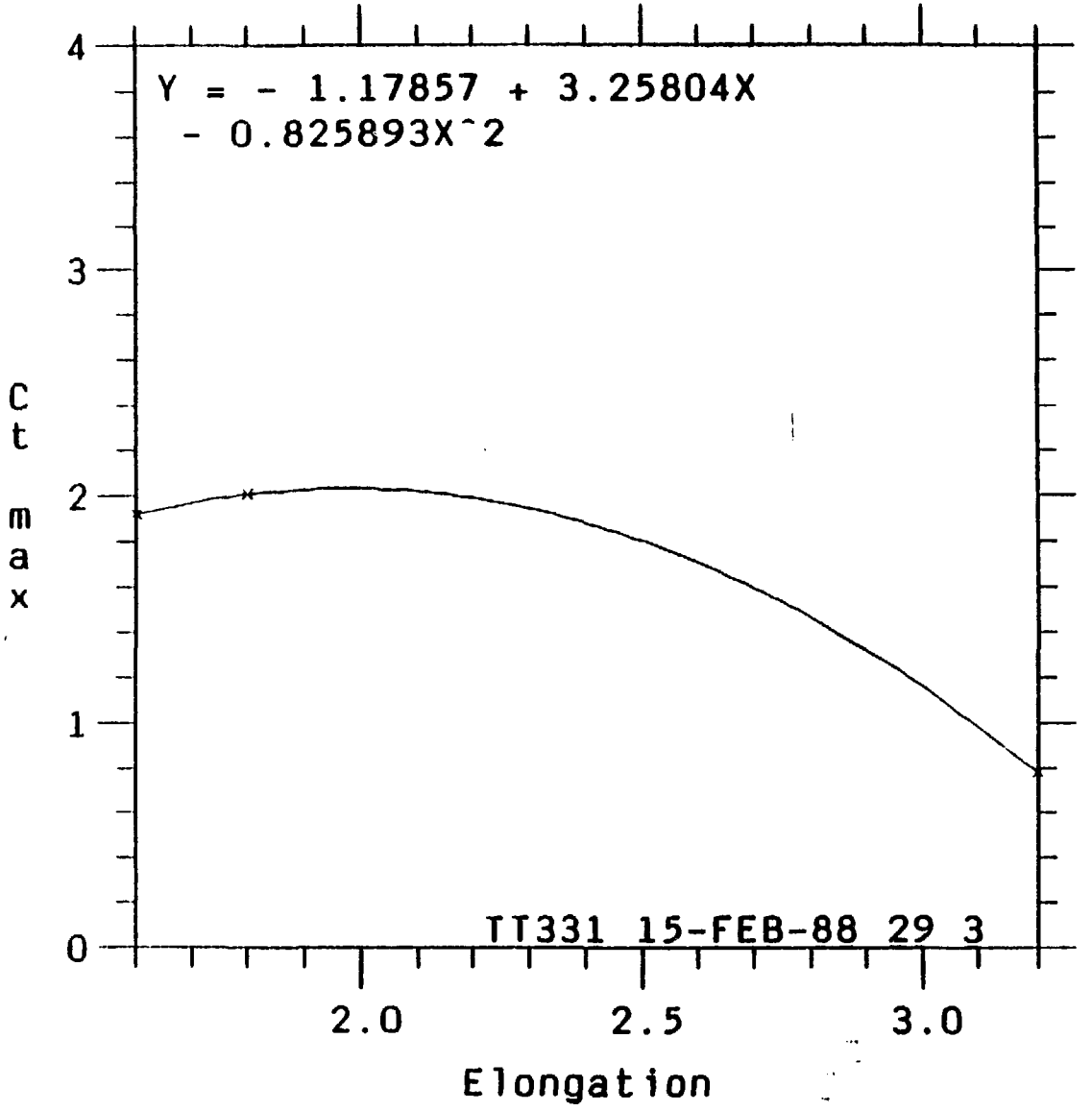
Y = - 1.17857 + 3.25804X
- 0.825893X^2
TT331 15-FEB-88 29 3
Ct max
Elongation
0
1
2
3
4
2.0
2.5
3.0

A.9

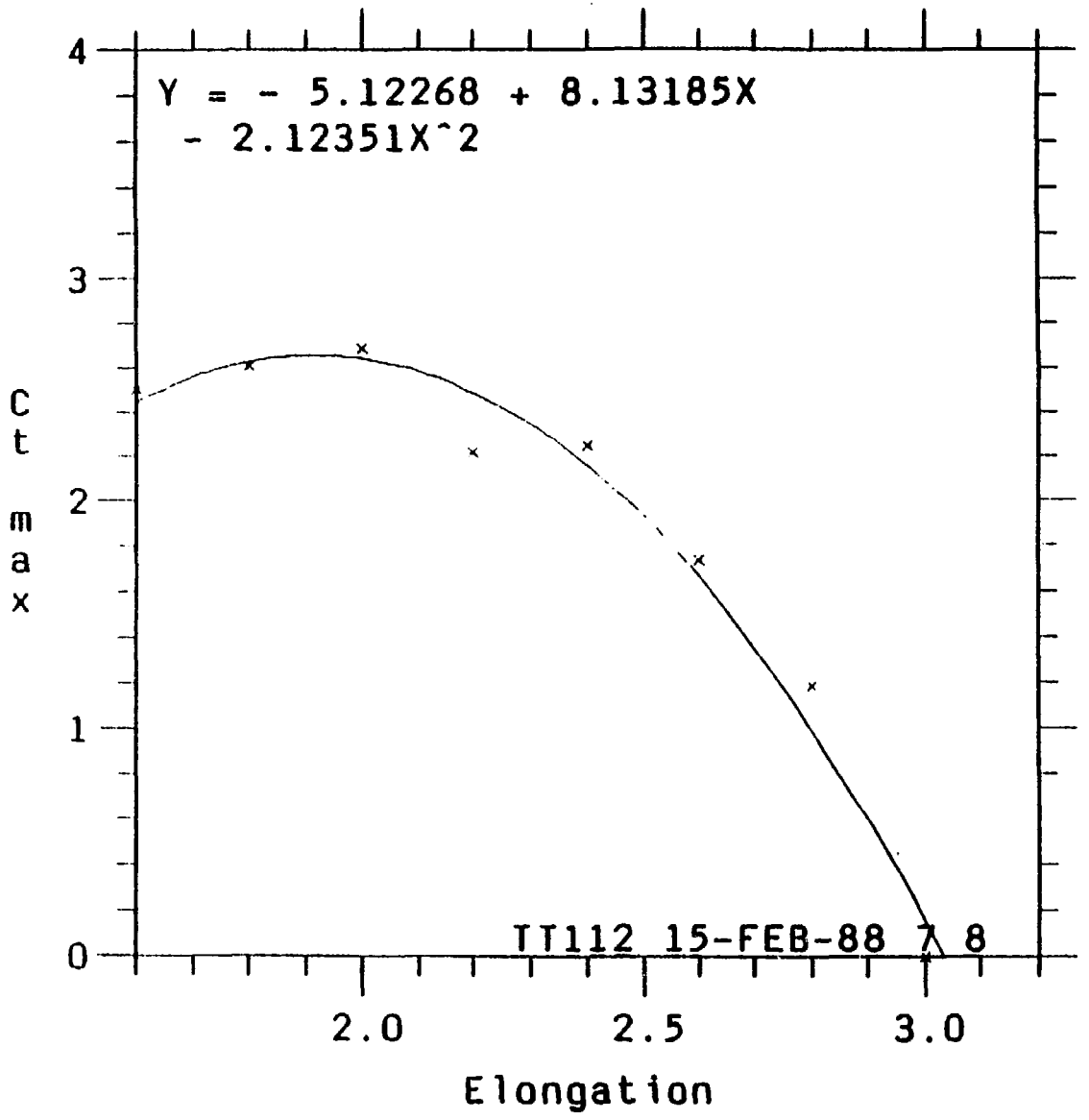
Y = - 5.12268 + 8.13185X
- 2.12351X^2
TT112 15-FEB-88 7 8
Ct max
Elongation
0
1
2
3
4
2.0
2.5
3.0

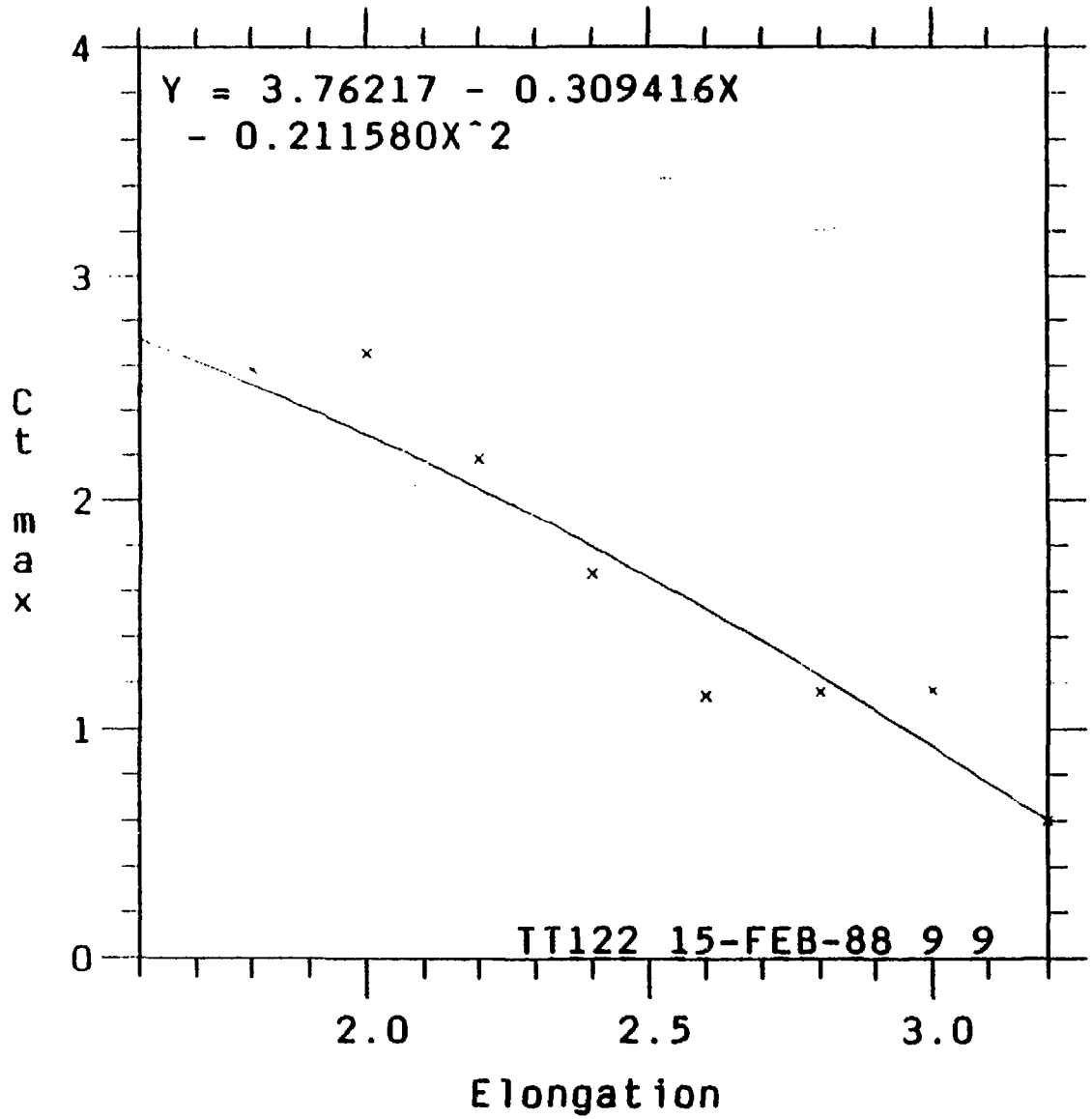
Y = 3.76217 - 0.309416X
- 0.211580X^2
TT122 15-FEB-88 9 9
Ct max
Elongation
0
1
2
3
4
2.0
2.5
3.0

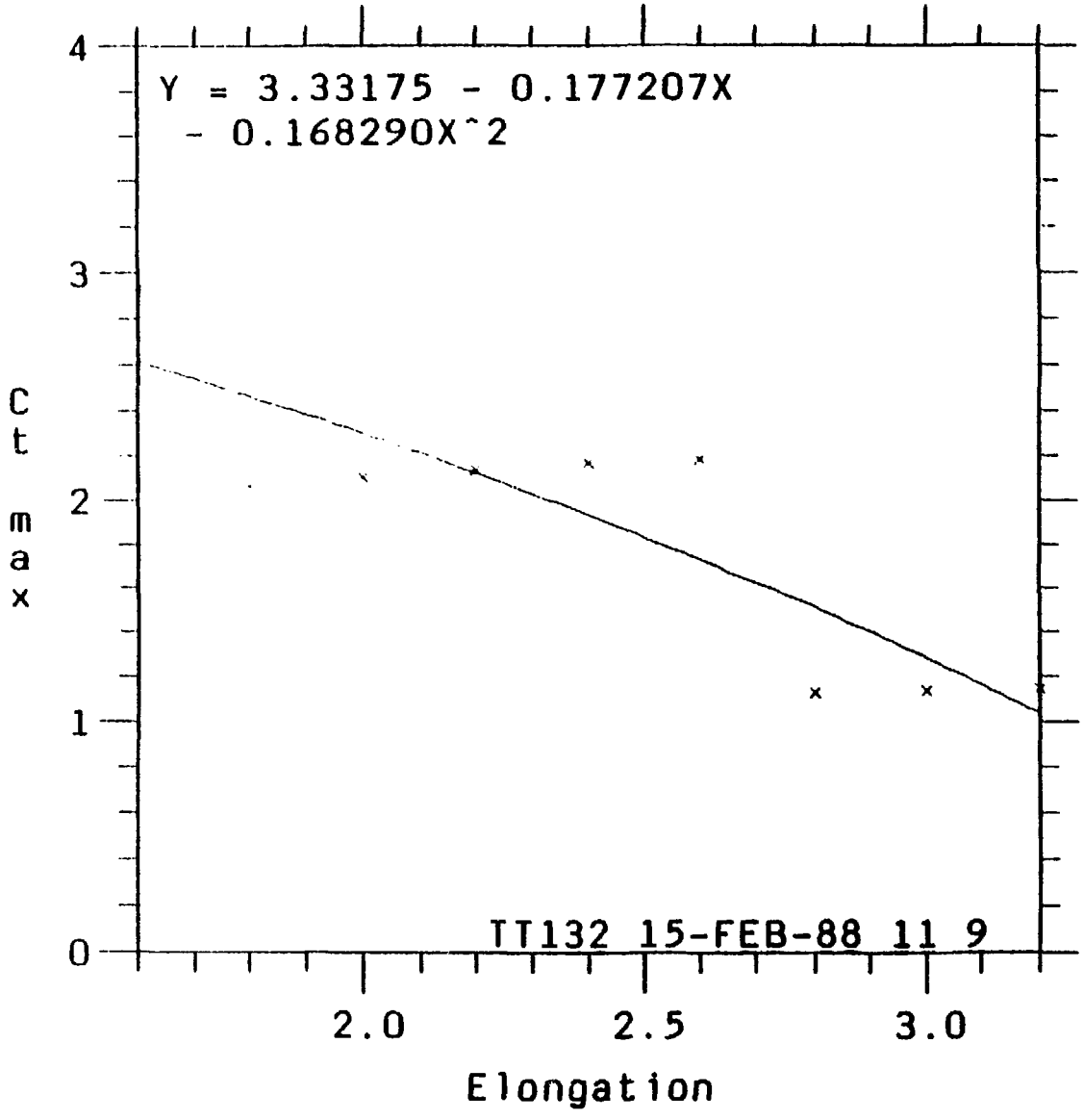
Y = 3.33175 - 0.177207X
- 0.168290X^2
TT132 15-FEB-88 11 9
Ct max
Elongation
0
1
2
3
4
2.0
2.5
3.0

A.12

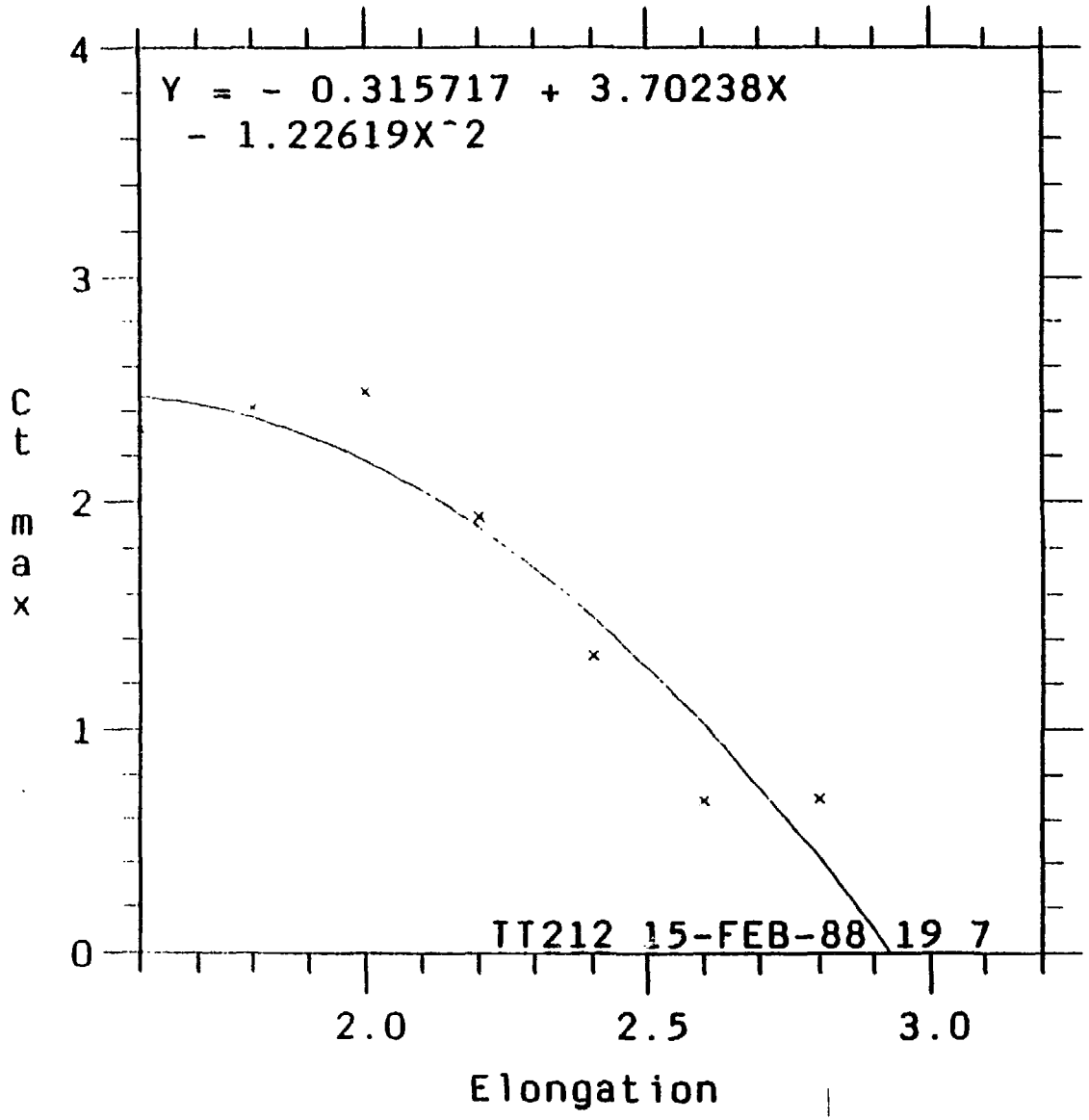
Y = - 0.315717 + 3.70238X
- 1.22619X^2
TT212 15-FEB-88 19 7
Ct max
Elongation
0
1
2
3
4
2.0
2.5
3.0

A.13

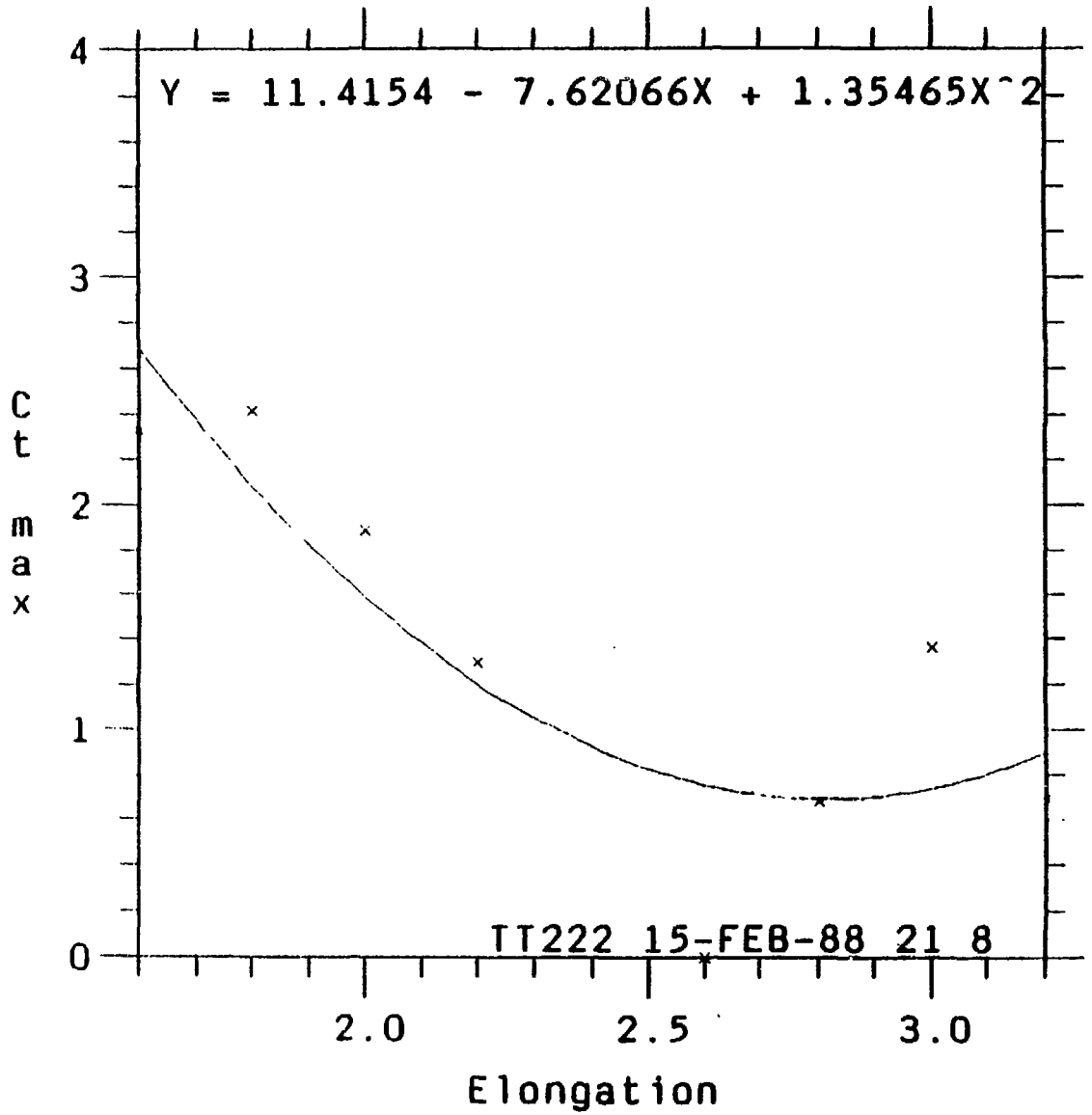
Y = 11.4154 - 7.62066X + 1.35465X^2
Ct max
4
3
2
1
0
2.0
2.5
3.0
Elongation
TT222 15-FEB-88 21 8

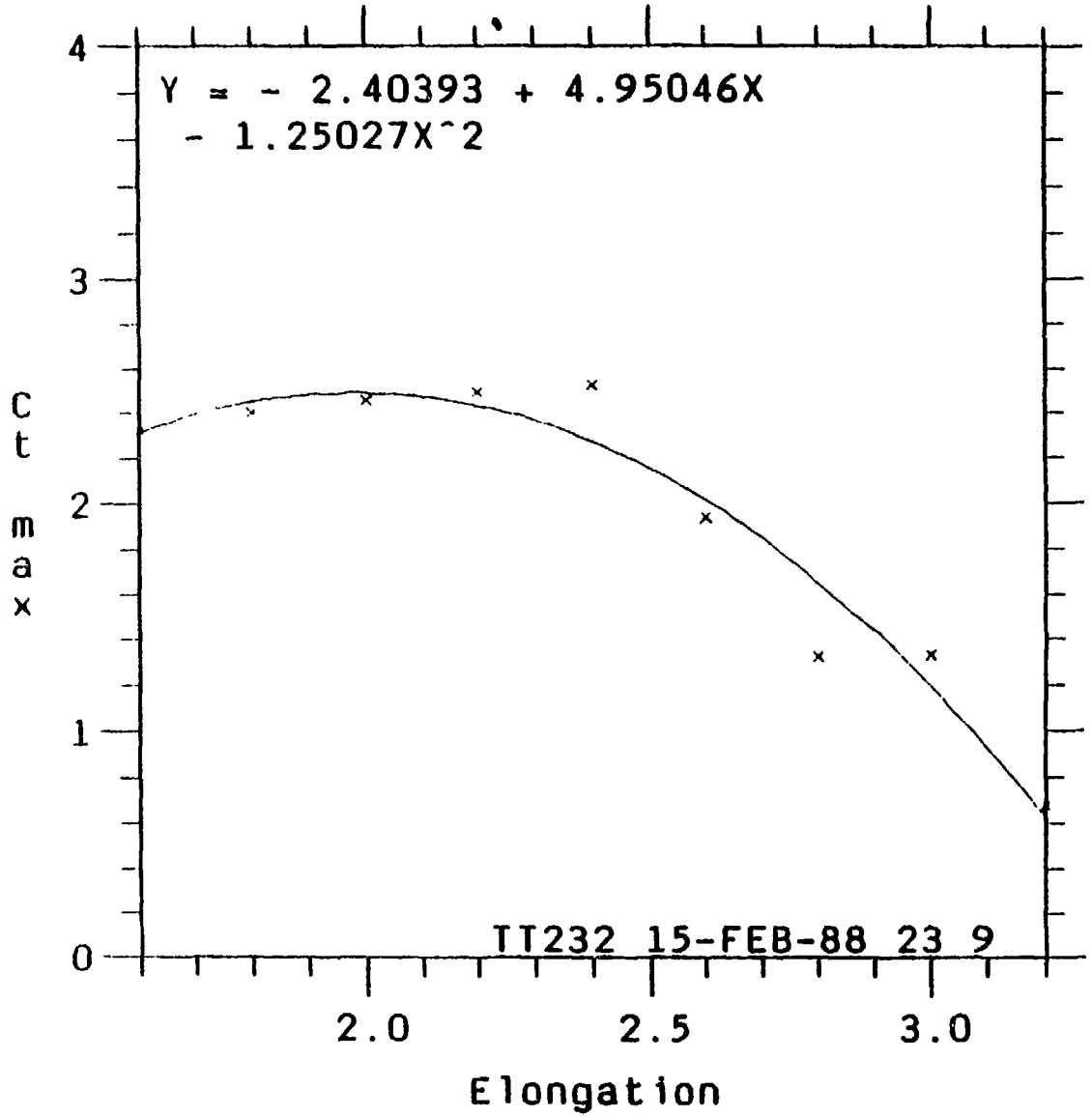
Y = - 2.40393 + 4.95046X
- 1.25027X^2
TT232 15-FEB-88 23 9
Ct max
Elongation
0
1
2
3
4
2.0
2.5
3.0

A.15